Title
Synthesis and Analysis of Mammary Gland Organoids

Author
Weber, Robert Joseph

Publication Date
2017

Peer reviewed|Thesis/dissertation

Synthesis and Analysis of Mammary Gland Organoids

by

Robert Joseph Weber

DISSERTATION

Submitted in partial satisfaction of the requirements for the degree of

DOCTOR OF PHILOSOPHY

in

Chemistry and Chemical Biology

in the

GRADUATE DIVISION

of the

UNIVERSITY OF CALIFORNIA, SAN FRANCISCO

Acknowledgements

Firstly, I would like to thank my family for raising me and encouraging an interest in science and mathematics. I also thank my numerous scientific mentors over the years, but especially Dr. Rushia Turner and Dr. John M. Lyle from my time at UCSC and Pacific Biosciences, respectively. Thanks to my classmates both in the MSTP program as well as CCB for coming on this journey with me. Finally, thanks especially to Dr. Samantha I. Liang, my wife, who provided not only emotional support, but also intellectual support. She is a far superior scientist than I as well as a master communicator and always patiently offered advice and assistance throughout my graduate career. Needless to say, her insights and support made graduate school a much smoother experience.

My graduate experience in the Gartner and Desai labs has taken several interesting turns. From joining the lab as a chemistry student and working on projects closely related to synthesis to a project heavy on 3D culture and imaging and finally culminating in a project mostly computational in nature – it has been a fascinating journey with many steep learning curves. I have been buoyed by the unwavering support, enthusiasm, and advice from my two mentors Zev Gartner and Tejal Desai. It is difficult to imagine a more supportive environment where such a breadth of work could take place.

I would like to thank Professors Matt Thomson, Thea Tlsty, Mark LaBarge, and Alexander Borowsky as well as Dr. James Garbe for providing the advice and expertise we needed to advance these projects. I would like to thank my co-authors for the fatty-acid DNA manuscripts, Dr. Samantha Liang, Nick Selden,

Dr. Alec Cerchiari, and Lucas Delannoy. I would like to also thank fellow researchers Dr. Sisi Chen, Mr. Emeric Charles and Dr. Thomas Norman for discussions, advice, and teaching about single cell RNA seq. I would like to thank Dr. Lyndsay Murrow who I worked closely with on all aspects of the RNA seq project as well as Dr. Joseph (Tony) Caruso who provided invaluable insight and analysis on all tissue-related aspects of that project. Professors Jack Taunton, Kevan Shokat, and Pam England were kind enough to share facilities and reagents. Help and advice from the Laboratory for Cellular Analysis, particularly Sarah Elmes, and the UCSF Center for Advanced Technology, especially Professor Eric Chow and Mr. Derek Bogdanoff were instrumental for a number of the enclosed studies.

Part of this dissertation is a reproduction of previously published articles and contains contributions from collaborators listed therein. Chapter 1 is reproduced in part from Weber, R. J., Desai, T. A., & Gartner, Z. J. (2017). Non-autonomous cell proliferation in the mammary gland and cancer. Current Opinion in Cell Biology, 45, 55–61 and .Chapters 2 is reproduced in part from Weber, R. J., Liang, S. I., Selden, N. S., Desai, T. A., & Gartner, Z. J. (2014). Efficient Targeting of Fatty-Acid Modified Oligonucleotides to Live Cell Membranes through Stepwise Assembly. Biomacromolecules, 15(12), 4621–4626. Chapter 3 is reproduced in part from Weber, R. J., Cerchiari, A. E., Delannoy, L. S., Garbe, J. C., Labarge, M. A., Desai, T. A., & Gartner, Z. J. (2016). Rapid Organoid Reconstitution by Chemical Micromolding. ACS Biomaterials Science & Engineering, 2(11), 1851–1855.

Abstract

The mammary gland is an important model system for several reasons but principal among them is that structural and signaling motifs found in the mammary gland recur throughout other organ systems and that due to surgical discard material, human tissue is readily available for study. The mammary gland is composed of a bilayered, tubular epithelial tree embedded in stroma. This system has been leveraged in-vitro in three-dimensional (3D) cell culture to model the impact of stromal-epithelial interactions at the scale of organoids.

To better understand cells interacting with their microenvironment, we developed DNA-based chemical tools to control the three-dimensional position and adhesion of cells. We optimized a bipartite system to label cell membranes with fatty acid modified, single strand DNA (ssDNA) in order to encode specific binding properties unto the cells. We demonstrate that this approach is synthetically simple, produces more robust labeling than comparable chemistries, and results in labeling of primary cells. We optimized the kinetics of this ssDNA labeling system and developed a capping strategy to effectively quench the reactivity of residual ssDNA on cell surfaces. We combined this ssDNA system with photolithographically defined microwells to rapidly cast multicellular structures of arbitrary shape, size and throughput. Finally, we studied primary organoids from multiple reduction mammoplasty samples with single cell RNA sequencing (scRNA seq) in order to enumerate the cell types and heterogeneity within the epithelial compartment of the mammary gland. Greater understanding of the populations of cells within the mammary epithelial system and how those

cells signal to their environment are likely to yield important insights for mammary pathologies such as breast cancer and guide future treatment regimes.

TABLE OF CONTENTS

LIST OF TABLES

TABLE OF FIGURES

CHAPTER 1

INTRODUCTION: A REVIEW OF ORGANOIDS AND MAMMARY GLAND SIGNALING

*Source: The following chapter was published as parts of two reviews. "Dissecting the stem cell niche with organoid models: an engineering-based approach." Murrow LM, Weber RJ, Gartner ZJ. Development (*2017*) and "Non-autonomous cell proliferation in the mammary gland and cancer." Weber RJ, Desai TA, Gartner ZJ. Curr Opin Cell Biol (*2017*).*

Contributions: The sections of the manuscripts presented here are original reviews of the literature on bottom-up approaches to building tissue models with multiple cell types and the impact of microenvironmental signals on cell division in the mammary gland. The listed authors wrote the manuscripts. Figures were contributed by myself and Dr. Lyndsay Murrow.

ORGANOIDS AS TOOLS TO INVESTIGATE NON-AUTONOMOUS CELL SIGNALING AT INTERMEDIATE LENGTH SCALES

Classic studies of cell growth and proliferation have used relatively homogeneous populations of immortalized cells due to their experimental tractability. In these cases, cells seem to autonomously decide whether to grow and divide, as microenvironmental cues are dominated by media formulation and physical cues such as local cells density. These homogeneous cell cultures allow for the detailed analysis of pathways controlling the cell cycle, for example, through gain and loss of function perturbations targeted to specific gene products. However, in multicellular organisms, interactions between heterogeneous cell populations are often the primary regulators of growth during development, normal tissue function, and even in diseases such as cancer. This realization has motivated the development of organoid, co-culture, and tumor xenograft models that provide a means to study so-called non-autonomous cell growth. While all cellular decisions in metazoan are to one degree or another regulated by signals generated by neighboring cells and tissues, we define non-cell autonomous behaviors as those cases where a signal or perturbation impinging on a cell triggers a response in a neighboring cell that may not have received the signal or that may be incapable of receiving the signal. In the case of proliferative control, this means that a signal impinging on one cell type triggers growth and proliferation in a neighboring or secondary cell type. Understanding the principles and mechanisms that regulate non-autonomous cell

growth will be critical for gaining deeper insight into the consequences of tumor heterogeneity, epithelial-stromal interactions, and will provide fertile ground for the discovery of new therapeutic targets and strategies.

The term organoids can refer to outgrowths from primary tissue explants (as in the mammary field), digested tissue fragments from organs, or to clonal outgrowths from single cells.[1] In this chapter, we focus in particular on two types of organoids – those produced by reaggregating mature cells together again and those produced by from outgrowths of single stem cells. (Fig. 1-1A) Organoids grown from pluripotent ESCs or iPSCs mimic embryonic developmental processes, whereas those derived from adult stem cells can be used to model tissue homeostasis and its disruption during disease progression. Together, such organoids, whether derived from pluripotent or adult stem cells, represent a diversity of organotypic cultured tissues that each recapitulate aspects of brain, retina, stomach, prostate, liver or kidney structure. [2,3]

As well as providing an easily accessible *in vitro* platform for understanding development and disease, organoids, especially those derived from adult stem cells, provide a convenient means to investigate stem cell-niche interactions. The stem cell niche can be defined as the local environment that surrounds a stem cell, which directly influences stem cell behavior and fate .[4] Indeed, some evidence suggests that in many cases the stem cell niche – rather than the stem cell itself – is the functional unit that controls cell fate. For example, transplantation into the mammary gland microenvironment reprograms single

neural stem cells into mammary epithelial cells that can regenerate the mammary epithelial tree.[5] The individual components that comprise the stem cell niche depend on the specific tissue, but include factors such as other differentiated cell types, signaling molecules, extracellular matrix (ECM) components, the 3D shape and arrangement of cells, and mechanical forces such as tension, rigidity and even fluid flow. Although many important niche components have been identified for different adult stem cell populations throughout the body, there are still many unknowns. In particular, it has been difficult to dissect the precise mechanism by which individual components regulate the niche owing to their interdependence. While *in vivo* animal studies have proven invaluable in defining the concept of the stem cell niche and identifying key stem cell-niche interactions, organoids serve as a complementary approach that could provide a better-controlled and higher-throughput platform to assess the contributions of individual niche components. Additionally, organoids can be used to study uniquely human stem cell-niche interactions (Fig. 1-1B), which will further our understanding of human tissue homeostasis, disease and regeneration.

In vitro organoid systems have a number of key advantages when it comes to modeling stem cell biology. These include the fact that organoids can be grown as clonal outgrowths from single cells, and that they can be derived from human cells. In organoids grown from single cells, putative adult stem cell populations can be identified based on a cell's organoid-forming capacity (Fig. 1-1A). [6-8] Moreover, organoids grown from human adult stem cells directly model human-specific stem cell biology and can identify differences between human

and non-human tissues (Fig. 1-1B). [6,7,9] Another key advantage of organoid culture is that it allows in-depth experimental perturbation and imaging of stem cells in their surrounding niche. This reductionist model can be used to identify molecules that are sufficient for functional maintenance, complementing *in vivo* models that identify those that are necessary. Finally**,** *in vitro* systems allow tight temporal control over chemical and genetic manipulation of the stem cell niche and facilitate both single-cell resolution and high-throughput 3D imaging over time (Fig. 1-1B).[10] Together, these features of organoids, in parallel with *in vivo* models, will help to reveal the underlying principles that guide tissue formation, maintenance and breakdown during development and regeneration.

In this chapter, we focus on adult stem cell-derived organoids and use the examples of the mammary gland, to describe how organoids have enabled intensive and systematic study of signals from the adult stem cell niche that control cell self-renewal and differentiation (Fig. 1-1C). We further describe some emerging technologies that now enable reconstitution of the stem cell niche from purified cellular and ECM components. Though stem cells and the niche are used as an example, these concepts are generalizeable to other cell interactions of interest. These engineering-based approaches can provide tight control over individual niche components and parameters such as initial organoid composition and size, which, under most commonly used organoid culture conditions, can be heterogeneous. Finally, we describe examples of non-autonomous cell signaling in the mammary gland illustrating that the smallest physiological unit of structure in the mammary gland is likely the organoid as opposed to single cells.

THE MAMMARY GLAND IS REGULATED BY ENDOCRINE AND JUXTACRINE SIGNALS

The mammary gland is a bilayered, tubular epithelial tree. Lining the lumen are milk producing, luminal epithelial cells (LEPs) surrounded by a layer of contractile myoepithelial cells (MEPs). The MEP layer is surrounded by a basement membrane, separating the epithelium from a stroma containing numerous additional cell types such as fibroblasts, adipocytes, lymphocytes, neurons, and endothelial cells. [11,12] Within the luminal layer of the epithelium, there exists a minor population of post-mitotic, hormone sensing cells which range from 7 to 30% in the human mammary gland depending on a host of factors including age, pregnancy history, and exposure to hormones.[13] These cells are generally defined using immunohistochemical (IHC) detection of nuclear localized estrogen receptor alpha (ERα) and progesterone receptor (PR), and are frequently referred to as ER(+) cells.[14] Without dividing themselves[13,15], this minor population integrates hormonal signals produced by the ovaries and coordinates post-natal development and post-pubertal cyclical expansion/regression of the mammary gland via an intricate paracrine signaling network (Fig. 1-2).

At three different developmental stages – prepubertal, postpurbertal, and pregnant – a distinct spectrum of hormones signal through ER(+) cells which in turn send out new signals to the microenvironment that serve to coordinate

growth and morphogenesis. At the pre-pubertal stage, for example, estrogen-dependent signaling activates the sheddase activity of the ADAM17 protease to release transforming growth factor alpha (TGF-α) and amphiregulin, Epidermal Growth Factor Receptor (EGFR) ligands, to fibroblasts in the stromal compartment which then signal back to the epithelial compartment promoting ductal tree elongation. [12,16,17] The complete mechanism of stromal signaling back to the epithelial compartment remains unclear, but depends on fibroblast growth factors 10 in the stroma and fibroblast growth factor receptors 1 and 2 in the epithelium. [18,19] At the post-pubertal stage, ERα activation is also permissive of PR expression, which when activated, results in local proliferation, primarily via secretion of paracrine signaling molecules: RANKL and Wnt4. [20-22] Rajaram ***et al*.** used serial engraftment of mutant mammary epithelial tissue with deletions in either RANKL or Wnt4 in contralateral mouse fat pads and observed that loss of RANKL modestly reduced proliferation, primarily by a reduction in the amount of side branching. By the third serial transplant, loss of Wnt4 secretion led to a drastic decrease in proliferation, more so even than PR deletion. They went on to parse Wnt4 secretion in the perinatal as well as pubertal and adult mammary gland. Their work and others supports a model in which canonical Wnt4 signaling downstream of PR is important for cell self-renewal and drives proliferation of $CD44^{high}$ $CK5^{+}$ luminal progenitor cells required for cyclical expansion and regression in the pubertal and adult mammary gland. [21,23] Though these experiments were conducted in mice, additional work has suggested PR is a key signaling pathway in the human mammary gland as well.[20] Finally, at the

pregnant stage, prolactin receptor activation can trigger secondary effects in the epithelium beyond its typical role in stimulating the production of milk proteins such as Beta casein during pregnancy. Recent work by Tarulli *et al***.** has demonstrated a unique response of hormone sensing/ER(+) cells to low levels of prolactin due to differences in Wip1 expression, a phosphatase that regulates Jak-Stat signaling. This difference results in hormone sensing/ER(+) cells converting prolactin signals into paracrine growth factors such as RANKL and IGF2 as opposed to milk production.[24]

In these three different developmental stages, a rare population of hormone sensing cells within the luminal compartment integrate systemic signals impinging on the gland through the blood stream to drive the exclusive proliferation of their neighbors. In cancer, these and other signaling pathways are frequently co-opted by the tumor and used in a dysregulated manner to promote tumor progression.[25] In invasive breast cancer, for example, ERα signaling is active and necessary for the growth and survival of nearly two thirds of tumors. This observation has driven the development and frequent clinical use of endocrine therapies that block estrogenic signaling, either through competitive inhibitors of ER such as tamoxifen, or through blocking the local conversion of androgens to estrogens via aromatase inhibitors.[26] Strikingly, patients with tumors containing as few as 1% ER+ cells, as defined by IHC staining, still benefit from anti-endocrine therapy.[27] It is interesting that these therapies are effective while presumably targeting such a small proportion of tumor cells, and highlights how non-autonomous proliferation may act as a hub for proliferative

control in both the normal and diseased mammary gland. While we still know relatively few mechanistic details governing the estrogenic paracrine signaling circuit in ER(+) breast cancers, particularly a detailed understanding of stromal–epithelial cross-talk, it is likely to be important given its role in normal gland function. It is possible, for example, that estrogenic signaling, in addition to allowing PR expression, is permissive of stromal alterations, creating a permissive microenvironment for tumor growth through mechanisms that remains to be determined. Along these lines, there is evidence that dysregulated RANKL is predictive of disease[28] and there is growing interest in targeting paracrine signaling such as by RANKL inhibition for breast cancer treatment[29,30] though specific mechanisms remain to be elucidated. Wnt4 has also been implicated as an important factor in cell line models of breast cancer, including in an endocrine resistant model, again paralleling its important role in normal physiology. [31,32] Further insight into these pathways, and the changes they promote within the stromal and epithelial compartments, will likely be fertile ground for novel therapeutic interventions. [12,33]

While hormone-sensing cells and their canonical ligands are central to paracrine signaling in the mammary gland, and also play a role in estrogen-dependent breast cancers, recent studies have unveiled additional examples of divisions of labor within the mammary gland that regulate its growth and remodeling. Sonic Hedgehog pathway is a key pathway for epithelial-to-mesenchymal transition across several tissues.[34] Visbal *et al***.** demonstrated that overexpression of smoothened, a key transducer of hedgehog signaling, in

luminal cells, stimulates proliferation in neighboring luminal cells and also serves to alter the stromal microenvironment, attracting macrophages.[35] This is a phenotype frequently observed in ductal carcinoma *in-situ* lesions (DCIS) and is conceptually analogous to the recruitment of tumor-associated macrophages and promotion of a tumorigenic microenvironment discussed below. A follow-up study by O'Toole ***et al*.** demonstrated negative survival in a cohort of 279 patients with invasive ductal carcinoma that correlated with the level of hedgehog signaling in the epithelium. They also showed that receptors in the stromal compartment, rather than epithelium, mediated this effect.[36]

Examples of non-autonomous cell growth, such as those described here in the mammary gland are common in normal physiology of other tissues. Moreover, there is an increasing appreciation that similar mechanisms likely play an important role in the progression and therapeutic response of cancers. Generally, these pro-proliferative signals take the form of paracrine growth signals or direct modulators of the physical and chemical microenvironment, and recent studies suggest that these pathways can be manipulated pharmacologically for therapeutic benefit. Therefore, a mechanistic examination of non-autonomous cell proliferation is vital in order to enhance our understanding of the complex cellular interactions that regulate normal physiology, as well as to develop the next generation of novel, rationally designed therapeutics.

One important challenge that is beginning to be addressed is developing a better understanding of the difference between stable cell 'types' and dynamical cell 'states'.[37] Measurements at a fixed time point or tissue state may not be sufficient reveal the dynamical cell-cell interaction landscape, leading to context-dependent, rather than generalizable, findings. Another challenge is identifying the correct *in vitro* or *in vivo* model to examine non-autonomous growth control. Given the complexity of cellular interactions regulating normal and diseased tissues, along with the important differences between human and mouse physiology[38], this can be a particularly vexing problem. However, recent advances in cell culture systems – be they 2D co-cultures, 3D systems with extra cellular matrix mimetics[1], or even 'organ on a chip' technologies[39] – are poised to advance our understanding of complex multicellular interactions among human cells.

A key advantage of multicellular models such as organoid is that *in vitro* growth allows decoupling of local signals within the niche from long-range signals, such as those that would impinge on the tissue from the bloodstream or surrounding stroma *in vivo*. Joshi and colleagues showed that systemic signals in the form of the steroid hormones estrogen and progesterone regulate stem cell dynamics *in vivo* but, surprisingly, that mammary stem cells themselves do not express receptors for progesterone and estrogen.[40] In this study, treatment of ovariectomized mice with estrogen and progesterone restricted mammary luminal differentiation and increased the proportion of organoid-forming cells in the mammary gland. These studies suggest that additional and locally acting

paracrine signals could provide a link between systemic hormone levels and mammary stem cell function. Among locally acting paracrine signaling molecules, Wnt has been found to control stem cell activity in multiple tissues[41] and, indeed, evidence suggests that Wnt is also a key component of the mammary stem cell niche. Wnt ligand treatment was found to promote mammary stem cell self-renewal, allowing serial, long-term expansion of mammary organoids. [23,42] Although these studies identified systemic (estrogen) and local (Wnt) signals that regulate mammary stem cell function, how these signals are coordinated remained unclear.

Recent work with mammary organoids has helped to uncover the mechanism by which hormone receptor-negative mammary stem cells respond to hormones through local relay of Wnt molecules.[23] Combined treatment with progesterone and estrogen induced the expression of Wnt4 and the Wnt agonist R-spondin 1 in luminal cells, which the authors showed is important for mammary stem cell self-renewal. Furthermore, they demonstrated that, in the absence of exogenous Wnt, hormone treatment supports expansion of mammary organoids from mammary stem cells only in the presence of luminal cells. Together, these data are consistent with a model in which systemic steroid hormone signaling induces local Wnt signaling from daughter luminal cells to restrict luminal differentiation and promote self-renewal of parent stem cells. This study illustrates how *in vitro* organoid systems serve as an important complement to *in vivo* experiments, since it would be difficult to distinguish between direct or secondary effects of hormone treatment without using tissue-specific conditional

knockout mouse lines, which is both costly and time consuming. Organoid culture therefore provides a simplified experimental system in which to quickly and directly test the effects of specific niche signals on discrete cell types, which can then be confirmed by in-depth animal studies.

ENGINEERING ORGANOIDS: A BOTTOM-UP APPROACH TO CONTROLLING INITIAL ORGANOID SIZE, SHAPE AND COMPOSITION

Most current protocols for guiding stem cells to form organoids with functional niches rely on the ability of stem cells to differentiate into a number of more mature cell types, as well as the ability of these cells to self-organize into the correct tissue architecture. These protocols build upon now classic methods in developmental biology that used dissociation and reaggregation of cells from various tissues to understand how cells self-sort during morphogenesis. [43-45] Together with more recent data, these reaggregation studies suggest that cells isolated from adult tissues can retain a 'memory' of their developmental or homeostatic program that allows them to self-organize through local interactions, recapitulating aspects of the tissue architecture from which they are derived. [46-48]2

While the capacity to self-organize leads to the formation of reproducible and tightly regulated tissue architectures *in vivo*, the process can be considerably more variable *in vitro*, particularly at length scales larger than a few hundred microns.[49] Such variability suggests that key chemical, physical and/or

spatial cues that guide the progress of self-organization *in vivo* may be lacking after cell reaggregation *in vitro*. In these cases, the tools and techniques of engineering could facilitate the more robust formation and analysis of organoids. New engineering technologies such as microwell arrays, droplet-based microfluidics, 3D bioprinting, chemically programmed tissue assembly and chemically defined ECMs mean that it is now feasible to engineer organoids in such a way as to precisely define their initial size, composition and spatial organizatiom. [50-53] Control over these culture parameters has the potential to open up new experimental approaches for understanding development, regeneration and disease by providing greater spatiotemporal control over organoid culture in general and the stem cell niche in particular (Fig. 1-2)

Ideally, engineered organoids should be made from purified components, allowing direct measurement and manipulation of the physical (e.g. shape, mechanics, cellular composition) and chemical (e.g. molecular composition) properties of input cells, ECM and medium. For example, engineering strategies provide a simple and precise means for the marking and tracking of input cell populations as they move and differentiate within organoids (Fig. 1-3A). Furthermore, they provide a facile means of activating or inhibiting chemical and physical cues in specific cell types by targeting gain- or loss-of-function perturbations to only the intended cell type prior to cell reaggregation.[54] Similar experiments using standard organoid cultures grown from individual stem cells or tissue explants would require sophisticated cell type-specific chemical or genetic targeting strategies. Combined with new and powerful technologies for genome

editing and spatiotemporal control of gene expression (e.g. CRISPR/Cas9 and optogenetics), engineering approaches will allow the manipulation and *de novo* construction of synthetic signaling circuits to facilitate our understanding of cell-cell communication within and around the niche.

An engineering approach to organoids will also allow the generation of tissues with defined initial compositions, shapes and spatial organization.[55] By enabling control over the starting number and types of cells in the organoid (Fig. 1-3B), these approaches provide a highly reproducible system that can be used to understand how tissue composition affects stem cell differentiation and cellular plasticity, and how stem cells self-organize within a tissue. Precise control over the cellular inputs for organoid culture can also identify the cell types and matrix components that comprise the 'minimal niche' sufficient for tissue self-renewal. [53,54] Furthermore, combinations of technologies, such as microfluidics and chemically programmed assembly, make it possible to incorporate sensors that dynamically measure properties such as mechanical forces within live tissues (Fig. 1-3C).[56] These advantages will enable systematic modeling, quantification and testing of stem cell-niche interactions to more fully define the systems-level cellular and molecular networks that control tissue homeostasis.

In this section, we summarize some emerging approaches for precisely controlling organoid cultures, including the use of microwells, microfluidics, bioprinting, chemically programmed assembly and engineered ECMs (Fig. 1-4). These new approaches for the generation and study of organoids will help define

the necessary and sufficient components of the stem cell niche, provide more quantitative insight into the role of plasticity and dedifferentiation in maintaining tissue homeostasis, and contribute to our emerging understanding of how the chemical and physical properties of the niche direct stem cell self-organization and behavior.

MICROWELLS PROVIDE CONTROL OVER ORGANOID SHAPE AND SIZE

Photolithographically defined microwells are one relatively simple technique to control initial organoid shape and size by providing a well-defined environment in which to aggregate cells. Wells are commonly microfabricated from weakly adhesive materials such as polydimethylsiloxane (PDMS) or non-adhesive materials such as agarose, and can be used to produce uniform cell aggregates of discrete sizes by varying well depth, diameter and seeding density (Fig. 1-4A). [57-59] Following condensation, spheroids can be transferred into ECMs for 3D culture. This general strategy is even compatible with forming reproducible embryoid bodies from human ESCs.[60] For cell aggregates that require immediate ECM contact for appropriate condensation and self-organization, microwells can be directly stamped into matrices such as collagen and subsequently overlaid with additional collagen to create fully embedded tissues.[61] This technique also facilitates the production of organoids with more complicated shapes, such as branching patterns. For softer ECMs that cannot be directly stamped,[62] developed a technique using gelatin as a degradable scaffold to produce microwells that could then be removed by buffer exchange and replaced by

matrices such as Matrigel or fibrin, maintaining the positional fidelity of the original wells. Both of these latter methods allow the production of organoids of non-spherical shapes that can be used to dissect how morphogen gradients are set up and maintained in the stem cell niche.

One notable variation on microwells, termed microraft arrays (MRAs), utilizes a translucent polystyrene array to facilitate live in-well imaging and controlled release of individual wells for further examination such as gene expression analysis. [49,63] This method has enabled high-throughput live imaging of intestinal stem cells interacting with other cells in the niche to show that Wnt signaling from Paneth cells is contact dependent.[49] Another approach, known as intaglio-void/embed-relief topographic (InVERT) molding, uses intaglio/relief-based cell deposition – originally a type of printing technique – to seed one cell population within a recessed surface (e.g. microwells), embed the patterned cells within a hydrogel, and deposit a second cell population in the ‘voids' around the first pattern. This technique has been used to study the interactions between iPSC-derived hepatocytes and surrounding non-parenchymal cells.[64] Overall, microwell approaches facilitate the rapid production of well-defined organoids and are therefore particularly well suited for screens identifying soluble factors exchanged within the niche, and for live imaging studies of niche dynamics that require large numbers of highly reproducible tissues to obtain sufficient statistical power. A variation of this approach to organoid synthesis is elaborated in chapter 3 of this thesis.

MICROFLUIDICS APPROACHES GUIDE ORGANOID SIZE AND SHAPE

Similar to microwell approaches, microfluidics techniques can be used to assemble spheroids of desired size in a cell adhesion-dependent manner (Fig. 1-4B). Recently, microfluidic platforms have been developed to capture cells in aqueous droplets within a carrier oil. These techniques produce spheroids of a tailored size from suspended cells by controlling the size of the droplets and the density of cells in the droplet-forming solution. An advantage of this technique over microwells is the speed of droplet generation and the ease of automation, which allows high-throughput assembly of cell aggregates. [50,65,66]

In contrast to microwells, which rely on probabilistic cell loading, recent advances in droplet-based microfluidics can achieve single-cell droplet loading and can load droplets with combinations of cell types with a precision that exceeds Poisson limitations. [67-69] These devices can also be used to capture precise cell pairs, facilitating the dynamic dissection of cell-cell interactions from the initiation of contact.[70] Droplet microfluidic platforms can also be used to investigate signals from the ECM. Cell-containing droplets can be fused with droplets containing diverse ECM components, or cells themselves can be directly encapsulated within microgels containing matrix components such as collagen, synthetic integrin-recognition sequences such as arginine-glycine-aspartic acid (RGD) peptides[65,71,72] or tunable alginate gels. [73,74]

In organoid cultures, microfluidic devices can also be used to deliver soluble signals that mimic *in vivo* signaling gradients. [75,76] Based on these

features, microfluidic platforms might be particularly well suited for large-scale combinatorial screens to identify cell and matrix components that comprise the stem cell niche. Future advances in microfluidics techniques will provide automated, high-throughput interrogation of stem-cell niche components, specifically how different ratios of cell types, specific cell-cell interactions, cell-ECM interactions and ECM mechanical properties direct stem cell maintenance and differentiation.

3D BIOPRINTING ENABLES INCREASED SPATIAL CONTROL AND COMPLEXITY

Although both microwell and microfluidics approaches can be used to produce organoids with controlled numbers and proportions of purified cell populations, these methods provide relatively little spatial control over the organization of biomaterials in the extracellular environment. The rapidly developing field of 3D bioprinting provides a potential solution to this limitation. In this suite of techniques (reviewed extensively by[77-79] biomaterials including cell and ECM components are deposited in layers to rapidly pattern multicomponent objects with defined *x*, *y* and *z* coordinates (Fig. 1-4C). Newer approaches allow even more complex structures to be generated in fluidizing granular baths that can support intricate 3D structures during printing, which are then gently melted away prior to culture. [80,81] These technologies provide control over the initial positions of different biomaterials and, to a more limited extent, cell subtypes within the resolution allowed by the print head and stage. Theoretically, small

organoids themselves can also be used as a printable ink, allowing higher-order structures to be printed. [82-84] These and related 3D printing platforms, although still limited in their number of applications in the study of the stem cell niche, will ultimately provide increased control over tissue architecture spanning multiple length scales – a major challenge for directing the growth of tissues and organoids.

CHEMICALLY PROGRAMMED ASSEMBLY: PRECISE CONTROL OF CELL-CELL INTERACTIONS IN 3D

In contrast to the systems described above, which utilize endogenous cell adhesion machinery to form condensed cellular aggregates, there are a number of techniques for aggregate formation that control adhesion synthetically. [85-90] For example, liposomes can be used as a delivery system to modify the cell surface by incorporating bio-orthogonal lipids that drive covalent cell-cell adhesion via click chemistry. This technique has been combined with microfluidics approaches to assemble spheroids containing two cell types.[91] An alternative approach uses DNA as a synthetic adhesion molecule to produce 3D tissues with programmable connectivity (Fig. 1-4D). [85,88,92-95] Some of this work is elaborated upon in Chapter 2 of this thesis. In a recent advance, DNA-labeled cells were assembled onto a complementarily labeled glass surface that functioned as a spatial template, and the resulting aggregates were subsequently embedded into a 3D matrix to create tissues at single-cell resolution with defined size, shape, composition and initial spatial organization.[52] Using DNA-programmed assembly

of cells (DPAC), it is also possible to incorporate components of the mesenchyme, such as fibroblasts, allowing the engineering of a stem cell niche that captures stromal contributions. These techniques allow precise control over individual cell-cell interactions and will enable direct examination and manipulation of juxtacrine cell-cell and cell-ECM cues within the stem cell niche.

Although engineering techniques provide the possibility for increased control over organoid culture, they also come with potential pitfalls. Prior to using any of these engineering techniques, it is necessary to process tissue samples into single cells and purify the desired cell populations away from undesired cellular components. Therefore, there is a time lag before cells are placed in culture to become organoids. During this lag time, microenvironmental cues that may be necessary for appropriate localization and function within a tissue are absent. For example, it has been observed that trypsinization can cleave integral surface proteins, potentially perturbing cell function, at least temporarily.[96] Furthermore, in certain contexts cells display broader differentiation potential *in vitro* or in transplantation models that might not be relevant for undamaged tissues operating in a more typical homeostatic regime. [97-99] Given these considerations, researchers must be vigilant of potential artifacts introduced by processing steps in any of these techniques, and findings will likely need to be validated in intact tissue or *in vivo* animal models when possible.

ENGINEERED ECMS PROVIDE CONTROL OVER MECHANICAL AND BIOCHEMICAL PROPERTIES OF THE STEM CELL NICHE

The ECM is a key component of organoid culture that, across multiple tissues, supports phenotypes not seen in 2D culture on plastic. The most commonly used ECMs are derived from animal sources. For example, Matrigel is produced from Engelbreth-Holm-Swarm tumors grown in mice. It is primarily composed of laminin, collagen IV and entactin, but also contains a poorly defined cocktail of growth factors and trace amounts of hundreds of other proteins. [100-102] Similarly, other matrices such as collagen I are typically purified from animal sources or cultured cells. Because these matrices can be heterogeneous and poorly defined, lot-to-lot variability can affect experimental reproducibility.[100] Therefore, there is significant interest in synthesizing well-defined ECM mimics that support similar 3D growth and developmental phenotypes to those observed for Matrigel or other purified ECMs (Fig. 1-4E). These rationally designed matrices will significantly enhance reproducibility and enable new experimental approaches. Most notably, engineered matrices will allow the systematic and independent perturbation of ECM properties such as stiffness, viscosity, porosity, protease cleavage sites, ligand type and ligand density.[51] Manipulation of these ECM properties will allow researchers to identify how mechanical and biochemical signals interact at the stem cell niche to control self-renewal and differentiation.

To address this need, many labs have used biochemically inert crosslinked hydrogels such as polyethylene glycol (PEG) or alginate to encapsulate cells in 3D. [51,103] These hydrogels can be tuned over a wide range of stiffnesses and topologies by varying monomer concentration, molecular weight

and degree of crosslinking. Moreover, these hydrogels provide an inert starting material, allowing specific concentrations and combinations of bioactive molecules, such as integrin-recognition sequences, to be rationally engineered back into the system.[104] For example, Enemchukwu and colleagues designed a PEG-based ECM mimetic with independent, tunable control over matrix stiffness, RGD ligand density and proteolytic degradation rate.[105]

Synthetic matrices are very tractable systems for interrogating the spatiotemporal dynamics of cell-matrix interactions. For example, hydrogels can be designed with different rates of stress relaxation over time.[106] Photodegradable[107] or photoactivatable[108,109] crosslinkers can be used to pattern matrix stiffness within a gel or change stiffness over time. By coupling bioactive ligands to the hydrogel with a photodegradable linker, similar strategies can be used to manipulate the biochemical properties of the matrix in space and time.[107] This is important, as work from several labs has suggested that the mechanical properties of the stem cell niche can control self-renewal and differentiation. Engineered matrices have been essential for isolating the effects of mechanical cues on stem cell activity, independent of biochemical signals. For example, mesenchymal stem cells can be driven towards osteogenic lineages via contact with a stiff substrate,[110] and experiments using collagen-coupled hydrogels demonstrated that this is independent of collagen density.[111]

Perhaps the greatest challenge for efforts to engineer ECM has been identifying a material capable of supporting the spectrum of cell behaviors

necessary for single stem cells to survive, divide, differentiate, and ultimately self-organize into organoid-like structures. While many efforts have optimized the properties of synthetic ECM towards supporting single-cell behaviors, [105,112,113] fewer reports have incorporated the full spectrum of chemical and physical properties necessary to support organoid growth and differentiation from stem cells. In a recent landmark study, Gjorevski and colleagues used a minimal, molecularly defined synthetic matrix to define the ECM properties that drive different stages of organoid formation from intestinal stem cells.[53] The authors systematically modulated matrix stiffness and degradation kinetics, while simultaneously grafting bioactive molecules onto PEG hydrogels to measure the individual effects of these proteins on intestinal stem cell survival, proliferation and self-organization. Interestingly, they found that the requisite matrix stiffness, degradation kinetics and ligand composition changed with development stage. Stem cell self-renewal and expansion required a stiff matrix modified with RGD peptides, but stem cell differentiation and organoid formation required a softer matrix containing laminin-111. To satisfy these requirements and design a matrix that supports all stages of organoid formation, the authors synthesized a laminin- and RGD-containing matrix that dynamically softens over time via the inclusion of hydrolytically degradable PEG monomers.

For future studies, it is exciting to consider how the various approaches described above could be combined. For example, tunable multicomponent matrices combined with high-throughput microfluidic platforms would allow rapid screening of key mechanical and biochemical properties within the stem cell

niche. Similarly, engineered ECMs combined with bioprinting or chemically programmed assembly techniques could be used to produce sophisticated custom matrices with defined 3D architecture that more closely mimic stem cell niches and the dynamic changes that occur during different developmental stages, aging and disease.

CONCLUSIONS

The use of organoid culture has helped to identify important niche components and has led to a deeper understanding of how the niche controls stem cell activity. The ability to manipulate organoid formation *in vitro* has enabled careful dissection of niche requirements, as demonstrated by reaggregation experiments that identified Paneth cells as a key member of the intestinal stem cell niche.[54] Such experiments in other tissues will be useful for identifying the cell types that comprise the ‘minimal niche', that is, the components that are necessary and sufficient for stem cell maintenance and tissue self-renewal. In addition to identifying feedback pathways from daughter to parent cells, organoids can also help to identify feedforward pathways between parent and daughter cells that help direct and maintain differentiation, as discussed in the case of Notch signaling in airway basal stem cells. [8,114] Controlled manipulation of organoid composition, including the numbers of stem cells and specific numbers and types of differentiated daughter cells, will allow interrogation of the feedforward and feedback loops that control cell fate in other tissues.

Emerging methods in organoid engineering will accelerate progress in our understanding of the stem cell niche by providing powerful means of interrogating organoids at the single cell level, as well as a means to guide the morphogenesis of organoids with significantly greater precision. This is crucial if we are to be able to use organoids in any meaningful way to address fundamental questions in developmental and regenerative biology.[115] These emerging technologies will facilitate studies that aim to address key concepts in stem cell biology, such as the influence of the niche on cell plasticity, as well as how the physical properties of the stem cell niche direct stem cell self-organization and, in turn, stem cell fate. For example, progenitors that are restricted to the enterocyte lineage during normal intestinal homeostasis can dedifferentiate to become stem cells and repopulate the crypt following damage.[116] Similarly, in the prostate both luminal and basal cells can produce *in vitro* organoids containing both lineages, but only basal cells give rise to all lineages when transplanted in vivo. [9,117] Together, these data clearly demonstrate that cell plasticity is context dependent. *In vitro* lineage tracing of single cells in organoids of precisely defined composition combined with *in vivo* models will help define the principles that govern dedifferentiation or interconversion between different cell identities and the long-term maintenance of tissue architecture and composition. As such, we predict that new engineering approaches will allow researchers to address fundamental questions that have been difficult to answer with less well-controlled organoid systems, or with *in vivo* lineage tracing experiments.

One intriguing possibility is that the mechanical forces that drive self-organization play a key role in directing cell fate, as stem cell localization is often highly stereotyped within a tissue. In the intestine, $Lgr5^+$ stem cells and supporting Paneth cells are located at the crypt base, and progenitors become committed to secretory or enterocyte lineages as they migrate away from the base. This same architecture is observed in intestinal organoids, where stem cell progeny self-organize into a crypt-like morphology containing $Lgr5^+$ stem cells and Paneth cells, with a transitional zone containing transit amplifying cells and regions of mature secretory and absorptive cells. [54,118] In the mammary gland, stem cells are enriched in the myoepithelial subpopulation and are thought to reside in a basal or suprabasal location.[7] Interestingly, basal cells normally divide parallel to the basement membrane, but deletion of β1-integrin from the basal compartment leads to random orientation of the mitotic spindle, an increased number of basal cell progeny located in the luminal compartment, and a loss of stem cells.[119] Together, these results suggest that specific localization within the niche is important for cell state maintenance**.** *In vitro* experiments using engineered organoids will allow direct measurement of the physical properties of individual cell types that comprise the niche, along with transcriptional and proteomic identification of key molecules that drive these properties, to enable systematic perturbation of niche organization. Furthermore, chemically programmed assembly methods can be used to directly manipulate cell positioning within the niche, and engineered ECMs can be used to manipulate mechanical, chemical and adhesive properties of the niche. These techniques

will play a crucial role in determining how mechanical cues are coordinated with spatially confined chemical cues to control cell activity and tissue homeostasis.

In this chapter, we have described the general organization and hormone-dependent signaling in the mammary gland, how organoid systems allow

systematic and in-depth interrogation of multicellular systems including the stem cell niche, and how state-of-the-art approaches for building synthetic niches will enable more direct quantification, modeling and testing of the processes that control cell activity. As a powerful complement to *in vivo* animal models, these current and emerging technologies will provide crucial insight into human tissue homeostasis and disease that could not be studied by other means.

REFERENCES

1. Simian, M.; Bissell, M. J. *J. Cell Biol.* **2017**, *216* (1), 31–40.

2. Clevers, H. *Cell* **2016**, *165* (7), 1586–1597.

3. Lancaster, M. A.; Knoblich, J. A. *Science* **2014**, *345* (6194), 1247125–1247125.

4. Scadden, D. T. *Cell* **2014**, *157* (1), 41–50.

5. Booth, B. W.; Mack, D. L.; Androutsellis-Theotokis, A.; McKay, R. D. G.; Boulanger, C. A.; Smith, G. H. *Proceedings of the National Academy of Sciences* **2008**, *105* (39), 14891–14896.

6. Jung, P.; Sato, T.; Merlos-Suárez, A.; Barriga, F. M.; Iglesias, M.; Rossell, D.; Auer, H.; Gallardo, M.; Blasco, M. A.; Sancho, E.; Clevers, H.; Batlle, E. *Nature Publishing Group* **2011**, *17* (10), 1225–1227.

7. Lim, E.; Vaillant, F.; Wu, D.; Forrest, N. C.; Pal, B.; Hart, A. H.; Asselin-Labat, M.-L.; Gyorki, D. E.; Ward, T.; Partanen, A.; Feleppa, F.; Huschtscha, L. I.; Thorne, H. J.; kConFab; Fox, S. B.; Yan, M.; French, J. D.; Brown, M. A.; Smyth, G. K.; Visvader, J. E.; Lindeman, G. J. *Nature Publishing Group* **2009**, *15* (8), 907–913.

8. Rock, J. R.; Onaitis, M. W.; Rawlins, E. L.; Lu, Y.; Clark, C. P.; Xue, Y.; Randell, S. H.; Hogan, B. L. M. *Proceedings of the National Academy of Sciences* **2009**, *106* (31), 12771–12775.

9. Karthaus, W. R.; Iaquinta, P. J.; Drost, J.; Gracanin, A.; van Boxtel, R.; Wongvipat, J.; Dowling, C. M.; Gao, D.; Begthel, H.; Sachs, N.; Vries, R. G. J.; Cuppen, E.; Chen, Y.; Sawyers, C. L.; Clevers, H. C. *Cell* **2014**, *159* (1), 163–175.

10. Sasai, Y. *Nature* **2013**, *493* (7432), 318–326.

11. Rosen, J. M. *Cold Spring Harbor Perspectives in Biology* **2012**, *4* (2), a013086–a013086.

12. Brisken, C.; O'Malley, B. *Cold Spring Harbor Perspectives in Biology* **2010**, *2* (12), a003178–a003178.

13. Clarke, R. B.; Howell, A.; Potten, C. S.; Anderson, E. *Cancer Research* **1997**, *57* (22), 4987–4991.

14. Allred, D. C. *Modern Pathology* **2010**, *23* (S2), S52–S59.

15. Graham, J. D.; Mote, P. A.; Salagame, U.; van Dijk, J. H.; Balleine, R. L.; Huschtscha, L. I.; Reddel, R. R.; Clarke, C. L. *Endocrinology* **2009**, *150* (7), 3318–3326.

16. Sternlicht, M. D. *Development* **2006**, *133* (6), 1203–1203.

17. Morancho, B.; Martínez-Barriocanal, Á.; Villanueva, J.; Arribas, J. *Breast Cancer Research* **2015**, 1–13.

18. Pond, A. C.; Bin, X.; Batts, T.; Roarty, K.; Hilsenbeck, S.; Rosen, J. M. *Stem Cells* **2012**, *31* (1), 178–189.

19. Lu, P.; Ewald, A. J.; Martin, G. R.; Werb, Z. *Developmental Biology* **2008**, *321* (1), 77–87.

20. Tanos, T.; Sflomos, G.; Echeverria, P. C.; Ayyanan, A.; Gutierrez, M.; Delaloye, J.-F.; Raffoul, W.; Fiche, M.; Dougall, W.; Schneider, P.; Yalcin-Ozuysal, O.; Brisken, C. *Sci Transl Med* **2013**, *5* (182), 182ra55.

21. Rajaram, R. D.; Buric, D.; Caikovski, M.; Ayyanan, A.; Rougemont, J.; Shan, J.; Vainio, S. J.; Yalcin-Ozuysal, O.; Brisken, C. *EMBO J.* **2015**, *34* (5), 641–652.

22. Brisken, C.; Hess, K.; Jeitziner, R. *Endocrinology* **2015**, *156* (10), 3442–3450.

23. Cai, C.; Yu, Q. C.; Jiang, W.; Liu, W.; Song, W.; Yu, H.; Zhang, L.; Yang, Y.; Zeng, Y. A. *Genes & Development* **2014**, *28* (20), 2205–2218.

24. Tarulli, G. A.; De Silva, D.; Ho, V.; Kunasegaran, K.; Ghosh, K.; Tan, B. C.; Bulavin, D. V.; Pietersen, A. M. *Breast Cancer Research* **2013**, *15* (1), R10.

25. Hanahan, D.; Weinberg, R. A. *Cell* **2011**, *144* (5), 646–674.

26. Dowsett, M.; Howell, A. *Nat. Med.* **2002**, *8* (12), 1341–1344.

27. Hammond, M. E. H.; Hayes, D. F.; Dowsett, M.; Allred, D. C.; Hagerty, K. L.; Badve, S.; Fitzgibbons, P. L.; Francis, G.; Goldstein, N. S.; Hayes, M.; Hicks, D. G.; Lester, S.; Love, R.; Mangu, P. B.; McShane, L.; Miller, K.; Osborne, C. K.; Paik, S.; Perlmutter, J.; Rhodes, A.; Sasano, H.; Schwartz, J. N.; Sweep, F. C. G.; Taube, S.; Torlakovic, E. E.; Valenstein, P.; Viale, G.; Visscher, D.; Wheeler, T.; Williams, R. B.; Wittliff, J. L.; Wolff, A. C. *Journal of Clinical Oncology* **2010**, *28* (16), 2784–2795.

28. Kiechl, S.; Schramek, D.; Widschwendter, M.; Fourkala, E.-O.; Zaikin, A.; Jones, A.; Jaeger, B.; Rack, B.; Janni, W.; Scholz, C.; Willeit, J.; Weger, S.; Mayr, A.; Teschendorff, A.; Rosenthal, A.; Fraser, L.; Philpott, S.; Dubeau, L.; Keshtgar, M.; Roylance, R.; Jacobs, I. J.; Menon, U.; Schett, G.; Penninger, J. M. *Oncotarget* **2016**, *8* (3), 3811–3825.

29. Kotsopoulos, J.; Singer, C.; Narod, S. A. *Breast Cancer Res Treat* **2016**, 1–6.

30. MD, P. M. G.; MD, G. P.; MD, P. C. D.; MD, M. H.; MD, P. R. G.; MD, P. R. J.; MD, V. W.; MD, M. B.; MD, F. H.; MD, E. M.; MD, V. B.-R.; MD, S. A.-M.; MD, F. F.; MD, P. C. M.; MD, P. S.; MD, B. M.; MD, G. G. S.; MD, D. M.; MD, R. E.; MD, D. E.; MD, P. J. B.; MD, F. K.; MSc, S. T.; MD, D. W.; PhD, C. F.; MD, P. C. F. S.; Group, A. B. A. C. C. S. *The Lancet* **2015**, *386* (9992), 433–443.

31. Okolicsanyi, R. K.; van Wijnen, A. J.; Cool, S. M.; Stein, G. S.; Griffiths, L. R.; Haupt, L. M. *J. Cell. Biochem.* **2014**, *115* (5), 967–976.

32. Sikora, M. J.; Jacobsen, B. M.; Levine, K.; Chen, J.; Davidson, N. E.; Lee, A. V.; Alexander, C. M.; Oesterreich, S. *Breast Cancer Research* **2016**, 1–16.

33. Tornillo, G.; Smalley, M. J. *J Mammary Gland Biol Neoplasia* **2015**, *20* (1-2), 63–73.

34. Zhang, J.; Tian, X.-J.; Xing, J. *J Clin Med* **2016**, *5* (4), 41.

35. Visbal, A. P.; LaMarca, H. L.; Villanueva, H.; Toneff, M. J.; Li, Y.; Rosen, J. M.; Lewis, M. T. *Developmental Biology* **2011**, *352* (1), 116–127.

36. O'Toole, S. A.; Machalek, D. A.; Shearer, R. F.; Millar, E. K. A.; Nair, R.; Schofield, P.; McLeod, D.; Cooper, C. L.; McNeil, C. M.; McFarland, A.; Nguyen, A.; Ormandy, C. J.; Qiu, M. R.; Rabinovich, B.; Martelotto, L. G.; Vu, D.; Hannigan, G. E.; Musgrove, E. A.; Christ, D.; Sutherland, R. L.; Watkins, D. N.; Swarbrick, A. *Cancer Research* **2011**, *71* (11), 4002–4014.

37. Janes, K. A. *Current Opinion in Biotechnology* **2016**, *39*, 120–125.

38. Parmar, H. *Endocrine Related Cancer* **2004**, *11* (3), 437–458.

39. Skardal, A.; Shupe, T.; Atala, A. *Drug Discovery Today* **2016**, *21* (9), 1399–1411.

40. Joshi, P. A.; Jackson, H. W.; Beristain, A. G.; Di Grappa, M. A.; Mote, P. A.; Clarke, C. L.; Stingl, J.; Waterhouse, P. D.; Khokha, R. *Nature* **2010**, *465* (7299), 803–807.

41. Clevers, H.; Loh, K. M.; Nusse, R. *Science* **2014**, *346* (6205), 1248012–1248012.

42. Zeng, Y. A.; Nusse, R. *Cell Stem Cell* **2010**, *6* (6), 568–577.

43. Bernfield, M. R.; Fell, P. E. *Proceedings of the National Academy of Sciences* **1967**, *58* (6), 2227–2234.

44. Steinberg, M. S.; Gilbert, S. F. *J. Exp. Zool.* **2004**, *301A* (9), 701–706.

45. Weiss, P.; Taylor, A. C. *Proc. Natl. Acad. Sci. U.S.A.* **1960**, *46* (9), 1177–1185.

46. Cerchiari, A. E.; Garbe, J. C.; Jee, N. Y.; Todhunter, M. E.; Broaders, K. E.; Peehl, D. M.; Desai, T. A.; Labarge, M. A.; Thomson, M.; Gartner, Z. J. *Proceedings of the National Academy of Sciences* **2015**, *112* (7), 2287–2292.

47. Chanson, L.; Brownfield, D.; Garbe, J. C.; Kuhn, I.; Stampfer, M. R.; Bissell, M. J.; Labarge, M. A. *Proceedings of the National Academy of Sciences* **2011**, *108* (8), 3264–3269.

48. Runswick, S. K.; O'Hare, M. J.; Jones, L.; Streuli, C. H.; Garrod, D. R. *Nat Cell Biol* **2001**, *3* (9), 823–830.

49. Gracz, A. D.; Williamson, I. A.; Roche, K. C.; Johnston, M. J.; Wang, F.; Wang, Y.; Attayek, P. J.; Balowski, J.; Liu, X. F.; Laurenza, R. J.; Gaynor, L. T.; Sims, C. E.; Galanko, J. A.; Li, L.; Allbritton, N. L.; Magness, S. T. *Nat Cell Biol* **2015**, *17* (3), 340–349.

50. Allazetta, S.; Lutolf, M. P. *Current Opinion in Biotechnology* **2015**, *35*, 86–93.

51. Magin, C. M.; Alge, D. L.; Anseth, K. S. *Biomed Mater* **2016**, *11* (2), 022001.

52. Todhunter, M. E.; Jee, N. Y.; Hughes, A. J.; Coyle, M. C.; Cerchiari, A.; Farlow, J.; Garbe, J. C.; Labarge, M. A.; Desai, T. A.; Gartner, Z. J. *Nat Meth* **2015**, *12* (10), 975–981.

53. Gjorevski, N.; Sachs, N.; Manfrin, A.; Giger, S.; Bragina, M. E.; Ordóñez-Morán, P.; Clevers, H.; Lutolf, M. P. *Nature* **2016**, *539* (7630), 560–564.

54. Sato, T.; van Es, J. H.; Snippert, H. J.; Stange, D. E.; Vries, R. G.; van den Born, M.; Barker, N.; Shroyer, N. F.; van de Wetering, M.; Clevers, H. *Nature* **2011**, *469* (7330), 415–418.

55. Discher, D. E.; Mooney, D. J.; Zandstra, P. W. *Science* **2009**, *324* (5935), 1673–1677.

56. Campàs, O.; Mammoto, T.; Hasso, S.; Sperling, R. A.; O'Connell, D.; Bischof, A. G.; Maas, R.; Weitz, D. A.; Mahadevan, L.; Ingber, D. E. *Nat Meth* **2014**, *11* (2), 183–189.

57. Choi, Y. Y.; Chung, B. G.; Lee, D. H.; Khademhosseini, A.; Kim, J.-H.; Lee, S.-H. *Biomaterials* **2010**, *31* (15), 4296–4303.

58. Karp, J. M.; Yeh, J.; Eng, G.; Fukuda, J.; Blumling, J.; Suh, K.-Y.; Cheng, J.; Mahdavi, A.; Borenstein, J.; Langer, R.; Khademhosseini, A. *Lab Chip* **2007**, *7* (6), 786–789.

59. Napolitano, A. P.; Dean, D. M.; Man, A. J.; Youssef, J.; Ho, D. N.; Rago, A. P.; Lech, M. P.; Morgan, J. R. *Scaffold-free three-dimensional cell culture utilizing micromolded nonadhesive hydrogels.*; 2007; Vol. 43, pp 494–496–500.

60. Ungrin, M. D.; Joshi, C.; Nica, A.; Bauwens, C.; Zandstra, P. W. *PLoS ONE* **2008**, *3* (2), e1565–12.

61. Nelson, C. M.; Vanduijn, M. M.; Inman, J. L.; Fletcher, D. A.; Bissell, M. J. *Science* **2006**, *314* (5797), 298–300.

62. Cerchiari, A.; Garbe, J. C.; Todhunter, M. E.; Jee, N. Y.; Pinney, J. R.; Labarge, M. A.; Desai, T. A.; Gartner, Z. J. *Tissue Engineering Part C: Methods* **2015**, *21* (6), 541–547.

63. Wang, X.; Sun, L.; Maffini, M. V.; Soto, A.; Sonnenschein, C.; Kaplan, D. L. *Biomaterials* **2010**, *31* (14), 3920–3929.

64. Stevens, K. R.; Ungrin, M. D.; Schwartz, R. E.; Ng, S.; Carvalho, B.; Christine, K. S.; Chaturvedi, R. R.; Li, C. Y.; Zandstra, P. W.; Chen, C. S.; Bhatia, S. N. *Nat Comms* **2013**, *4*, 1847–11.

65. Chan, H. F.; Zhang, Y.; Ho, Y.-P.; Chiu, Y.-L.; Jung, Y.; Leong, K. W. *Sci. Rep.* **2013**, *3* (1), 701–708.

66. Tumarkin, E.; Tzadu, L.; Csaszar, E.; Seo, M.; Zhang, H.; Lee, A.; Peerani, R.; Purpura, K.; Zandstra, P. W.; Kumacheva, E. *Integr. Biol.* **2011**, *3* (6), 653–11.

67. Collins, D. J.; Neild, A.; deMello, A.; Liu, A.-Q.; Ai, Y. *Lab Chip* **2015**, *15* (17), 3439–3459.

68. Edd, J. F.; Di Carlo, D.; Humphry, K. J.; Köster, S.; Irimia, D.; Weitz, D. A.; Toner, M. *Lab Chip* **2008**, *8* (8), 1262–1263.

69. Schoeman, R. M.; Kemna, E. W. M.; Wolbers, F.; van den Berg, A. *ELECTROPHORESIS* **2013**, *35* (2-3), 385–392.

70. Dura, B.; Servos, M. M.; Barry, R. M.; Ploegh, H. L.; Dougan, S. K.; Voldman, J. *Proc. Natl. Acad. Sci. U.S.A.* **2016**, *113* (26), E3599–E3608.

71. Allazetta, S.; Kolb, L.; Zerbib, S.; Bardy, J.; Lutolf, M. P. *Small* **2015**, *11* (42), 5647–5656.

72. Ma, S.; Natoli, M.; Liu, X.; Neubauer, M. P.; Watt, F. M.; Fery, A.; Huck, W. T. S. *J. Mater. Chem. B* **2013**, *1* (38), 5128–5129.

73. Khavari, A.; Nydén, M.; Weitz, D. A.; Ehrlicher, A. J. *Sci. Rep.* **2016**, *6* (1), 145–11.

74. Mao, A. S.; Shin, J.-W.; Utech, S.; Wang, H.; Uzun, O.; Li, W.; Cooper, M.; Hu, Y.; Zhang, L.; Weitz, D. A.; Mooney, D. J. *Nat Mater* **2016**, *16* (2), 236–243.

75. Attayek, P. J.; Ahmad, A. A.; Wang, Y.; Williamson, I.; Sims, C. E.; Magness, S. T.; Allbritton, N. L. *PLoS ONE* **2016**, *11* (4), e0153795–23.

76. Ellison, D.; Mugler, A.; Brennan, M. D.; Lee, S. H.; Huebner, R. J.; Shamir, E. R.; Woo, L. A.; Kim, J.; Amar, P.; Nemenman, I.; Ewald, A. J.; Levchenko, A. *Proc. Natl. Acad. Sci. U.S.A.* **2016**, *113* (6), E679–E688.

77. Gudapati, H.; Dey, M.; Ozbolat, I. *Biomaterials* **2016**, *102*, 20–42.

78. Murphy, S. V.; Atala, A. *Nat Biotechnol* **2014**, *32* (8), 773–785.

79. Truby, R. L.; Lewis, J. A. *Nature* **2016**, *540* (7633), 371–378.

80. Bhattacharjee, T.; Zehnder, S. M.; Rowe, K. G.; Jain, S.; Nixon, R. M.; Sawyer, W. G.; Angelini, T. E. *Science Advances* **2015**, *1* (8), e1500655–e1500655.

81. Hinton, T. J.; Jallerat, Q.; Palchesko, R. N.; Park, J. H.; Grodzicki, M. S.; Shue, H. J.; Ramadan, M. H.; Hudson, A. R.; Feinberg, A. W. *Science Advances* **2015**, *1* (9), e1500758–e1500758.

82. Livoti, C. M.; Morgan, J. R. *Tissue Engineering Part A* **2010**, *16* (6), 2051–2061.

83. Rago, A. P.; Chai, P. R.; Morgan, J. R. *Tissue Engineering Part A* **2009**, *15* (2), 387–395.

84. Tejavibulya, N.; Youssef, J.; Bao, B.; Ferruccio, T.-M.; Morgan, J. R. *Biofabrication* **2011**, *3* (3), 034110–034110.

85. Chandra, R. A.; Douglas, E. S.; Mathies, R. A.; Bertozzi, C. R.; Francis, M. B. *Angew. Chem. Int. Ed.* **2006**, *45* (6), 896–901.

86. Dutta, D.; Pulsipher, A.; Luo, W.; Yousaf, M. N. *J. Am. Chem. Soc.* **2011**, *133* (22), 8704–8713.

87. Hamon, M.; Ozawa, T.; Montagne, K.; Kojima, N.; Ishii, R.; Yamaguchi, S.; Nagamune, T.; Ushida, T.; Sakai, Y. *Biofabrication* **2011**, *3* (3), 034111–034111.

88. Hsiao, S. C.; Shum, B. J.; Onoe, H.; Douglas, E. S.; Gartner, Z. J.; Mathies, R. A.; Bertozzi, C. R.; Francis, M. B. *Langmuir* **2009**, *25* (12), 6985–6991.

89. Konagaya, S.; Iwata, H. *Biochimica et Biophysica Acta (BBA) - General Subjects* **2016**.

90. Zhao, W.; Loh, W.; Droujinine, I. A.; Teo, W.; Kumar, N.; Schafer, S.; Cui, C. H.; Zhang, L.; Sarkar, D.; Karnik, R.; Karp, J. M. *The FASEB Journal* **2011**, *25* (9), 3045–3056.

91. O'Brien, P. J.; Luo, W.; Rogozhnikov, D.; Chen, J.; Yousaf, M. N. *Bioconjugate Chem.* **2015**, *26* (9), 1939–1949.

92. Gartner, Z. J.; Bertozzi, C. R. *Proceedings of the National Academy of Sciences* **2009**, *106* (12), 4606–4610.

93. Selden, N. S.; Todhunter, M. E.; Jee, N. Y.; Liu, J. S.; Broaders, K. E.; Gartner, Z. J. *J. Am. Chem. Soc.* **2012**, *134* (2), 765–768.

94. Teramura, Y.; Minh, L. N.; Kawamoto, T.; Iwata, H. *Bioconjugate Chem.* **2010**, *21* (4), 792–796.

95. Weber, R. J.; Liang, S. I.; Selden, N. S.; Desai, T. A.; Gartner, Z. J. *Biomacromolecules* **2014**, *15* (12), 4621–4626.

96. Huang, H.-L.; Hsing, H.-W.; Lai, T.-C.; Chen, Y.-W.; Lee, T.-R.; Chan, H.-T.; Lyu, P.-C.; Wu, C.-L.; Lu, Y.-C.; Lin, S.-T.; Lin, C.-W.; Lai, C.-H.; Chang, H.-T.; Chou, H.-C.; Chan, H.-L. *J. Biomed. Sci.* **2010**, *17* (1), 36.

97. Rios, A. C.; Fu, N. Y.; Lindeman, G. J.; Visvader, J. E. *Nature* **2014**, *506* (7488), 322–327.

98. Van Keymeulen, A.; Rocha, A. S.; Ousset, M.; Beck, B.; Bouvencourt, G.; Rock, J.; Sharma, N.; Dekoninck, S.; Blanpain, C. *Nature* **2011**, *479* (7372), 189–193.

99. Wuidart, A.; Ousset, M.; Rulands, S.; Simons, B. D.; Van Keymeulen, A.; Blanpain, C. *Genes & Development* **2016**, *30* (11), 1261–1277.

100. Hughes, C. S.; Postovit, L. M.; Lajoie, G. A. *Proteomics* **2010**, *10* (9), 1886–1890.

101. Kleinman, H. K.; McGarvey, M. L.; Hassell, J. R.; Star, V. L.; Cannon, F. B.; Laurie, G. W.; Martin, G. R. *Biochemistry* **1986**, *25* (2), 312–318.

102. Kleinman, H. K.; Martin, G. R. *Seminars in Cancer Biology* **2005**, *15* (5), 378–386.

103. Seliktar, D. *Science* **2012**, *336* (6085), 1124–1128.

104. Zhu, J. *Biomaterials* **2010**, *31* (17), 4639–4656.

105. Enemchukwu, N. O.; Cruz-Acuña, R.; Bongiorno, T.; Johnson, C. T.; García, J. R.; Sulchek, T.; García, A. J. *J. Cell Biol.* **2016**, *212* (1), 113–124.

106. Darnell, M.; Young, S.; Gu, L.; Shah, N.; Lippens, E.; Weaver, J.; Duda, G.; Mooney, D. *Adv Healthc Mater* **2016**.

107. Kloxin, A. M.; Kasko, A. M.; Salinas, C. N.; Anseth, K. S. *Science* **2009**, *324* (5923), 59–63.

108. Mosiewicz, K. A.; Kolb, L.; van der Vlies, A. J.; Lutolf, M. P. *Biomater. Sci.* **2014**, *2* (11), 1640–1651.

109. Sunyer, R.; Jin, A. J.; Nossal, R.; Sackett, D. L. *PLoS ONE* **2012**, *7* (10), e46107–e46109.

110. Engler, A. J.; Sen, S.; Sweeney, H. L.; Discher, D. E. *Cell* **2006**, *126* (4), 677–689.

111. Wen, J. H.; Vincent, L. G.; Fuhrmann, A.; Choi, Y. S.; Hribar, K. C.; Taylor-Weiner, H.; Chen, S.; Engler, A. J. *Nat Mater* **2014**, *13* (10), 979–987.

112. Chaudhuri, O.; Gu, L.; Klumpers, D.; Darnell, M.; Bencherif, S. A.; Weaver, J. C.; Huebsch, N.; Lee, H.-P.; Lippens, E.; Duda, G. N.; Mooney, D. J. *Nat Mater* **2016**, *15* (3), 326–334.

113. Green, J. J.; Elisseeff, J. H. *Nature* **2016**, *540* (7633), 386–394.

114. Pardo-Saganta, A.; Tata, P. R.; Law, B. M.; Saez, B.; Chow, R. D.-W.; Prabhu, M.; Gridley, T.; Rajagopal, J. *Nature* **2015**, *523* (7562), 597–601.

115. Huch, M.; Knoblich, J. A.; Lutolf, M. P.; Martinez-Arias, A. *Development* **2017**, *144* (6), 938–941.

116. Tetteh, P. W.; Basak, O.; Farin, H. F.; Wiebrands, K.; Kretzschmar, K.; Begthel, H.; van den Born, M.; Korving, J.; de Sauvage, F.; van Es, J. H.; van Oudenaarden, A.; Clevers, H. *Cell Stem Cell* **2016**, *18* (2), 203–213.

117. Goldstein, A. S.; Lawson, D. A.; Cheng, D.; Sun, W.; Garraway, I. P.; Witte, O. N. *Proceedings of the National Academy of Sciences* **2008**, *105* (52), 20882–20887.

118. Sato, T.; Vries, R. G.; Snippert, H. J.; van de Wetering, M.; Barker, N.; Stange, D. E.; van Es, J. H.; Abo, A.; Kujala, P.; Peters, P. J.; Clevers, H. *Nature* **2009**, *459* (7244), 262–265.

119. Taddei, I.; Deugnier, M.-A.; Faraldo, M. M.; Petit, V.; Bouvard, D.; Medina, D.; Fässler, R.; Thiery, J. P.; Glukhova, M. A. *Nat Cell Biol* **2008**, *10* (6), 716–722.

FIGURES

Figure 1-1. Advantages of organoid models for studying adult stem cells.

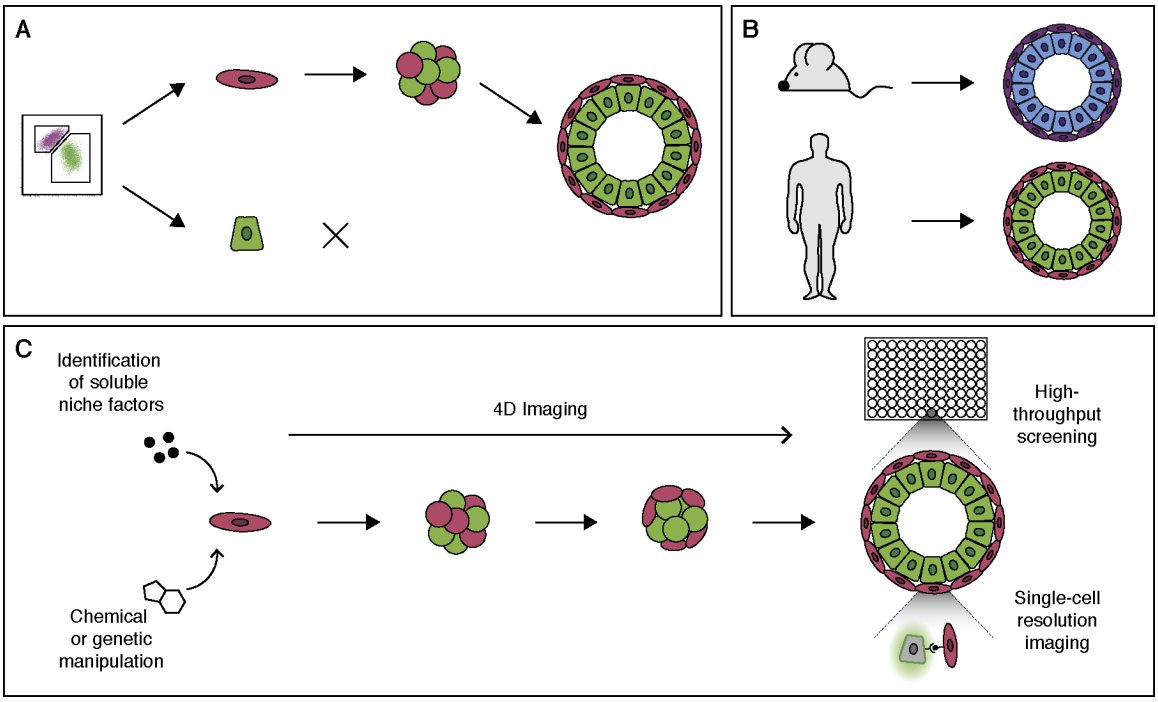

(A) Organoids can be derived from human cells as well as non-human cells such as mouse or zebrafish, which allows modeling of human-specific stem cell biology and the identification of differences between human and non-human tissues. (B) *In vitro* culture allows in-depth experimental perturbation and imaging of stem cells in their surrounding niche. Different approaches include tightly controlled chemical or genetic manipulation, 3D imaging of live tissues over time (4D imaging), high-throughput combinatorial screening, and single-cell resolution imaging to analyze specific cell-cell interactions.

Figure 1-2. Hormone Dependent Growth on the Mammary Gland.

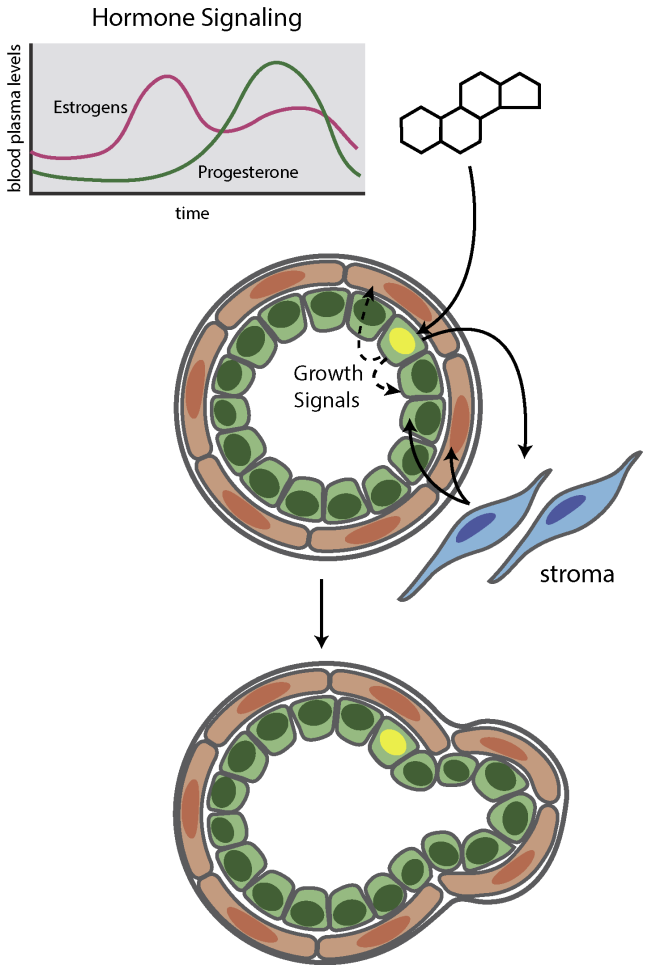

Hormone-sensing cells are restricted to the luminal epithelial lineage (green) and integrate cyclic hormonal signals, such as progesterone. These signals drive proliferation in neighboring cells via paracrine signaling both within the epithelium and through stromal–epithelial cross-talk. This key regulator of mammary gland growth is preserved but dysregulated in many breast cancers.

Figure 1-3. Advantages of engineered organoids for studying physiology.

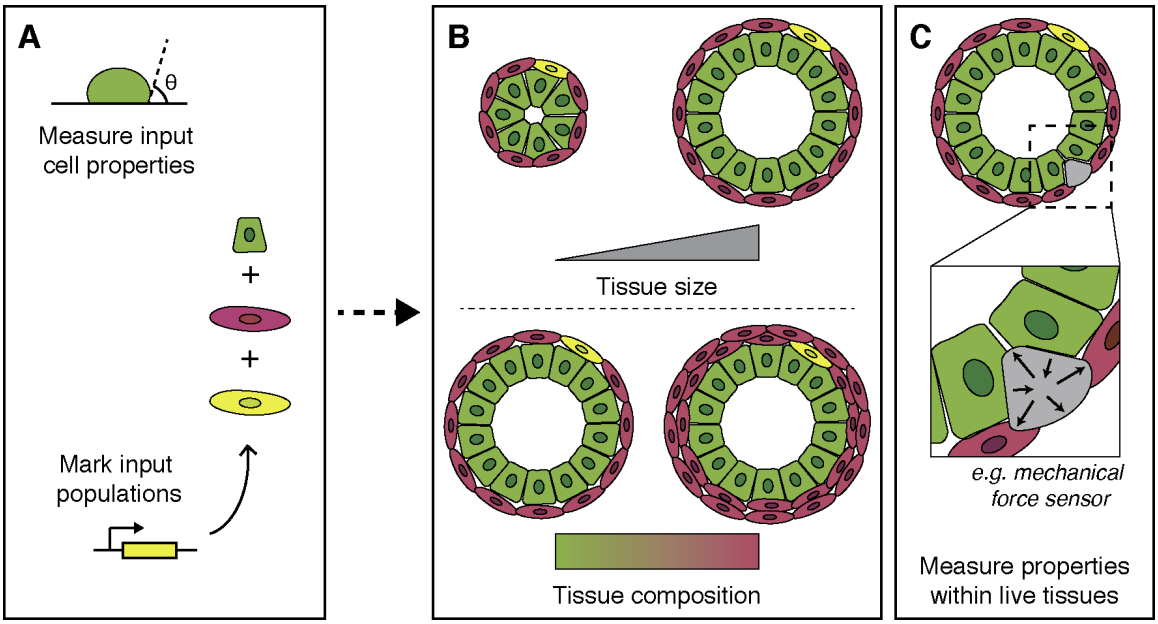

(A) Constructing organoids from purified cellular components allows the direct measurement of input cell properties and labeling of different input populations. (B) In addition to the advantages of classical organoid models (outlined in Fig. 1), controlled organoid engineering provides tight experimental control over the numbers and types of cells in the resulting tissue. (C) Engineered organoids can incorporate non-cellular material, such as sensors that dynamically measure properties such as mechanical forces and signaling pathway activation within live tissues.

Figure 1-4: Technologies to Reconstitute Organoids From Purified Cell Populations.

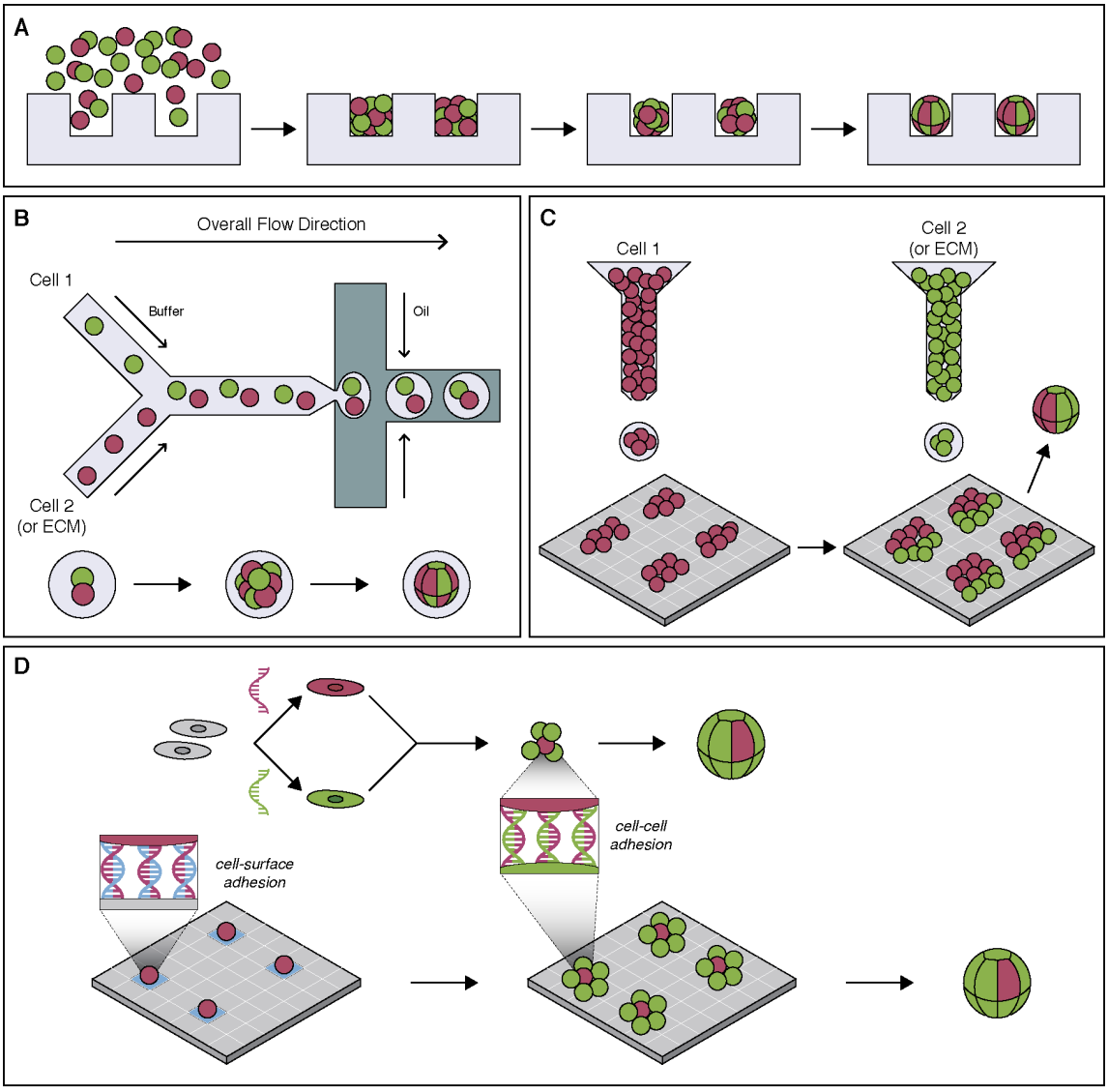

(A) Microwells. Cells can be centrifuged, flowed or injected into arrays of microwells to produce organoids that conform to the size and shape of the microwell. (B) Microfluidics. Individual cells or ECM components can be captured in aqueous droplets and combined to produce precisely sized spheroids that are

amenable to high-throughput recovery and analysis. (C) 3D bioprinting. Cells suspensions or ECM components can be used as a printable 'ink', with control in the *x*, *y* plane over individual components. Multiple 'inks' can be loaded into the printer to create complex, patterned tissues. (D) Chemically programmed assembly. Cell surfaces can be chemically modified with single-stranded DNA or other bio-orthogonal molecules to program adhesion to surfaces or other cells, independent of endogenous cellular machinery. This technique can achieve single-cell resolution to create organoids with precisely controlled cell-cell interactions. (E) Engineered ECMs. Polymer hydrogels such as PEG can be tuned over a range of stiffnesses and topologies by varying monomer concentration, molecular weight and degree of crosslinking. Cell adhesion ligands (e.g. RGD integrin-recognition sequences) or proteolytically degradable sequences can be engineered back into the system.

CHAPTER 2

FATTY-ACID MODIFIED DNA FOR SPECIFIC ASSEMBLY OF MICROTISSUES

Source: The following chapter was previously published as: Efficient Targeting of Fatty-Acid Modified Oligonucleotides to Live Cell Membranes through Stepwise Assembly Robert J. Weber, Samantha I. Liang, Nicholas S. Selden, Tejal A. Desai, and Zev J. Gartner, Biomacromolecules ***2014*** **15** *(12), 4621-4626 DOI: 10.1021/bm501467h*

Contributions: Nicholas Selden and Samantha Liang initiated the project. I followed up on their initial findings and performed the majority of subsequent the experiments, with help from Samantha Liang. Zev Gartner, Tejal Desai, and I wrote the manuscript with editorial input from all authors. Zev Gartner and Tejal supervised the project.

INTRODUCTION

Lipid-modified oligonucleotides(1-3) facilitate uptake of siRNA,(4) target DNA nanostructures to lipid bilayers,(5) program assembly of 3D microtissues,(6, 7) enable preparation of live single cell microarrays,(8-10) and function as vaccine adjuvants and immunotherapeutics.(11, 12) These uses are predicated on rapid, efficient, and stable partitioning of these amphiphilic molecules from solution into live cell membranes.(13) We recently reported an approach for incorporating dialkylglycerol modified oligonucleotides (DAG) into cell membranes.(10) DAG is useful for targeting DNA to the membranes of most cell lines, but suffers when targeting primary or embryonic stem cells (ESCs). Moreover, DAG and other lipid-modified oligonucleotides slowly leave the cell membrane and establish an equilibrium with the surrounding medium.(14, 15) This loss by re-equilibration limits the ultimate efficiency of incorporation into the bilayer over time.

To improve the concentration of lipid-anchored oligonucleotides in cell membranes, we reasoned that increasing the dialkyl anchor hydrophobicity would increase its thermodynamic stability when inserted into cell membranes.(9, 14-16) Indeed, previous studies demonstrated that longer lipids are more stable than shorter lipids when reconstituted into synthetic lipid bilayers.(3) However, we found that DAG incorporation into live cell membranes (as opposed to synthetic systems) was exquisitely sensitive to alkyl chain length. The addition of even two methylenes completely inhibited partitioning into cell membranes.(9) We hypothesized that this was due to a competing self-aggregation reaction(17, 18)

and thus sought an alternative means of introducing greater hydrophobicity to the lipid anchors without aggregation.

RESULTS AND DISCUSSION

Previous reports show that complementary cholesterol-bearing oligonucleotides can be stably targeted to liposomes and supported lipid bilayers via hybridization.(19) We envisioned further increasing the hydrophobicity of the membrane anchors to further stabilize duplexes in live cells, rather than artificial lipid bilayers. To prevent aggregation of these more hydrophobic molecules, however, the two strands would need to be added sequentially to cells, rather than as a prehybridized duplex. Under conditions of stepwise addition, a first Anchor strand (Anch) partitions into the lipid bilayer but remains in rapid equilibrium with the medium. A second, co-Anchor (cA) strand is subsequently added and also establishes rapid equilibrium between the lipid bilayer and the medium. However, upon encountering the first strand through diffusion in the phospholipid bilayer, the two strands hybridize, increase the total hydrophobicity of the now doubly anchored duplex and, thus, slowing their exchange with the medium (Scheme 1).

To explore this strategy, we used fatty acid amides (FA) as more synthetically tractable membrane anchors than previously reported phospholipids or cholesterol.(19) Fatty acids are widely commercially available and do not require chemical modification before coupling. Additionally, the conjugation

reaction to DNA is not highly water sensitive and requires only one reverse phase purification step after coupling.

Consistent with past studies,(13, 20) a single FA anchor does not stably label cell membranes when compared to DAG or doubly cholesterol-anchored DNA (Figure 2-S1). For example, a 100 base Anch strand linked to stearic acid (C18) via a 5′ amide (5′-Anch100-C18) did not yield significant DNA incorporation after incubation with cells and washing (Figure 2-1, column 3). However, addition of a second, 20 base complementary coanchor (cA-) strand linked to palmitic acid (C16) via a 3′ amide (3′-cA20-C16) dramatically increased cell labeling to near that of the DAG and doubly anchored cholesterol (Figure 2-1, column 6 and Figure 2-S1). No increase was seen upon addition of a noncomplementary 3′-cA20-C16 strand (Figure 2-1, Column 5), indicating that at least two FA anchors, linked noncovalently through Watson–Crick base pairing in the “lock” region (Scheme 2-1a), are necessary for stable incorporation.

We found that the number of base pairs in the lock region correlated with initial labeling and retention of oligonucleotides over time, both at 0 and 37 °C. This effect saturated between 15 and 20 bases (Figure 2-S2). Labeling was dose-dependent and occurred without altering cell viability over the examined range of 0.5 to 5 μM (Figure 2-S2). Encouragingly, even these unoptimized molecules were capable of programming cell–cell and cell−surface adhesion of model cell lines with results comparable to DAG when incorporating 60 base polythymine spacers (Figure 2-S3).

These initial findings suggested we could achieve additional improvements in cell membrane incorporation by increasing the length and thus hydrophobicity of FA anchors. We therefore synthesized a series of 5′-Anch100 strands conjugated to saturated FAs between 16 and 24 carbons in length. These Anch strands behaved as predicted when added stepwise to cells in concert with 3′-cA20-C16. Increased lipophilicity of FAs enhanced the labeling efficiency and showed substantial improvement over both DAG and cholesterol linked oligonucleotides (Figure 2-2A). Anch strands with enhanced hydrophobicity also demonstrated improved retention over time at physiological temperature (Figure 2-S4). Unlike the 5′-Anch100-C18 and 3′-cA20-C16 combination, stepwise addition of more hydrophobic Anch and cA strands was essential for preventing competing aggregation reactions (Figure 2-2B). Prehybridizing 5′-Anch100-C24 and 3′-cA20-C16 strands led to dramatically reduced cell membrane incorporation compared to prehybridized 5′-Anch100-C18 and 3′-cA20-C16 strands (Figure 2-2B). Together, these results support the notion that splitting the hydrophobicity of dual-anchored species across two complementary oligonucleotides added stepwise to cells prevents aggregation and improves labeling.

These data suggested we could achieve further increases in cell labeling and stability by increasing the hydrophobicity of the cA strand in addition to the Anch strand. Surprisingly, increasing the hydrophobicity of the cA strand anchors did not yield additional gains in cell labeling. For instance, stepwise addition of 5′-Anch100-C24 and 3′-cA20-C24, which maximizes hydrophobicity for both

strands, actually decreased DNA incorporation when compared to 5′-Anch100-C24/3′-cA20-C16. We investigated this effect by assaying a panel of molecules in which the fatty acid on the Anch and cA strands was varied systematically and independently. We found that increasing hydrophobicity specifically on the coanchor strand decreased labeling (Figure 2-2C). Indeed, 5′-Anch100-C24/3′-cA20-C16 inserted far more efficiently into cell membranes than 5′-Anch100-C16/3′-cA20-C24 despite containing identical number of phosphodiester bonds and methylene groups.

To explain this trend, we hypothesized that the ratio of anchor hydrophobicity to oligonucleotide length (and thus charge) determines the extent of aggregation. If this were the case, short oligonucleotides would be more prone to aggregation than equivalently modified longer oligonucleotides. To test this notion, we used dynamic light scattering (DLS) to examine the relationship between FA anchor length, oligonucleotide length, and relative aggregation. Both scattered light intensity (Figure 2-3A) and particle size (Figure 2-S5) correlated with the length of the FA conjugated to the cA strand. In contrast, very little light scattering was observed for any FA conjugated to the 100 base anchor strand (Figure 2-3B). These results suggested that adding additional bases to the cA strand, increasing its net size and charge, would destabilize aggregates through Coulombic or steric repulsion while simultaneously allowing for increased hydrophobicity of its FA anchor. We therefore synthesized a series of 3′-cA20-C24 strands incorporating an additional 10, 20, or 30 bases at the 5′ end. Consistent with our expectations, DLS revealed an inverse relationship between

the number of bases and aggregation (Figure 2-3B). Moreover, the best of these molecules, 3′-cA50-C24, increased cell labeling in combination with 5′-Anch100-C24 to nearly 7-fold of DAG (Figure 2-3C). This combination of molecules also showed a dramatic increase in lifetime at the cell surface compared to DAG (Figure 2-3D). We calculated that the initial rate of decay of these fully optimized strands from the cell surface was nearly 100-fold lower than DAG.

Given the improved cell labeling enabled by stepwise addition of C24 conjugated oligonucleotides, we investigated whether they could be used for programming cell–cell and cell–surface adhesion for cell types that were inaccessible with DAG. Using even unoptimized 5′-Anch100-C24/3′-cA20-C16, we found efficient adhesion between ESCs and complementary 7 μm diameter spots of DNA patterned on glass surfaces, allowing the preparation of live, single cell microarrays with more than 95% occupancy. By comparison, DAG yielded only 40% binding using identical conditions (Figure 2-4A). We also used stepwise assembly of FA-anchored DNA to prepare 3D mosaic epithelial tissues from nonmalignant human mammary epithelial cell lines (MCF10A). Aggregates were purified by fluorescence activated cell sorting (FACS) prior to incubation under 3D culture conditions for 48 h in Matrigel. Consistent with previous reports,(21, 22) aggregates condensed into spherical microtissues with appropriately positioned markers of cell polarity such as α6-integrin (basal) and actin (lateral; Figure 2-4B). The 5′-Anch100-C24/3′-cA20-C16 combination showed improved labeling compared to DAG in several low passage primary cells and a pancreatic β-cell line (Figures 2-4C and 2-S6). We therefore used this combination to

prepare aggregates of controlled topology from mouse ESCs and pancreatic β-cells (Figure 2-4C). Previous reports have demonstrated that heterotypic aggregates of this general form can be used to differentiate stem cells into a variety of useful cell types.(23-25) Thus, small 3D tissues of this type may find utility in regenerative medicine or basic science research.

CONCLUSION

In conclusion, stepwise assembly of membrane-anchored oligonucleotides is a modular strategy for targeting DNA to cell membranes with improved efficiency and stability. Insertion of oligonucleotide duplexes into membranes occurs via two FA-anchors with higher net lipophilicity compared to previously reported anchors. Competing self-aggregation is prevented by separating the dual anchors between two molecules that are added sequentially to cells, as well as by balancing the ratio of hydrophobicity to oligonucleotide length. This strategy facilitates new applications such as DNA-mediated adhesion in primary cells, murine ESCs, and pancreatic β cells, cell types that show little to no labeling with DAG. An additional benefit of these molecules is their streamlined synthesis compared to previous methods. We anticipate that the structure/function relationships defined here will prove useful in other applications utilizing lipid-modified oligonucleotides or amphiphiles including vaccine adjuvants, siRNA delivery, and structural DNA nanotechnology.

METHODS

SYNTHESIS OF LIPID-MODIFIED OLIGONUCLEOTIDES

Hexadecanoic (Palmitic) acid, octadecanoic (Stearic) acid, icosanoic (Arachidic) acid, docosanoic (Behenic) acid, tetracosanoid (Lignoceric) acid, N,N-diisopropylethylamine (DIPEA), N,N-diisopropylchlorophosphoramidite (DIPC), N,N-dimethylformamide (DMF), methylamine, ammonium hydroxide, and piperidine were obtained from Sigma-Aldrich. HPLC grade acetonitrile, triethylamine, acetic acid, and dichloromethane (DCM) were obtained from Fisher Scientific. Monomethoxytritylamino)hexyl-(2-cyanoethyl)-(N,N-diisopropyl)-phosphoramidite (amine phosphoramidite), standard phosphoramidites, and DNA synthesis reagents were obtained from Azco Biotech. Controlled pore glass (CPG) support, 1-O-dimethoxytrityl-hexyl-disulfide,1′-[(2-cyanoethyl)-(N,N-diisopropyl)]-phosphoramidite, 10-O-[1-propyl-3-N-carbamoylcholesteryl]-triethylene glycol-1-[(2-cyanoethyl)-(N,N-diisopropyl)]-phosphoramidite (5′-cholesterol-TEG phosphoramidite), (1-dimethoxytrityloxy-3-O-(N-cholesteryl-3-aminopropyl)-triethylene glycol-glyceryl-2-O-succinoyl-long chain alkylamino-CPG (3′-cholesterol-TEG CPG), and 2-dimethoxytrityloxymethyl-6-fluorenylmethoxycarbonylamino-hexane-1-succinoyl-long chain alkylamino-CPG (3′-amino-modifier C7 CPG), and synthesis columns were obtained from Glen Research. All materials were used as received from manufacturer.

Oligonucleotides were synthesized on an Applied Biosystems Expedite 8909 DNA synthesizer. Amino and cholesterol modified 'DNA strands were synthesized using amine and cholesterol phosphoramidites (100 mM), respectively, using a custom 15 min coupling protocol. For the polythymine regions of the anchor strands (Anch), the capping step was omitted in order to

maximize yield. After synthesis of 5′ amino-modified DNA, the MMT protecting group was deprotected manually on the synthesizer by priming alternately with deblock and dry acetonitrile three times and watching for yellow elution. To ensure complete deprotection of the MMT group, the 5′ solid supports were also resuspended in a solution of 20% acetic acid/80% water(1) shaking for 1 h at room temperature. The solid support was subsequently washed repeatedly with DMF, DCM, and acetonitrile with acetonitrile as the final wash and then dried with a speedvac system. For the 3′ amino-modified CPG, a solution of 20% piperidine in dimethylformamide was prepared and used to deprotect the CPG support for 10 min at room temperature, followed by DCM and DMF washes with DCM as the final wash. This procedure was repeated twice more to ensure complete deprotection of the FMOC protecting group prior to coupling to the fatty acid. Fatty acid conjugated oligonucleotides were synthesized by coupling the carboxylic acid moiety of the fatty acid to amino modified oligonucleotides with a 3′ or 5′ free amine while on the solid support. The solid support was transferred to an eppendorf tube and resuspended in a solution of dichloromethane containing 200 mM fatty acid, 400 mM DIPEA, and 200 mM DIPC. The eppendorf tubes were sealed with parafilm, crowned with a cap lock, and shaken overnight at room temperature. The next morning, they were washed with DCM and DMF repeatedly and then cleaved off the solid support

Oligonucleotides were cleaved from solid support with a 1:1 mixture of ammonium hydroxide/40% methylamine (AMA) for 1 h at 65 °C with a cap lock followed by evaporation of AMA with a speedvac system. Cleaved

oligonucleotides were filtered through 0.2 μm Ultrafree-MC Centrifugal Filter Units (Millipore) to remove any residual CPG support before HPLC purification. Fatty acid modified oligonucleotides were purified from unmodified oligonucleotides by reversed-phase high-performance liquid chromatography (HPLC) using an Agilent 1200 Series HPLC System equipped with a diode array detector (DAD) monitoring at 260 and 300 nm. Purifications used 100 mM triethylamine acetate (TEAA, pH 7) H2O/acetonitrile as a mobile phase on a C8 column (Hypersil Gold, Thermo Scientific) running a gradient between 8 and 95% acetonitrile over 30 min. Pure fractions were collected manually and lyophilized. The resulting powder was then resuspended in distilled water and lyophilized again three more times to remove residual TEAA salts prior to use. Purified FA-modified oligonucleotides were resuspended in distilled water and concentrations were determined by measuring their absorbance at 260 nm on a Thermo-Fischer NanoDrop 2000 series. An aliquot of these stocks was reinjected on the HPLC to ensure >95% purity. If purity was <95%, HPLC purification was repeated. Additionally, select strands were also analyzed by MALDI-TOF (see below). The dialkylglycerol (DAG)-modified oligonucleotides were prepared as previously described.(10) Stocks of 250 μM were prepared and from them aliquots of 50 μM were prepared for day-to-day use in order to minimize repeated freeze–thaw cycles.

CELL LINES AND CELL CULTURE

Jurkats were obtained from ATCC (Clone E6–1) ATCC TIB-152 and were grown in suspension using RPMI 1640 media supplemented with 10% fetal

bovine serum by volume (UCSF Cell Culture Facility) to a density of 106 cells per mL. The 832–13 pancreatic beta islet cells were obtained from Dr. Tejal Desai (UCSF) at passage 51 and were grown in RPMI 1640 supplemented with 10% fetal bovine serum, 63.7 mg/L penicillin G, 100 mg/L streptomycin SO4, 1 mM sodium pyruvate, and 70 nM 2-mercaptoethanol (UCSF Cell Culture Facility) to approximately 70% confluency on 75 cm2 tissue culture plastic. Dr. Matt Thomson (UCSF) generously provided 46C mouse ES cells. The cells were grown on gelatinized tissue culture plates using N2B27 media supplemented with 1000 U/mL LIF, 3 μM CHIR99021 and 1 μM PD0325901. The cells were lifted from their substrate using accutase and grown to a density of 2–3 x106 cells per cm2. MCF10A cells were kindly provided by Professor Jayanta Debnath (UCSF) and were cultured as previously described.(27) Low passage, primary fibroblast, HMEC, and pre-adipocyte cell lines were provided by Jim Garbe (LBNL) and cultured in M87 media supplemented with cholera toxin.

DNA Labeling of Cells and Quantification of Cell Surface Oligonucleotides

For experiments, unless otherwise noted, Jurkat cells were used. Cells were pelleted at 1000 g resuspended in calcium and magnesium-free PBS (UCSF Cell Culture Facility) three times, with a final resuspension volume of 48 μL of PBS per 106 cells. Resuspended cells were labeled with single-stranded DNA by the addition of 1 μL of a 50 μM solution of the anchor strand in water. Cells were gently agitated by gentle vortexing for 5 min at room temperature. Subsequently, 1 μL of a 50 μM solution of the coanchor strand in water was

added, bringing both strands to a final concentration of 1 μM. Cells were again gently agitated by slow vortexing for 5 min at room temperature. The cells were then pelleted and resuspended three times in ice-cold PBS to remove unbound or excess oligonucleotides. To quantify the extent of cell surface labeling, cells were incubated with 100 μL of a 20mer complementary 6-FAM modified oligonucleotide (1 μg/mL, Operon), which annealed to the most distal portion of the anchor strand. The strand was incubated for 30–45 min at 4 °C, protected from light. Cells were pelleted and resuspended one time in ice cold PBS before pelleting and resuspending in 100 μL per 106 cells of LIVE/DEAD Fixable Cell Stain (Invitrogen, used per manufacturers instructions) for 15 min at 4 °C protected from light. Cells were washed one last time with ice cold PBS before flow cytometry analysis. Flow cytometry was performed on a FACSCalibur (BD Biosciences, UCSF Laboratory for Cell Analysis) and the data was analyzed using FlowJo software package (Tree Star, Inc.). For stability time course experiments, cells were incubated at 37 °C for the designated amount of time in the presence of serum-free RPMI 1640 before incubating with the fluorescent, complementary oligonucleotide. For the preannealing experiment, a 1 μM solution of C18/C16 and a 0.3 μm solution of C22/C16 fatty acid modified strands in room temperature PBS was prepared and gently agitated for 10 min at room temperature. This solution was used to resuspend the cell pellet after the final wash from media and gently agitated for an additional 10 min at room temperature. This was compared to normal labeling using these same strands at these same concentrations. All reported values are the average of three or more

independent measurements, with error bars indicating standard deviations. Graphs were produced using the Prism software package (Graphpad). The heatmap was produced using the R software package (R), specifically using the ggplot2 library.

Measuring Aggregation by Dynamic Light Scattering (DLS)

PBS CMF (UCSF CCF) was filtered by a 0.2 μm vacuum filter. Stock solutions of 250 μM ss-DNA strands were diluted to 1 μM with this filtered PBS prior to transfer to cuvette for measuring by DLS on a Wyatt Technology DynaPro Protein Solutions utilizing the DYNAMICS software package ver 6.10.1.2. Particle size was determined by cumulants analysis. All samples were prepared separately and measured in triplicate.

Surface Preparation for Cell Binding

Lyophilized 5′-amino-modified DNA was resuspended in a buffer of 60 mM sodium citrate, 450 mM sodium chloride, pH = 7.0. DNA was patterned onto aldehyde-silanized glass (Schott) using a micropipette (Figure 2-4c) or a Nano eNabler (BioForce Nanosciences; Figure 2-4d,e). Slides were reduced with $NaBH_4$ (Sigma) and passivated with both SigmaCote (Sigma) and Pluronic F108 acid before use. Cells labeled with lipid-DNA were allowed to settle onto patterned glass within a PDMS-based flow cell for 30 min. Flow cells were flushed with ice cold PBS, and only cells hybridized to the surface via DNA were retained. Patterned cells were imaged using phase contrast settings and

reconstructed using tiling algorithm (Zen Software, Zeiss). For experiments with mouse embryonic stem cells, no sigmacote was used for surface passivation.

Programmed Cell Assembly

For quantification of programmed assembly efficiency, CellTracker Green CMFDA and CellTrace Far Red DDAO-SE (Invitrogen) stocks were prepared to a concentration of 10 mM in anhydrous DMSO. Cells were resuspended in 10 μM stain in serum-free media for 30 min at 37 °C followed by 15 min in media supplemented with 10% fetal bovine serum before proceeding through the labeling steps described above. After washing away unreacted DNA, cells were resuspended at 1 × 106 cells/mL. Green cells were mixed with far-red cells at a ratio of 1:60 with 106 cells per 200 μL of ice cold PBS. Mixtures were then agitated at 150 rpm for 10 min in an Ultra-Low Attachment 24-well plate (Corning). This mixture was pelleted and resuspended in ice cold PBS before quantifying via flow cytometry or sorting via fluorescence activated cell sorting (FACS). The labels were reversed to ensure unbiased quantitation. For programmed assemblies of the embryonic stem and pancreatic beta islet cells, CellTracker Green CMFDA was used to stain the ESCs and the islet cells were left unstained. were subsequently labeled with anchor strands 1 and 2, respectively, and assembled as described above. Clusters containing at least 1 green cell were purified from the unassembled cell population using a FACSAria II (UCSF Laboratory for Cell Analysis).

MCF10A Acinus Formation and Imaging

MCF10A cells were cultured as described above. Cells were collected and stained with CellTracker Green CMFDA, as described above or left unstained. The green and unstained cells were subsequently labeled with anchor strands 1 and 2, respectively, and assembled as described above. Clusters containing at least 1 green cell were purified from the unassembled cell population using a FACSAria II (UCSF Laboratory for Cell Analysis) and grown for 48 h in 3D on-top cultures in 8-well chamber slides (Lab-Tek) which were performed as previously described using growth-factor-reduced lrECM lots with protein concentrations between 9 and 11 mg/mL (Matrigel; BD Biosciences) (Debnath et al., 2003). After 48 h, the 3D cultures were fixed with 4% Paraformaldehyde in PBS. The 3D cultures were stained, as previously described by Debnath et al. (2003). Structures were stained with rat anti-human α6-integrin antibodies (Millipore clone NKI-GoH3MAB1378) for the primary and Alexa-568 conjugated goat antirat antibodies (Invitrogen) for the secondary. Alexa-647 conjugated phalloidin (Invitrogen) and 1× DAPI in PBS was used to stain the actin cytoskeleton and nuclei, respectively. Confocal images were acquired on Zeiss Axio Observer Z1 equipped with a Yokogawa spinning disk unit and an EM-CCD camera.

REFERENCES

1. Benkoski, J. J.; Höök, F. J. Phys. Chem. B 2005, 109, 9773

2. Yoshina-Ishii, C.; Boxer, S. G. J. Am. Chem. Soc. 2003, 125, 3696

3. Tumpane, J.; Ljungdahl, T.; Wilhelmsson, L. M.; Nordén, B.; Brown, T.; Albinsson, B. J. Am. Chem. Soc. 2009, 131, 2831

4. Kanasty, R.; Dorkin, J. R.; Vegas, A.; Anderson, D. Nat. Mater. 2013, 12, 967

5. Langecker, M.; Arnaut, V.; Martin, T. G.; List, J.; Renner, S.; Mayer, M.; Dietz, H.; Simmel, F. C. Science 2012, 338, 932

6. Gartner, Z. J.; Bertozzi, C. R. Proc. Natl. Acad. Sci. U.S.A. 2009, 106, 4606

7. Liu, J. S.; Gartner, Z. J. Trends Cell Biol. 2012, 22, 683

8. Chandra, R. A.; Douglas, E. S.; Mathies, R. A.; Bertozzi, C. R.; Francis, M. B. Angew. Chem., Int. Ed. 2006, 45, 896

9. Hsiao, S. C.; Shum, B. J.; Onoe, H.; Douglas, E. S.; Gartner, Z. J.; Mathies, R. A.; Bertozzi, C. R.; Francis, M. B. Langmuir 2009, 25, 6985

10. Selden, N. S.; Todhunter, M. E.; Jee, N. Y.; Liu, J. S.; Broaders, K. E.; Gartner, Z. J. J. Am. Chem. Soc. 2012, 134, 765

11. Pfaar, O.; Cazan, D.; Klimek, L.; Larenas-Linnemann, D.; Calderon, M. A. Curr. Opin. Allergy Clin. Immunol. 2012, 12, 648

12. Ishii, K.; Akira, S. Trends Immunol. 2006, 27, 525

13. Borisenko, G. G.; Zaitseva, M. A.; Chuvilin, A. N.; Pozmogova, G. E. Nucleic Acids Res. 2008, 37, e28

14. Liu, H.; Kwong, B.; Irvine, D. J. Angew. Chem., Int. Ed. 2011, 50, 7052

15. Palte, M. J.; Raines, R. T. J. Am. Chem. Soc. 2012, 134, 6218

16. Silvius, J. R.; Leventis, R. Biochemistry 1993, 32, 13318

17. Patwa, A.; Gissot, A.; Bestel, I.; Barthélémy, P. Chem. Soc. Rev. 2011, 40, 5844

18. Berti, D. Curr. Opin. Colloid Interface Sci. 2006, 11, 74

19. Pfeiffer, I.; Höök, F. J. Am. Chem. Soc. 2004, 126, 10224

20. Kato, K.; Itoh, C.; Yasukouchi, T.; Nagamune, T. Biotechnol. Prog. 2004, 20, 897

21. Debnath, J.; Muthuswamy, S. K.; Brugge, J. S. Methods 2003, 30, 256

22. Liu, J. S.; Farlow, J. T.; Paulson, A. K.; Labarge, M. A.; Gartner, Z. J. Cell Rep. 2012, 2, 1461

23. Goerke, S. M.; Plaha, J.; Hager, S.; Strassburg, S.; Torio-Padron, N.; Stark, G. B.; Finkenzeller, G. Tissue Eng., Part A 2012, 18, 2395

24. Saleh, F. A.; Whyte, M.; Genever, P. G. Eur. Cell Mater. 2011, 22, 242

25. Van Hoof, D.; Mendelsohn, A. D.; Seerke, R.; Desai, T. A.; German, M. S. Stem Cell Res. 2011, 6, 276

26. Glenn Research. 5'-MMT-Amino-Modifiers. Technical Note 1–2 (2013)

27. Debnath, J., Muthuswamy, S. K. & Brugge, J. S. Morphogenesis and oncogenesis of MCF-10A mammary epithelial acini grown in three- dimensional basement membrane cultures. Methods 30, 256–268 (2003).

FIGURES

Scheme 2-1. Stepwise Assembly of Fatty-Acid (FA)-Modified ssDNA into Cell Membranes.

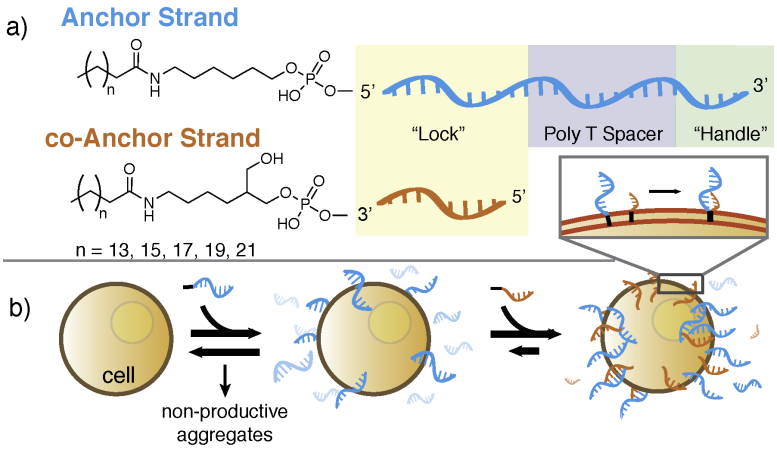

(a) Structure of the Anchor (Anch) and co-Anchor (cA) strands incorporating a lock region for Anch/cA-strand annealing and a polythymine spacer region. A handle region provides adhesion to surfaces and a means of quantifying cell membrane incorporation using complementary fluorescently labeled probes. (b) Model for step-wise assembly of membrane anchored DNA duplexes. FA-DNA molecules insert into the lipid bilayer but remain in rapid equilibrium with the surrounding cell medium. A second, complementary FA-modified oligonucleotide similarly establishes a rapid equilibrium with the cell membrane, but can also hybridize with the first strand in the membrane. The additional FA-anchor in the hybridized duplex alters the equilibrium, locking the co-anchored complex in the membrane. Elevated hydrophobicity can also trigger non-productive aggregate formation in solution.

Figure 2-1. Anchor (Anch) and complementary co-Anchor (cA) strands together enhance ssDNA targeting and retention in cell membranes.

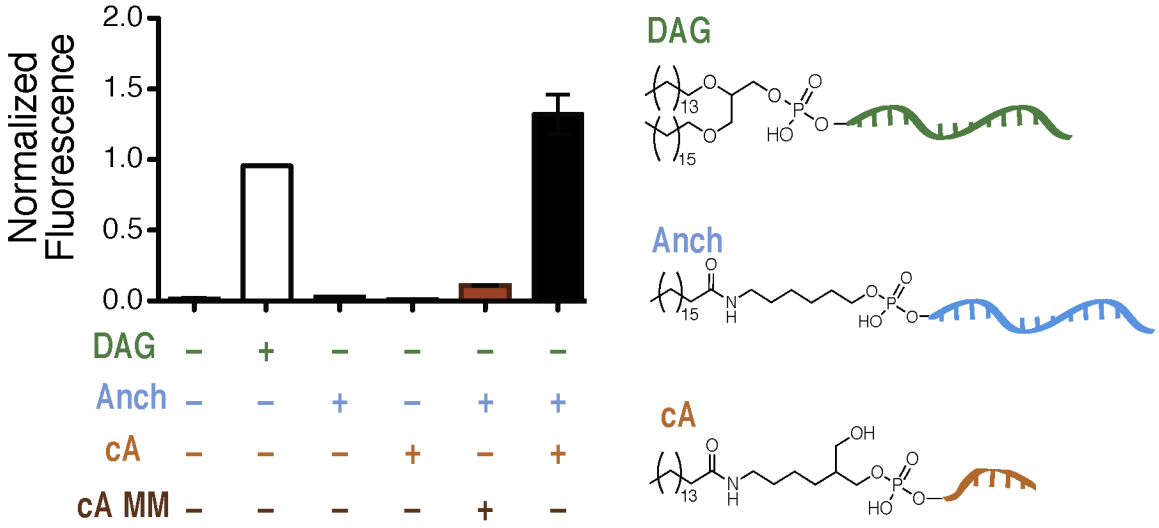

Fluorescence was measured with flow cytometry and normalized to a C_{16}/C_{18} DAG-ssDNA control. cA-MM is a 20 base coanchor strand with a DNA sequence noncomplementary to the Anch strand. Error bars are standard deviation of at least three independent replicates.

Figure 2-2. Lipid hydrophobicity affects cell labeling efficiency of Anch, cA, and prehybridized strands.

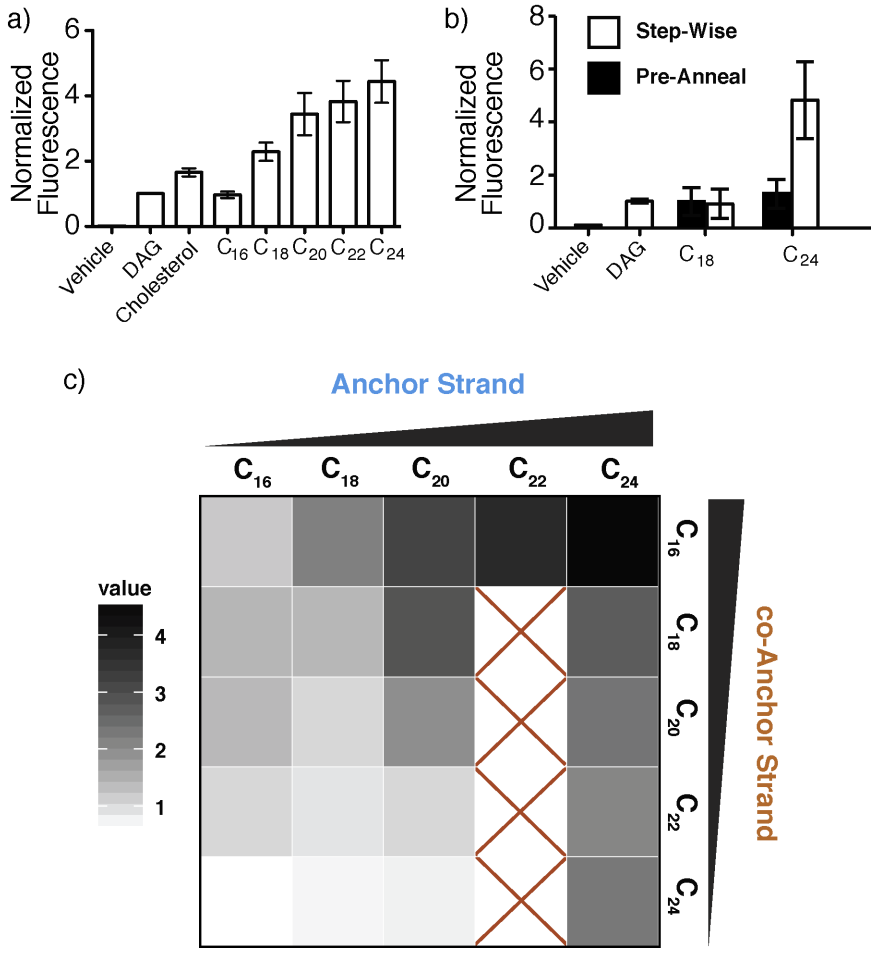

(a) Membrane incorporation compared to DAG for duplexes with 3′-cA_{20}-C16 strands and Anch strands bearing FA anchors of increasing length. (b) Membrane incorporation of 3′-cA_{20}-C16 and different Anch strands when added stepwise (white bars) or after preannealing (black bars). (c) Heatmap relating average membrane labeling (n = 3) to combinations of Anch and cA strand FA anchor lengths. Error bars are standard deviation of at least three independent measurements.

Figure 2-3. Ratio of FA to oligonucleotide length determines the extent of aggregation.

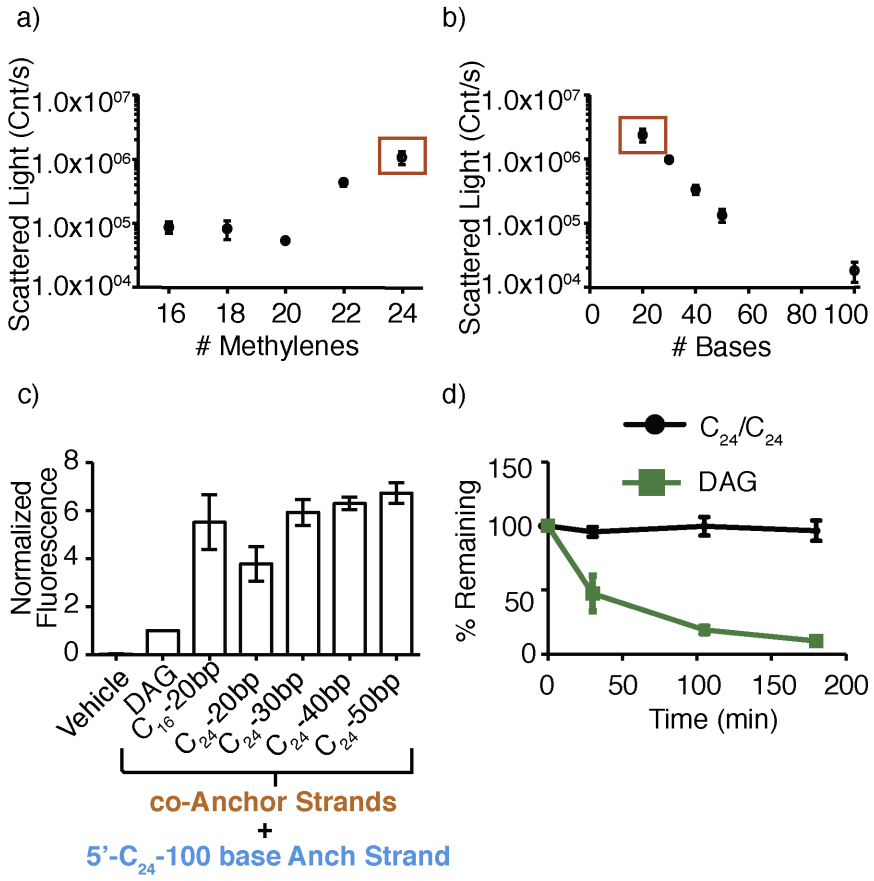

(a) Light scattering from solutions of 3′-cA$_{20}$ strands as a function of FA anchor length. (b) Light scattering from solutions of 3′-cA-C$_{24}$ anchored oligonucleotides as a function of the number of DNA bases. The red box indicates the same strand, 3′-cA$_{20}$-C$_{24}$. (c) Membrane incorporation compared to DAG for combinations of 3′-cA-C$_{24}$ with increasing numbers of DNA bases. (d) Incorporation vs time for DAG and 5′-Anch$_{100}$-C$_{24}$/3′-cA$_{50}$-C$_{24}$-DNA. Error bars are standard deviation of at least three independent measurements.

Figure 2-4. Improved preparation of single cell microarrays and 3D microtissues using stepwise assembly of membrane anchored adhesive oligonucleotides.

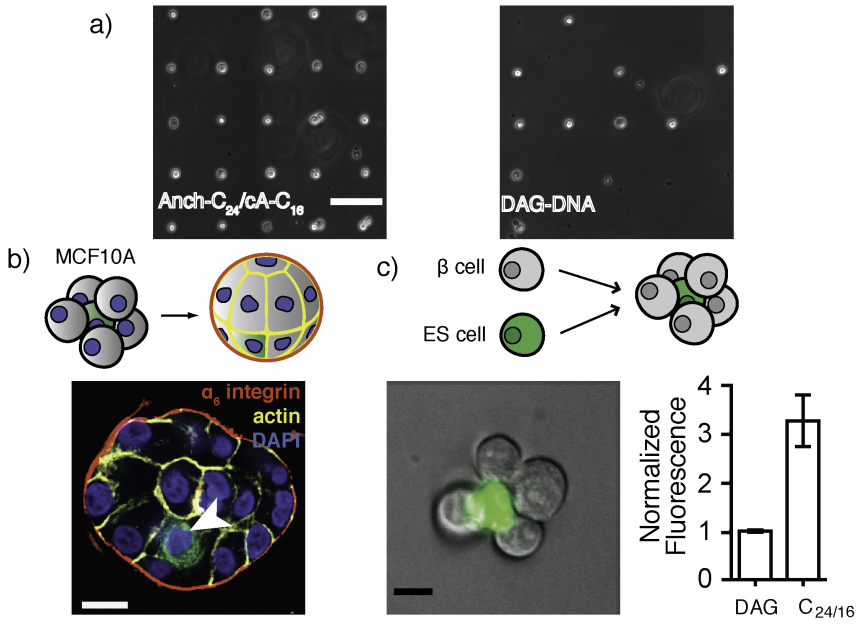

(a) Single cell microarrays prepared with murine ESCs labeled with $Anch_{100}$-C_{24}/cA_{20}-C_{16} or DAG. (b) MCF10A clusters assembled around 1 cell tracker green-stained cell (arrow) establish polarity after 48 h in Matrigel (scale bar is 20 μm). (c) Representative cluster of sorted ESC/β islet cells (scale bar is 10 μm) and labeling efficiency of β islet cells. Error bars are standard deviation of at least three independent measurements.

SUPPLEMENTARY INFORMATION

OLIGONUCLEOTIDE SEQUENCES:

Anchor Strands:

1) CAGT Repeat, 10 bp Duplex:

Y-5' Amino-AG CTG TCA $CT(T)_{70}$ CAG TCA GTC AGT CAG TCA GT 3'

2) CAGT Repeat, 15 bp Duplex:

Y-5' Amino-G ATC CAG CTG TCA $CT(T)_{65}$ CAG TCA GTC AGT CAG TCA GT 3'

3) CAGT Repeat, 20 bp Duplex:

Y-5'-Amino-GTA ACG ATC CAG CTG TCA $CT(T)_X$ CAG TCA GTC AGT CAG TCA GT 3'

4) ACTG Repeat, 20 bp Duplex:

Y-5'-Amino-GTA ACG ATC CAG CTG TCA $CT(T)_{60}$ ACT GAC TGA CTG ACT GAC TG 3'

5) CAGT Repeat, 20 bp Duplex:

5'-Cholesterol Phosphoramidite-GTA ACG ATC CAG CTG TCA $C(T)_{60}C$ AGT CAG TCA GTC AGT CAG T 3'

X=0, 20, 40, 60, or 80; Y= C16, C18, C20, C22, C24 saturated fatty acid

Co-Anchor Strands:

1) 10 bp Co-Anchor: 5' AGT GAC AGC T Amino 3'-Y Y=C16

2) 15 bp Co-Anchor: 5' AGT GAC AGC TGG ATC Amino 3'-Y
Y=C16

3) 20 bp Co-Anchor: 5' AGT GAC AGC TGG ATC GTT AC Amino 3'-Y
Y=C16, C18, C20, C22, C24 saturated fatty acid, Cholesterol

4) 30 bp Co-Anchor: 5' T10 AGT GAC AGC TGG ATC GTT AC Amino 3'-Y

5) 40 bp Co-Anchor: 5' T20 AGT GAC AGC TGG ATC GTT AC Amino 3'-Y

6) 50 bp Co-Anchor: 5' T30 AGT GAC AGC TGG ATC GTT AC Amino 3'-Y

Fluorescent Strands:

FAM-5'-(CAGT)5-3'

FAM-5'-(ACTG)5-3'

MALDI Mass Spectroscopy Data

The mass of representative co-anchor samples was confirmed by MALDI-MS using a Voyager-DE Pro in reflector mode with a hydroxypicolinic acid/ammonium citrate matrix supplemented with acetone solubilized nitrocellulose4. While the various anchor strands and co-anchor strands were tested for purity by analytical HPLC re-injection, only the masses of the co-anchor strands were confirmed by MALDI-MS due to the low mass resolution of MALDI for high molecular weight FA-oligonucleotides. Each measurement represents an individual spot on the MALDI plate.

Molecule	Actual MW	Measured (M+H)					Average	StDev
		1	2	3	4	5		
10mer 3' C16	3500	349	3499	3499	3498	3499	3499	0.4
15mer 3' C16	5065	5064	5064	5064	5064	5064	5064	0.0
20mer 3' C16	6605	6603	6607	6606	6599	6598	6603	4.0
20mer 3' C18	6633	6630	6629	6630	6630	6630	6630	0.6
20mer 3' C20	6661	6656	6657	6657	6657	6657	6657	0.4
20mer 3' C22	6689	6686	6685	6685	6685	6685	6685	0.4
20mer 3' C24	6717	6717	6715	6714	6714	6713	6715	1.2
20mer 3' Cholesterol	6913	6912	6912	6912	6913	6911	6912	0.7

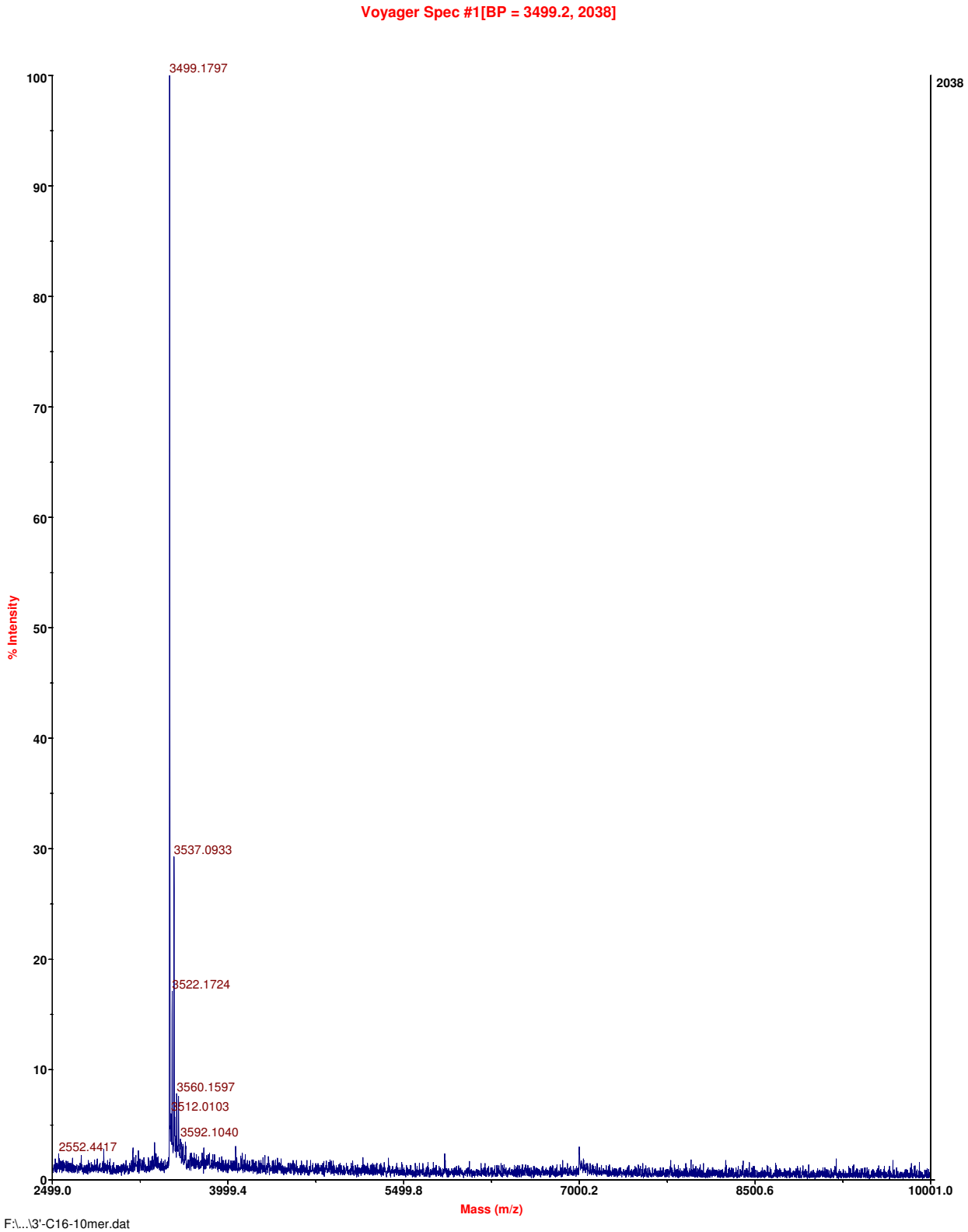
Voyager Spec #1[BP = 3499.2, 2038]
3499.1797
2038
100
90
80
70
60
50
40
30
20
10
0
% Intensity
3537.0933
3522.1724
3560.1597
3512.0103
3592.1040
2552.4417
2499.0
3999.4
5499.8
7000.2
8500.6
10001.0
Mass (m/z)
F:\...\3'-C16-10mer.dat
Acquired:

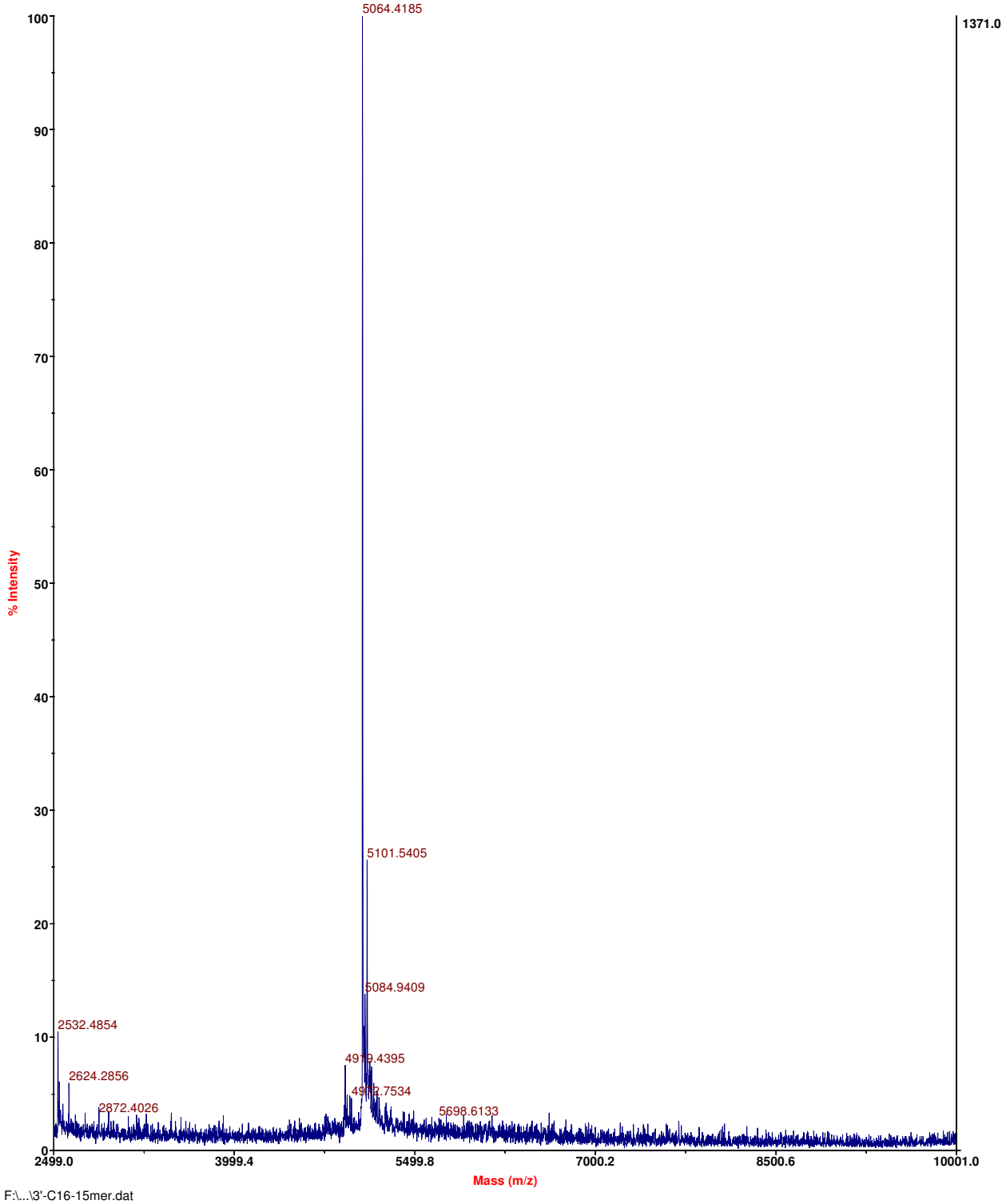

F:\...\3'-C16-15mer.dat
Acquired:

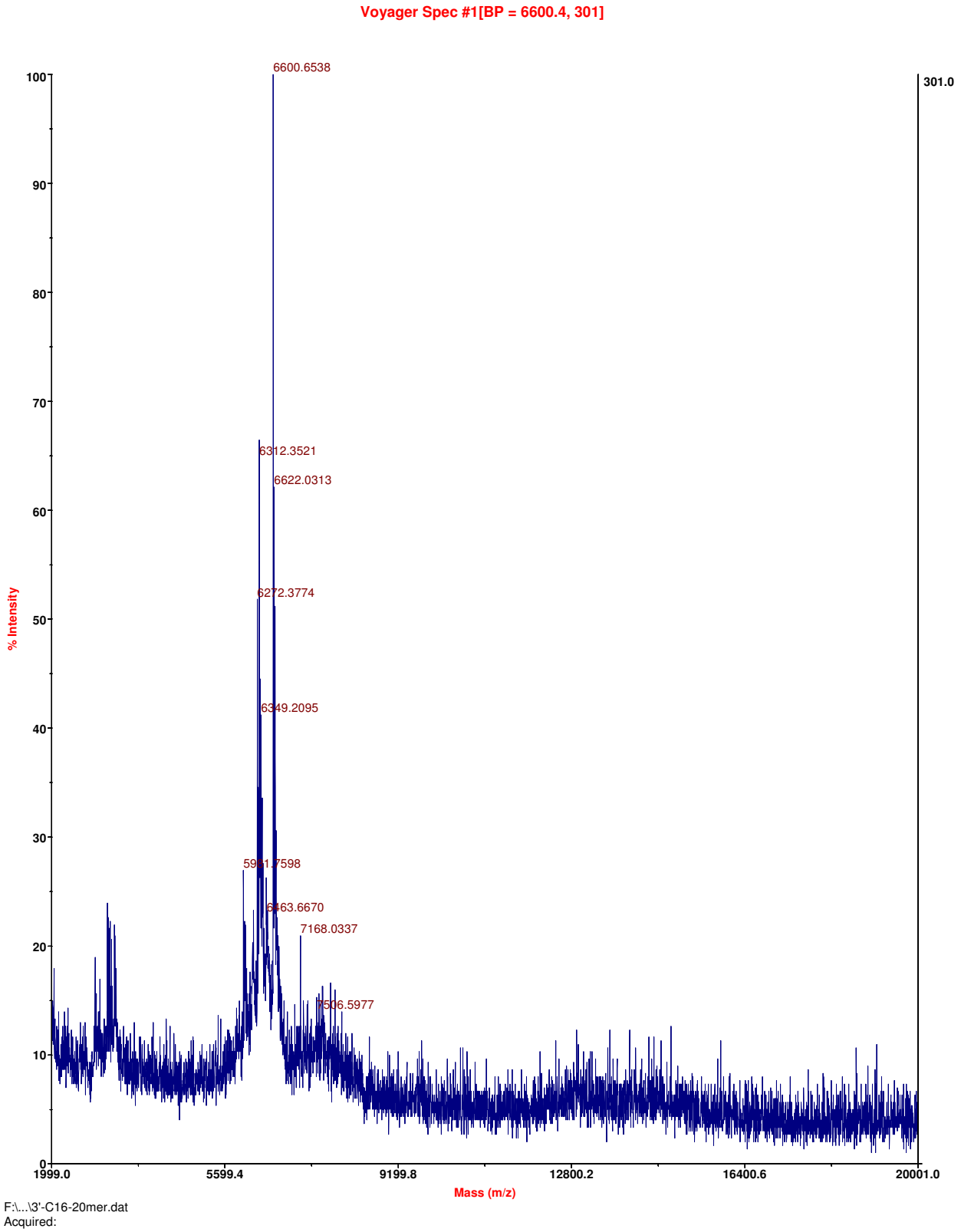
Voyager Spec #1[BP = 6600.4, 301]
6600.6538
301.0
6312.3521
6622.0313
6272.3774
6349.2095
5951.7598
6463.6670
7168.0337
7506.5977
% Intensity
Mass (m/z)
1999.0
5599.4
9199.8
12800.2
16400.6
20001.0
F:\...\3'-C16-20mer.dat
Acquired:

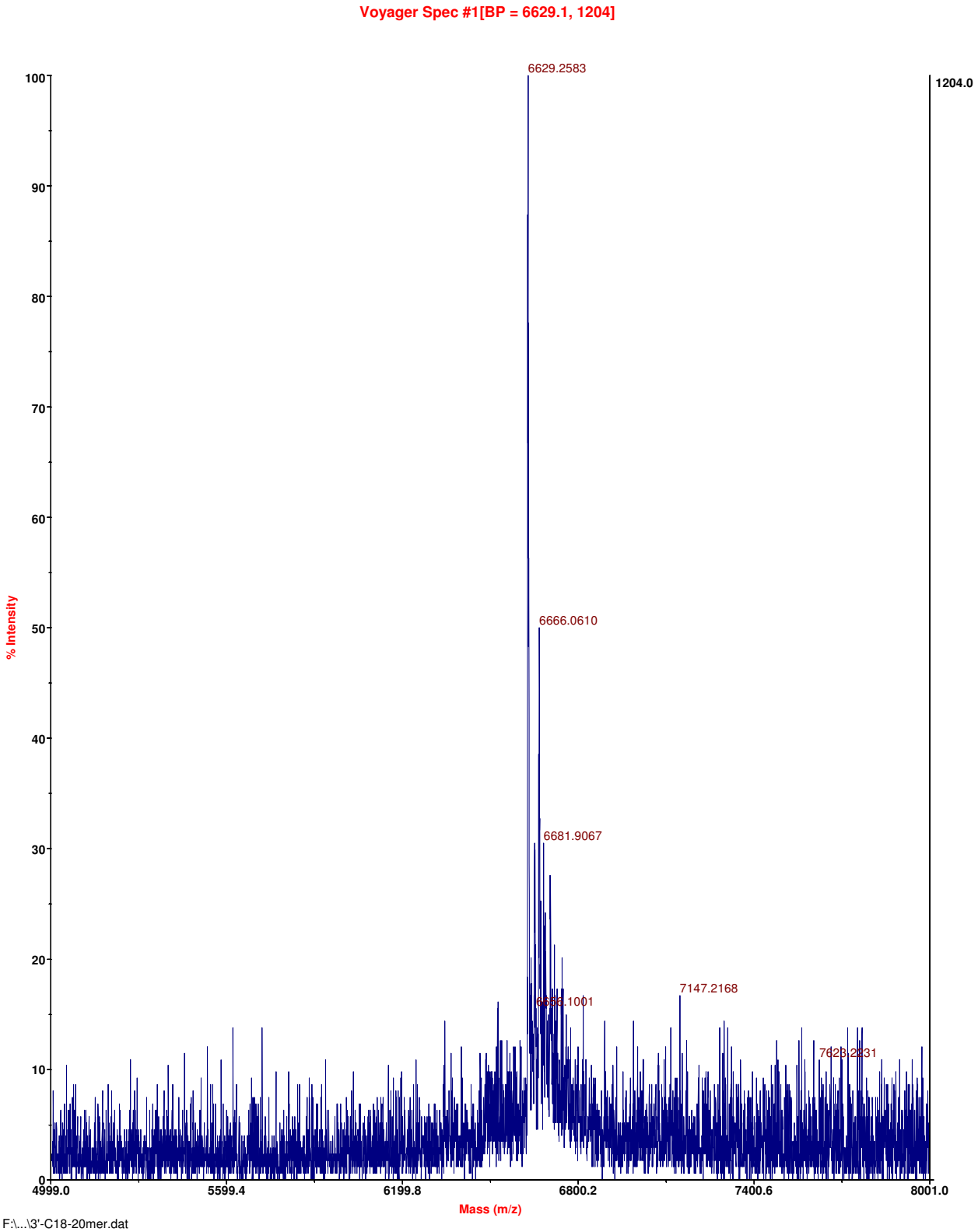

F:\...\3'-C18-20mer.dat
Acquired:

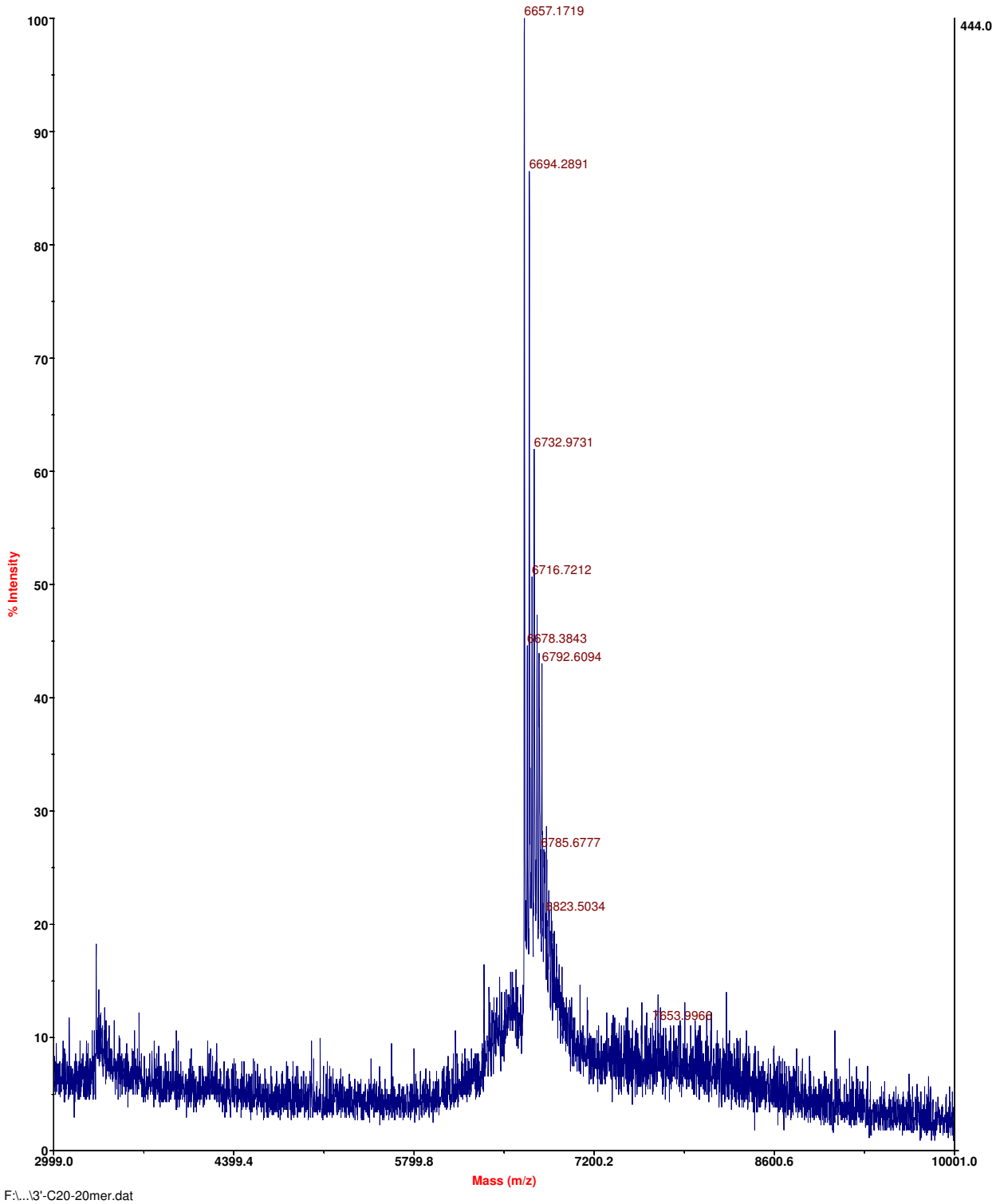

F:\...\3'-C20-20mer.dat
Acquired:

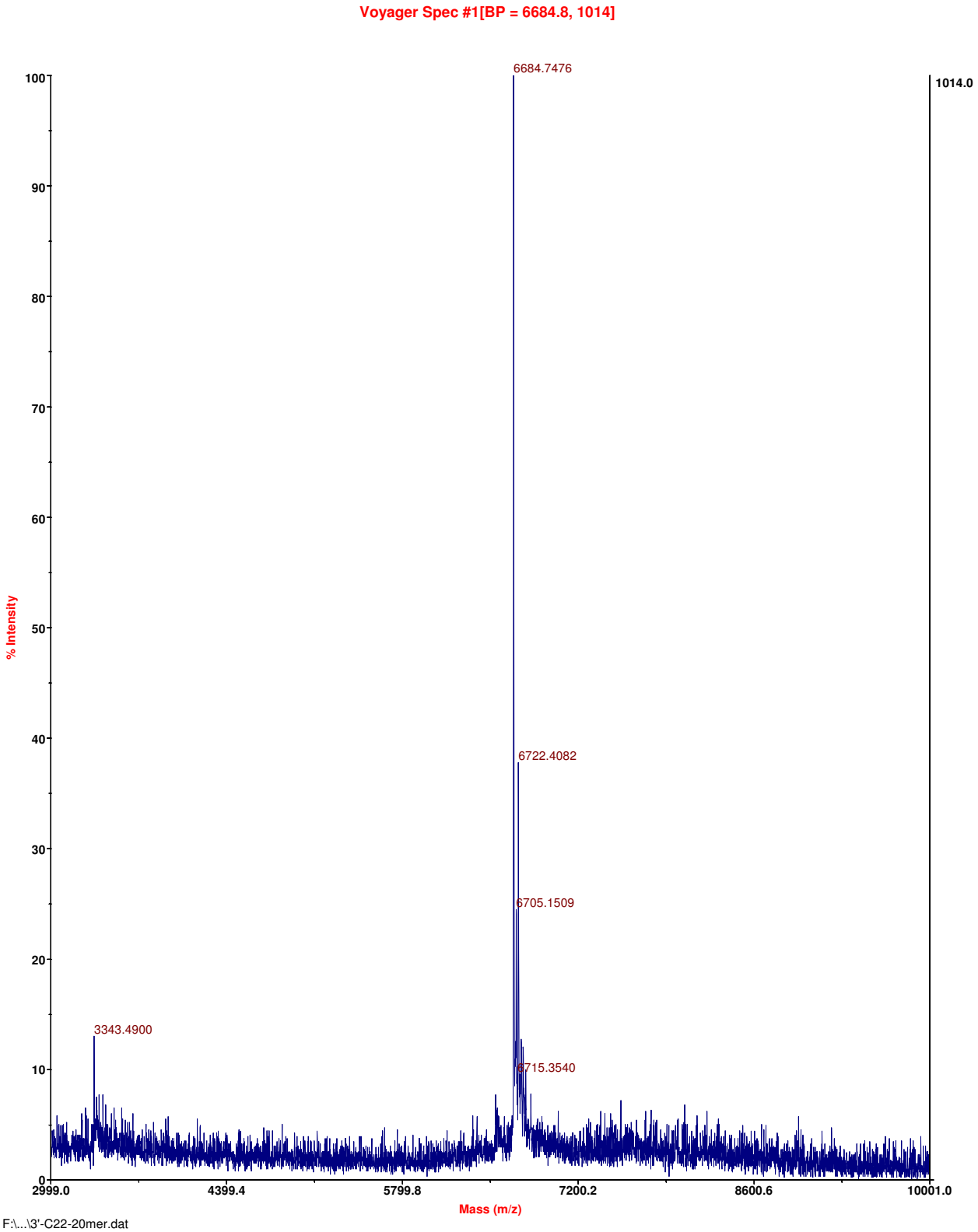

F:\...\3'-C22-20mer.dat
Acquired:

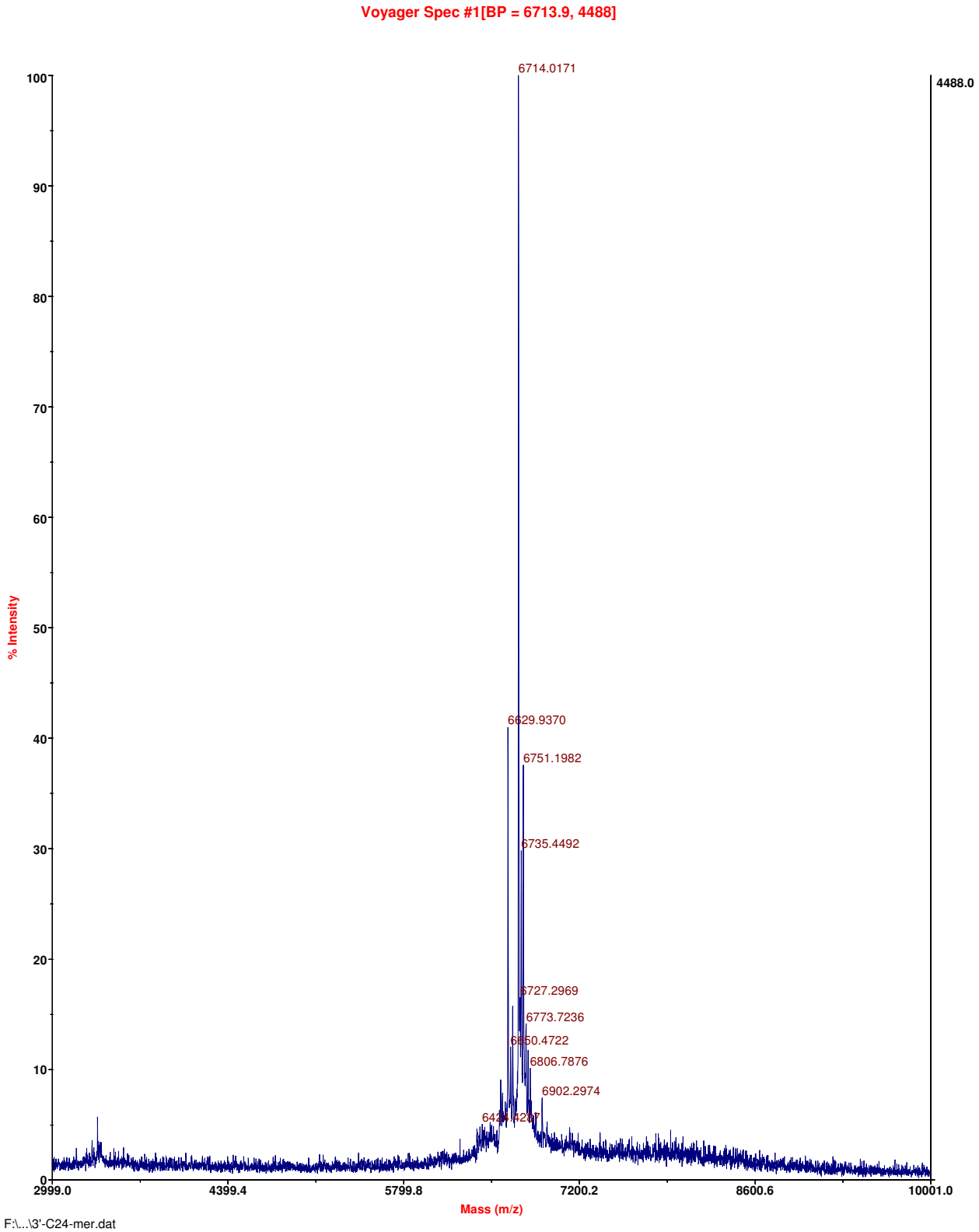

F:\...\3'-C24-mer.dat
Acquired:

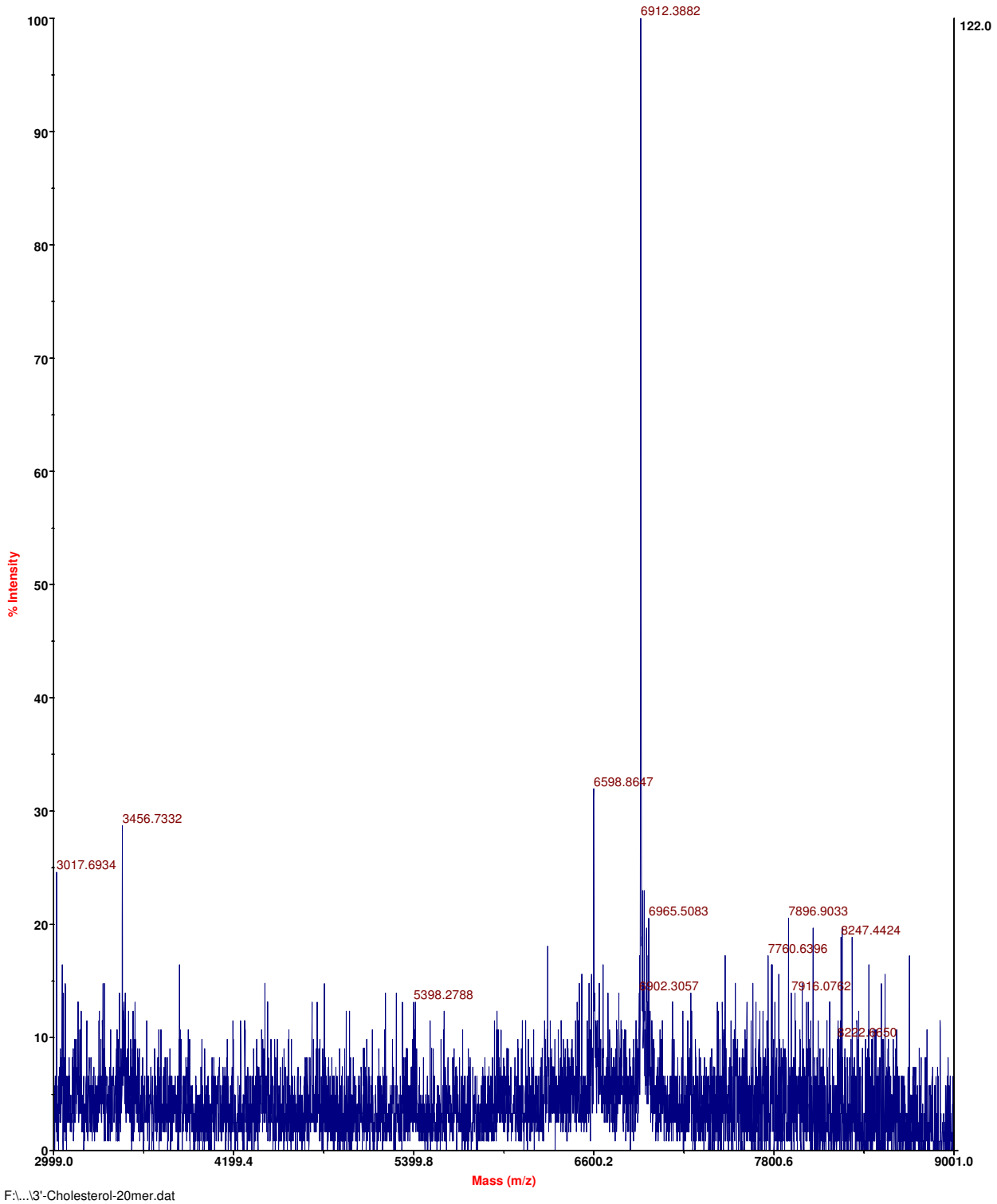

F:\...\3'-Cholesterol-20mer.dat
Acquired:

Figure 2-S1. Labeling of Jurkats with single and double cholesterol anchors.

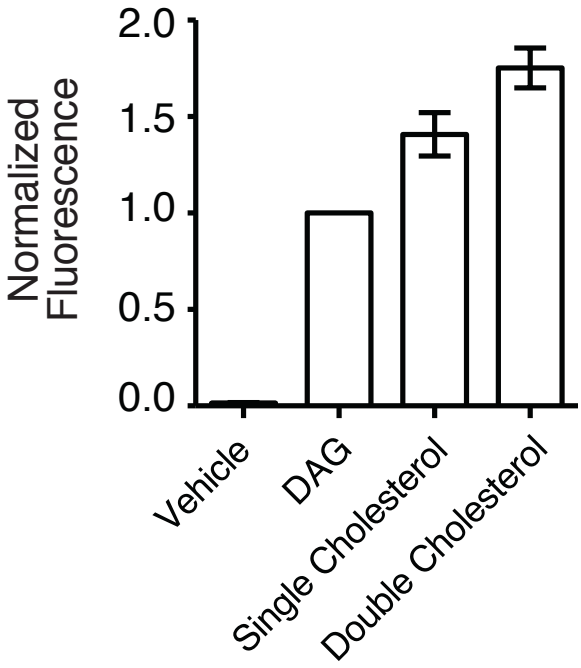

Single cholesterol indicates cells a single anchor strand linked to cholesterol (Anch-Chol) alone. Double cholesterol indicates cells labeled with Anch-Chol and a co-anchor modified with cholesterol (cA-Chol) with a 20 bp duplex. Fluorescence was normalized to DAG. Error bars are standard deviations of at least 3 independent measurements.

Figure 2-S2. Cell labeling Optimization.

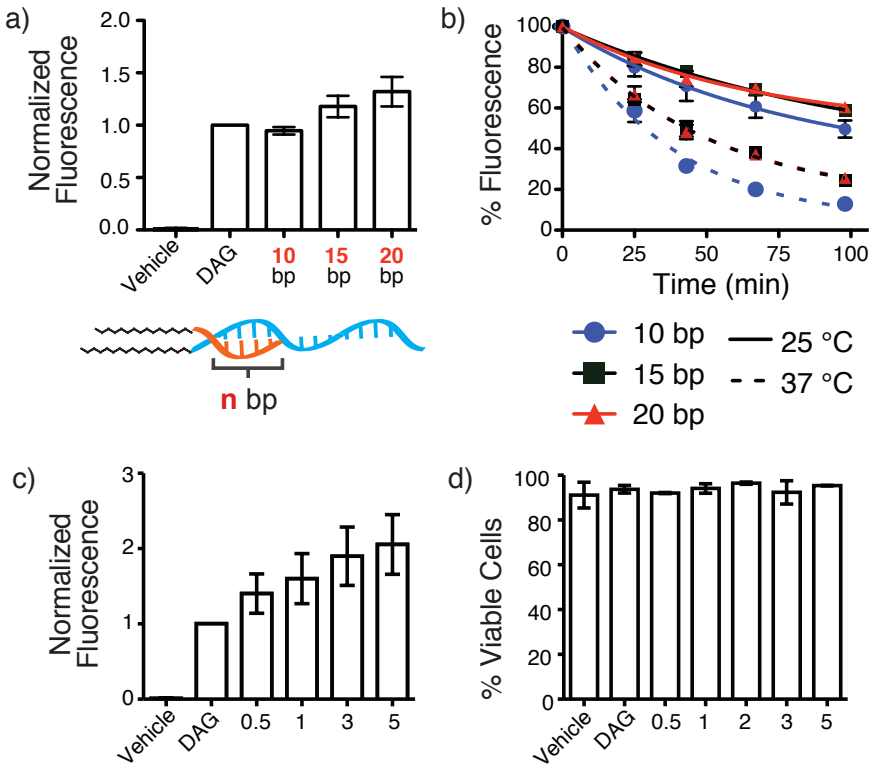

The combination of FAs used for this experiment was 5'-Anch100-C18 and 3'-cA-C16. a) Dependence of initial cell labeling on the length of duplex formed by the anchor and co-anchor. b) Stability of cell labeling overtime at 25 and 37 °C as a function of duplex length. c) Initial cell labeling as a function of FA-DNA concentration. d) Effect of FA-DNA concentration on cell viability. Error bars are standard deviations of at least 3 independent measurements.

Figure 2-S3. Binding of cells bearing Anch and cA ssDNA duplexes to cells and surfaces bearing complementary oligonucleotide sequences.

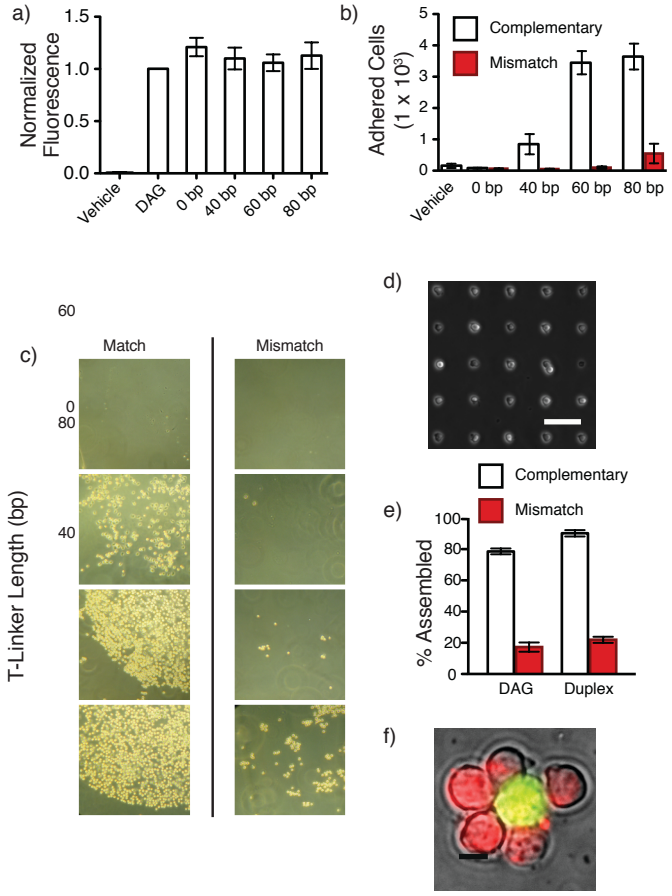

a) Labeling efficiency of various poly-T linker lengths on the anch strand. b,c) Model cell line, Jurkats, labeled with DNA complexes bearing poly-T linker lengths of increasing length were incubated with aldehyde glass modified with spots of complementary or non-complementary ssDNA (scale bar = 100 μm) and the number of adhered cells was quantified. d) An array of Jurkat cells prepared from printed DNA spots approximately 1 cell in diameter (scale bar is 100 μm). e) Assembly of Jurkats into small clusters when labeled with complementary and non-complementary DNA strands. f) Representative image of one such cluster. Error bars are standard deviations of at least 3 independent measurements.

Figure 2-S4. The effect of FA-Anch length on cell surface DNA retention after 90 minutes at 37 °C.

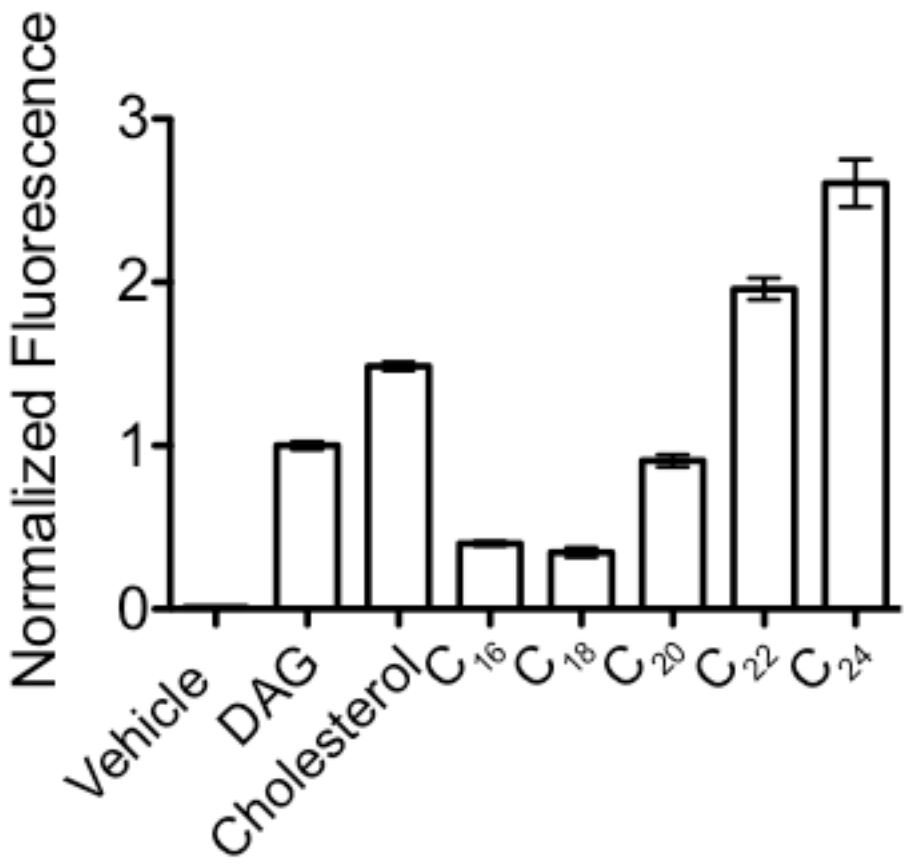

The Anch strand was linked to saturated fatty acids of increasing length and fluorescence was measured after a 90 minute time course and normalized to DAG which was arbitrarily set to 1. The cA strand was linked to 3'-cA20-C16 fatty acid for all samples. Error bars are standard deviations of at least 3 independent measurements.

Figure 2-S5. Particle size by DLS of 3'-cA strands of with various hydrophobicities and charges.

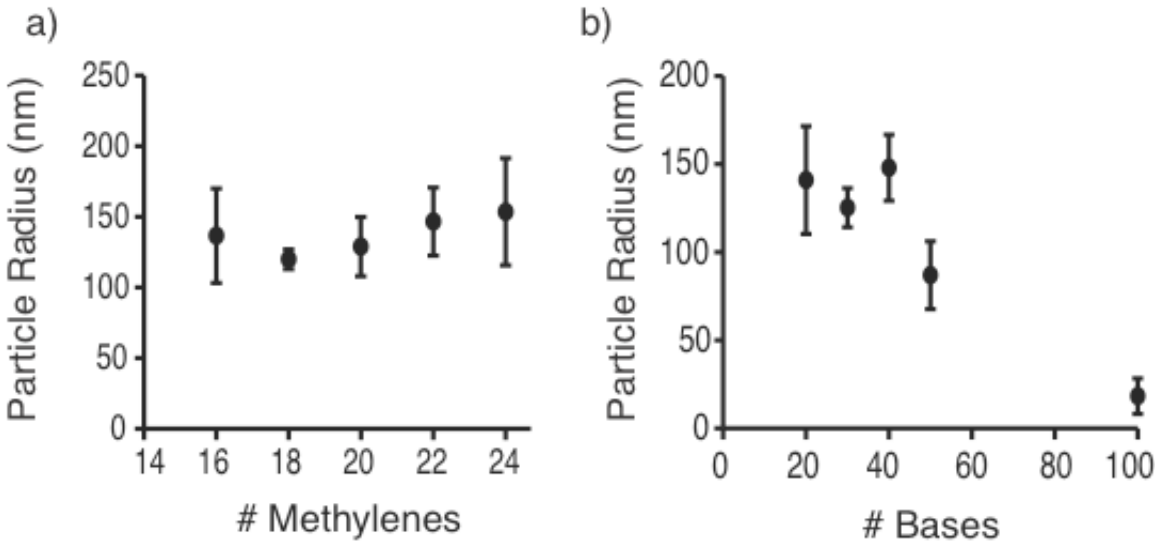

a) Particle size gradually increases as the hydrophobicity of the linked fatty acid increases for 3'-cA20. Particle size drops for 3'-cA-C24 as more nucleotides are added thus increasing the charge. Error bars are standard deviations of at least 3 independent measurements.

Figure 2-S6. Cell Labeling of Several Primary Cell Lines.

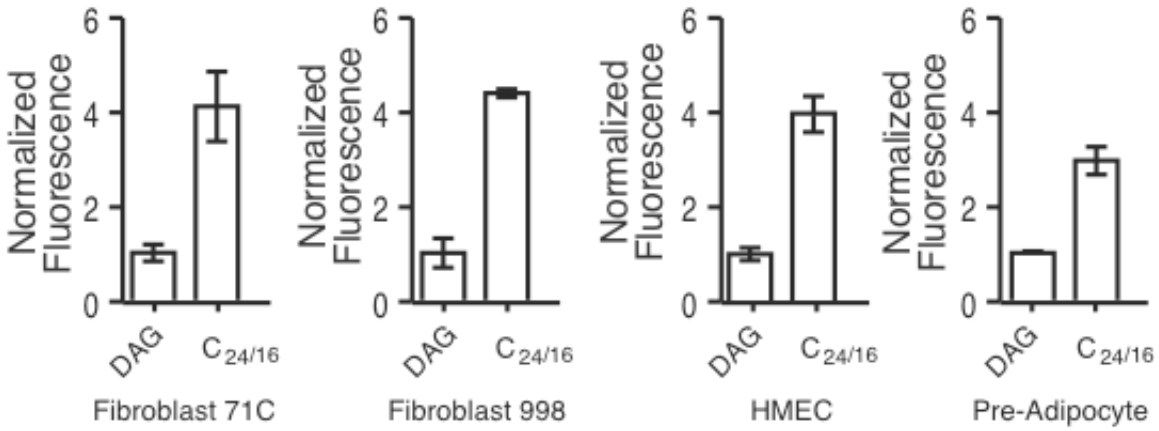

Cells were labeled with either DAG or a combination of 5'-Anch100-C24/3'-cA50-C24 and the relative fluorescence was plotted. Error bars are standard deviations of at least 3 independent measurements.

CHAPTER 3

RAPID ORGANOID RECONSTITUTION BY CHEMICAL MICROMOLDING

Source: Rapid Organoid Reconstitution by Chemical Micromolding

Robert J. Weber, Alec E. Cerchiari, Lucas S. Delannoy, James C. Garbe, Mark A. LaBarge, Tejal A. Desai, and Zev J. Gartner

ACS Biomaterials Science & Engineering ***2016 2*** *(11), 1851-1855*

DOI: 10.1021/acsbiomaterials.6b00421.

Contributions: Alec Cerchiari and I initiated the project and performed the majority of the experiments with equal contributions. Photolithography work was initiated by Alec Cerchiari and completed with assistance from Jennifer Hu and Katelyn Cabral. Zev Gartner, Alec Cerchiari, Tejal Desai and I wrote the manuscript with editorial input from all authors. Zev Gartner and Tejal Desai supervised the project.

INTRODUCTION

The ability to reconstitute human cells into organoids—or small 3D consortia of cells that recapitulate the basic architecture of their parental tissue—promises to enhance our ability to screen drugs, model diseases, and regenerate organs.(1-6) Organoids are also emerging as invaluable tools for dissecting development, morphogenesis, human pathology, and even for probing components of the stem cell niche.(7-10) Currently, many technologies exist to create organoids. Some approaches begin from single stem cells,(11, 12) whereas many others use printing or aggregation techniques to place cells into rudimentary aggregates for subsequent culture.(13-15)

Across multiple tissue types, cells retain powerful programs of self-organization ex vivo that drive the formation of tissue architecture, (16-19) and these programs are required to guide the self-organization of aggregated cells into mature and physiologically relevant structures. Efficient self-organization depends upon appropriate microenvironmental cues, especially approximate positioning of different cell types and extracellular matrix (ECM) components.(20, 21) These cues are often ill-defined and tissue specific. Therefore, high-throughput means of reconstituting cell aggregates with defined structures offers the potential to facilitate the development and elaboration of organoid models by simplifying the synthesis of aggregates with more controlled initial geometries and culture conditions.(22-24) An ideal approach would be rapid, scalable, and agnostic to cell or tissue type.

A powerful and widely adopted strategy for reconstituting cells into microtissues involves packing cells into arrays of photolithographically formed microwells of defined size and shape by sedimentation or injection.(4, 25-29) The arrays are generally fabricated from elastomers such as polydimethylsiloxane (PDMS) or minimally adhesive hydrogels such as polyethylene glycol (PEG), polyacrylamide (PA), or agarose. Hydrogels can also be functionalized with oligopeptides or ECM proteins but rarely sustain in vivo-like patterns of self-organization and are generally not suitable for prolonged 3D culture. Variations of this general approach have been used to mold microtissues directly within hydrogel ECM mimics such as Matrigel, collagen, or fibrin.(30, 31) However, a major limitation for all of these approaches is that the optimum viscoelastic and chemical properties of a particular hydrogel for casting microwells are often at odds with optimum properties for subsequent 3D culture. For example, materials such as polyacrylamide are in a stiffness regime that can cause actin polarization and perturb growth and morphogenesis.(32, 33) In contrast, matrigel has a low modulus (34) and allows for growth and morphogenesis (35, 36) but is too soft to reliably be molded into microwells. Thus, these strategies are compatible with only a subset of hydrogels, or a subset of cell and tissue types. Additionally, these strategies do not provide means for the control of internal aggregate topology, and technical challenges related to surface chemistry (e.g., passivation of molds used for templating) or ease of use (e.g., cell-processing time and quality of reconstituted 3D pattern) hinder the wide adoption of these methods.

One potential solution to these limitations involves casting cells into microwells, and upon formation of a cohesive aggregate, transferring the aggregates out of the microwells and into appropriate conditions for long-term culture. However, even cohesive cells have slow adhesion kinetics from dissociated and trypsinized populations, requiring relatively long incubations in microwells prior to transfer, affecting viability, cellular differentiation, and organoid uniformity. Furthermore, cell aggregates formed in microwells compact and reorganize over time preventing the culture of microtissues with defined internal structures or shapes other than spheroids (Figure 3-S1).

RESULTS AND DISCUSSION

To overcome these temporal obstacles, we envisioned catalyzing cell-to-cell adhesion by transiently chemically remodeling the exterior of cells with mutually adhesive synthetic single stranded oligonucleotides (ssDNA) prior to centrifugation into microwells–an approach we've termed "Chemical Micromolding." DNA programmed adhesion allows rapid and reversible cell adhesions within the microwells, facilitating rapid transfer to appropriate 3D culture conditions without disruption of aggregate shape enforced by microwell geometry (Figure 3-1A–E). There are several ways to modify cell surfaces with ssDNA (37-40), but we found previously described coanchored, fatty acid-modified oligo pairs (A and A′) to be the simplest and most efficient approach across multiple cell types (41).

To test the feasibility of Chemical Micromolding, we began by preparing two populations of Jurkat cells, a non-adhesive human lymphoma cell line, bearing either of two complementary ssDNA strands on their cell surfaces. Using repetitive DNA sequences, we observed significant amounts of cell aggregation outside of microwells prior to centrifuging, negatively affecting the yield of targeted structures (Figure 3-S2). We hypothesized the aggregation was due to rapid DNA annealing in solution, above the microwells, prior to and during centrifugation. We therefore redesigned the ssDNA strands to incorporate more heterogeneous adhesive sequences which have been shown to slow the kinetics, but not stability, of cell–cell adhesion (37). These new sequences (R and R′) reduced adhesion outside the confines of microwells, but still provided for strong cell–cell adhesion within the microwells (Figure 3-S2). Moreover, cell-aggregates could be subsequently transferred to biomimetic hydrogels for 3D culture where they were initially observed to maintain the architecture prescribed by the microwell geometry (Figure 3-1E). The entire process, including cell labeling, centrifugation, micromolding, and transfer to hydrogel, required less than 2 h to complete.

DNA-labeled cells retain a surface boundary coated with excess, unpaired ssDNA molecules even after aggregation. Residual DNA poses a challenge to manipulation of these “sticky” cell-based biomaterials, as it can catalyze hierarchical assembly of molded aggregates into higher order structures once transferred out of the microwells. Formation of higher-order aggregates, although potentially useful, severely decreases the yield and uniformity of microtissues

transferred to 3D culture. We therefore explored the use of DNA capping strands as a protecting group, preventing additional adhesion between aggregates. We prepared a spectrum of capping strands (Table 3-S1), varying the lengths, and used flow cytometry to explore their ability to kinetically block additional annealing without disrupting existing adhesions by strand invasion (Figure 3-2A) (42, 43). Shorter capping strands of 22 bases and fewer were ineffective at blocking subsequent binding events. However, longer capping strands spanning the entire annealing region (30 bases) effectively blocked subsequent binding events without disrupting existing cell-to-cell bonds (Figure 3-2B, C). Therefore, we used the 30 base capping strand in subsequent experiments in order to retain aggregate structures after transfer out of microwells.

Chemical micromolding allowed for the formation and transfer of microtissues with different sizes and shapes to very soft hydrogels such as Matrigel for subsequent culture (Figure 3-2D). We prepared cylindrical structures as well as cubes, triangular prisms, and others. Notably, we were also able to transfer rectangular-shaped microtissues and *y*-shaped microtissues as simple facsimiles of tubular or branched structures, respectively. Thus, compared to other approaches, chemical micromolding can form microtissues of increased geometrical complexity and variable aspect ratio in soft gels. Furthermore, the approach is easily scalable by using more microwell arrays in parallel or simply creating larger arrays (Figure 3-S3).

Aggregates formed by Chemical Micromolding can be elaborated through additional manipulations by leveraging the fact that cells can be labeled with

multiple and orthogonal strands of ssDNA. To demonstrate this concept we began by double labeling two populations of cells with one set of ssDNA strands complementary to each other and another ssDNA complementary to a third cell type (Figure 3-3A). We found incorporation of a second ssDNA strand to the cell surface reduced the relative incorporation of each individual ssDNA but total DNA incorporation remained sufficient for DNA-programmed assembly (37) (Figure 3-S4).

The first two cell populations of Jurkats (red and unstained) were each labeled with two different strands of ssDNA, one complementary to each other, and one complementary to a third cell population. They were then centrifuged into circular microwells as outlined above to create a spherical core that was liberated from microwells in the presence of capping strand and a third cell type (green) labeled with a ssDNA strand complementary to both the red and unstained population to create a core–shell structure (Figure 3-3B). This conformal structural motif is found in a number of tissues including the mammary, prostate, salivary, sweat, and lacrimal glands. We therefore repeated the process but using the two cell lineages found in the human mammary gland. We used primary Human Mammary Epithelial Cells (HMECs) (Figure 3-3C), forming a core of luminal epithelial cells (LEPs) and an outer layer of myoepithelial cells (MEPs). The resulting microtissues had the basic 3D structure of the mammary gland and could be transferred to Matrigel or agarose for culture. We found that in the epithelial microenvironment provided by matrigel, the organization persisted (Figure 3-3D and 3-3E) while in agarose the cells rearranged themselves into a

disorganized structure even after 1 day, consistent with the inappropriate microenvironmental cues provided by agarose (14). Furthermore, the capacity of these tissues to demonstrate lumenization in Matrigel (Figure 3-3E, arrow) indicates that the process of DNA-labeling and chemical micromolding does not interfere with their intrinsic potential to self-organize.

CONCLUSION

In summary, chemical micromolding is a powerful new approach to rapidly reconstitute organoids of defined size, shape, and internal structure using DNA programmed adhesion to catalyze tissue aggregation, and microwells to enforce aggregate geometry. We have previously shown that DNA labeling has negligible effects on cell viability (41) and presume that the shortened processing time necessary for completing chemical micromolding compared to similar approaches (44) will further enhance cell viability. This technique is scalable by preparing more or larger microwell arrays. Tissue assemblies of greater complexity can be synthesized by iteratively adding layers of cells. We anticipate that chemical micromolding will find utility in preparing uniform microtissues for high-throughput, multicellular assays and in allowing for the study of tissues that incorporate sensitive, nonadhesive, or weakly adhesive cells.

METHODS

SYNTHESIS OF FATTY ACID-MODIFIED OLIGONUCLEOTIDES AND LABELING CELLS WITH SINGLE STRANDED DNA

The procedure used to synthesize fatty acid-modified oligonucleotides and label cells was already described in the methods section of the preceeding chapter. In brief, oligonucleotide strands were synthesized on an Expedite 8909 DNA synthesizer using reagents and protocols standard to the instrument. A terminal amine was incorporated either via modified phosphoramidite for the 5' amine (Glen Research 10-1906-90) or by utilizing a modified solid support for the 3' amine (Glen Research 20-2958). DNA was elaborated with the fatty acid membrane anchors lignoceric acid and palmitic acid for the adhesion and co-anchor strands respectively by condensation using carbodiimides. Fatty acid-modified strands of 20 bases for co-anchor and 100 bases for adhesion strands were purified from residual, unmodified oligonucleotides by reverse phase chromatography on an Agilent 1200 Series HPLC System using 100 mM triethylamine acetate (TEAA, pH 7) H_2O/acetonitrile as a mobile phase on a C8 column (Hypersil Gold, Thermo scientific) running a gradient between 8 and 95% acetonitrile over 30 minutes. Strands were checked for approximate mass on a Shimadzu Axima Performance MALDI-TOF instrument. Concentrations of purified products were determined by UV absorbance at 260 nm using a Thermo-Fischer NanoDrop. Cells were labeled by a 5-minute incubation in a 1 μM concentration of first the 'Adhesion' strand at room temperature followed by a 5-minute incubation with 1 μM of the 'Co-Anchor' strand at room temperature. Residual DNA strands were removed by washing the cells three times via pelleting and resuspension in calcium and magnesium free phosphate-buffered saline (PBS-CMF) (UCSF Cell Culture Facility).

Cell Lines and Primary Cells

Jurkat cells (Clone E6-1) ATCC TIB-152 were obtained from the ATCC and were grown in suspension using RPMI 1640 supplemented with 10% fetal bovine serum (v/v) (UCSF Cell Culture Facility). MCF10As were obtained from the lab of Professor Jayanta Debnath (UCSF) and were cultured as previously described[2]. HMEC cultures were provided by Dr. Martha Stampfer (LBNL) and cultured in M87 media supplemented with cholera toxin as previously described[3]. The specific specimen used in this study was 240L, which was obtained from the reduction mammoplasty of a 19 year old woman.

Fabrication of PDMS Stamps

PDMS stamps were produced from a photolithographically created master mold. SU-8 2075 (Microchem) was spun onto a silicon wafer to a thickness of approximately 100 µm. The wafer was briefly baked for 10 minutes on a hotplate set to 135 °C. The prebaked SU-8 was patterned with a negative mask (CAD/Art Services, Inc.) for 5 minutes. The wafer was subsequently baked for 1 minute on the hotplate set to 135 °C and then developed with agitation in 1-Methoxy-2-propyl acetate SU-8 developer (Microchem) for 15 minutes. Both sides of the wafer were washed with fresh 1-Methoxy-2-propyl acetate to remove dissolved resist followed by washing with isopropyl alcohol. The wafer was subsequently baked on the hotplate for another 10 minutes, allowed to cool and placed with features face up into a 150 mm petri dish. 30 grams of polydimethylsiloxane

(PDMS) elastomer (Sylgard® 184 Silicone Elastomer Kit, Dow Corning) was mixed with 3 grams of curing agent (10:1 ratio w/w) in a large weigh boat, mixed rapidly with a spatula until bubbles were apparent and poured into the petri dish containing the wafer, coating it evenly. The petri dish with PDMS was then degassed until bubbles were no longer apparent, approximately 30 minutes. The PDMS was then baked for at least 3 hours at 60 °C. The PDMS was removed from the master by cutting with a disposable scalpel or razor blade. Stamps were created to fit a 24 well or 6 well dish by manually subdividing the PDMS elastomer with a razorblade.

Fabrication of Microwell Arrays

Microwell arrays were created by pipetting 400-500 µL of molten agarose (Allstar Scientific, 490-050, Lot BB01013R0S) (3% w/v) or gelatin (8% w/v) (Knox Original Gelatin, unflavored) into each well of a 24 well plate and gently placing a PDMS stamp face down into the liquid in a manner so that the stamp features are in contact with the liquid, but not pressed down into the bottom of the well. For different sizes of stamps or vessels, the volume of agarose or gelatin scales with the surface area of the vessel. For example, 2 mL were used for a sample in a 6 well cell culture plate. The plate is then incubated at 4 °C until the agarose or gelatin solidifies which is apparent because it changes from translucent to opaque in appearance. The PDMS stamps are then gently removed by forceps and 500 µL of PBS-CMF (UCSF cell culture facility) is added. In general, PDMS

stamps were removed shortly before the microwells were used in order to avoid deformations that occur over time, particularly in the case of gelatin microwells.

Procedure for Chemical Micromolding

Cells are divided into two populations and stained with Cell Tracker Green CMFDA or Cell Tracker Red CMPTX (Thermofisher) as per manufacturers instructions. The two populations were labeled separately with complementary ssDNA strands as described above. Cells are mixed in a 1:1 ratio in a tube at a concentration of 1 million cells per mL, added to the microwell array and placed promptly into a centrifuge. For microwells in a 24 well plate, we found 1 million Jurkats (500,000 of population 1 and 500,000 of population 2) filled the microwells with high occupancy, though this may need to be adjusted for cells of different sizes. Centrifugation speed was set to the slowest velocity at which a cell pellet was observed. For cells used in this study, we found 160xg for 4 minutes was sufficient. Typically this results in many full wells but also excess cells collecting around the edges of the microwell array. These excess cells are adhesive to each other as large aggregates visible by eye and easily removed by gently washing the edges of the array with PBS-CMF and 1 mL pipetteman. Cells were allowed to anneal in the microarray for 10 minutes and then incubated with 1 μM capping strand for 10 minutes. Microtissues were recovered from agarose microwell arrays by gentle agitation with a 1 mL pipetteman with the pipet tip cut off. For gelatin microwell arrays, the plate is simply incubated in a tissue culture incubator set to 37 °C for 20 minutes which returns the gelatin to liquid phase.

The microtissues can be recovered from single cell debris by pulsing a centrifuge to 1000 g and immediately stopping in order to remove residual single cells and/or gelatin. For creating bilayered structures, microtissues were simply removed from microwell arrays in the presence of a high concentration of a third cell type. For a 24 well plate this was 5 million cells in a 500 µL volume of PBS-CMF. For agarose versus gelatin as the mold material, we generally found that gelatin microwells were advantageous only for shapes outside an aspect ratio of 1 (rectangles and branched shapes) because melting the gelatin array gave higher yield than recovery by pipetting from the agarose array which resulted in fragmentation of some microtissues, presumably due to shear.

For the adhesion assay in the absence of ssDNA labeling (Figure 3-S1), cells were allowed to adhere in agarose microwells for the noted amount of time before transfer.

CELL SORTING AND STAINING

HMEC cells were cultured in M87A media and used at passage 4. Single cell suspensions were prepared by trypsinization in 1x TrypLE (Thermo), transferred to a 15 mL falcon tube and the trypsin quenched with fresh M87A. Cells were pelleted at 160xg for 4 minutes and resuspended in M87A at a concentration of 10^6 cells/mL. Cells were stained with anti-human FITC-MUC1 1:50 (BD Clone HMPV) and anti-human PE-CALLA 1:200 (Biolegend Clone HI 10A) for 30 minutes on ice. Cells were washed three times in PBS to remove excess antibody and resuspended in 2% BSA in PBS. Pure populations of MEPs and

LEPs were sorted from HMEC cultures using fluorescently activated cell sorting (FACS) on a FACSAriaII (BD). LEPs were selected as $MUC1^{+}/CALLA^{-}$ and MEPs were selected as $MUC1^{-}/CALLA^{+}$. Keratin staining was performed by fixing cultures in 4% PFA for 20 minutes at room temperature. Samples were then treated with blocking buffer (10% heat inactivated goat serum and 0.5% Triton X-100) for 1 hour at room temperature. Primary antibodies were diluted in blocking buffer and added overnight at 4° C. After incubation in primaries, excess antibody was removed by 3x 15 minute washes in blocking buffer. Fluorescently linked secondary antibodies were added at a dilution of 1:200 and incubated overnight. Following secondary incubation, samples were once again washed 3x with blocking buffer before imaging. Primary antibodies used in this study were mouse anti-human Keratin-19 (Sigma Clone A53-B/A2; 1:50 dilution) and rabbit anti-human Keratin-14 (Thermo RB-9020-P (polyclonal); 1:50 dilution) to mark LEPs and MEPs, respectively. Secondary antibodies were Goat anti-mouse IgG Alexa 647 (Abcam ab150115, 1:200 dilution) and Goat anti-rabbit IgG Alexa 488 (Abcam ab150077, 1:200 dilution).

CELL IMAGING

All images were collected using an inverted epifluorescence microscope (Zeiss Axiovert 200M, running Slidebook) with the exception of the confocal images in figure 3-2D and 3-2E which were acquired on a spinning disc confocal microscope (Zeiss Cell Observer Z1 with Yokagawa spinning disc, running Zen 2011).

OLIGONUCLEOTIDE SEQUENCES

Anchor Strands:

1) A: 5'-C_{24}-GTA ACG ATC CAG CTG TCA CT(T)$_{60}$ A CTG ACT GAC TGA CTG ACT G-3'

2) A': 5'-C_{24}-GTA ACG ATC CAG CTG TCA CT(T)$_{60}$ CAG TCA GTC AGT CAG TCA GT-3'

3) R: 5'-C_{24}-GTA ACG ATC CAG CTG TCA CT(T)$_{50}$ TAT CCT ATC CTG TGT GTG TGT ATC CTA TCC-3'

4) R': 5'-C_{24}-GTA ACG ATC CAG CTG TCA CT(T)$_{50}$ GGA TAG GAT ACA CAC ACA CAG GAT AGG ATA-3'

Co-Anchor Strands:

1) Co-Anchor: 5'-T_{30} AGT GAC AGC TGG ATC GTT AC-C_{24}-3'

Fluorescent Strands:

Complementary to A: FAM-5'-$(CAGT)_5$-3'

Complementary to A': FAM-5'-$(ACTG)_5$-3'

Complementary to R: FAM-5'-GGATAGGATACACACACACAGGATAGGATA-3'

Complementary to R': FAM-5'-TATCCTATCCTGTGTGTGTGTATCCTATCC-3'

MALDI MASS SPECTROSCOPY DATA

The purity and identity of fatty acid modified DNA oligonucleotides was confirmed by analytical HPLC and mass determination by MALDI-MS using a Shimadzu Biotech Axima Performance in positive linear mode with 3-hydroxy picolinic acid as the matrix. 2 µL of matrix was spotted on the plate, followed by 2 µL of a sample (50 µM). The combined solutions were mixed and spots were allowed to dry under atmospheric pressure. Measurements were performed on at least 5 separate spots for each sample. Mass resolution decreased with the length of the Fatty Acid-conjugated oligonucleotides, yielding sharp peaks for oligonucleotides less than 10 kD, and broad peaks for oligos over 20 kD.

Molecule	Actual MW	Measured (M+H)					Average	StDev
		1	2	3	4	5		
A	31025.46	31473.9	31471.79	31327.68	31,172.48	31,267.0	31342.6	131.2
A'	31025.46	31391.8	31349.12	31511.32	31396.52	31311.54	31392.1	75.1
R	30971.44	31353.9	31425.93	31506.01	31339.06	31345.41	31394.1	71.9
R'	31172.35	31506.0	31506.0	31470.5	31,396.95	31,235.61	31432.0	113.8
Co-Anchor	16112.39	16263.4	16258.1	16296.8	16254.8	16254.8	16265.6	17.8

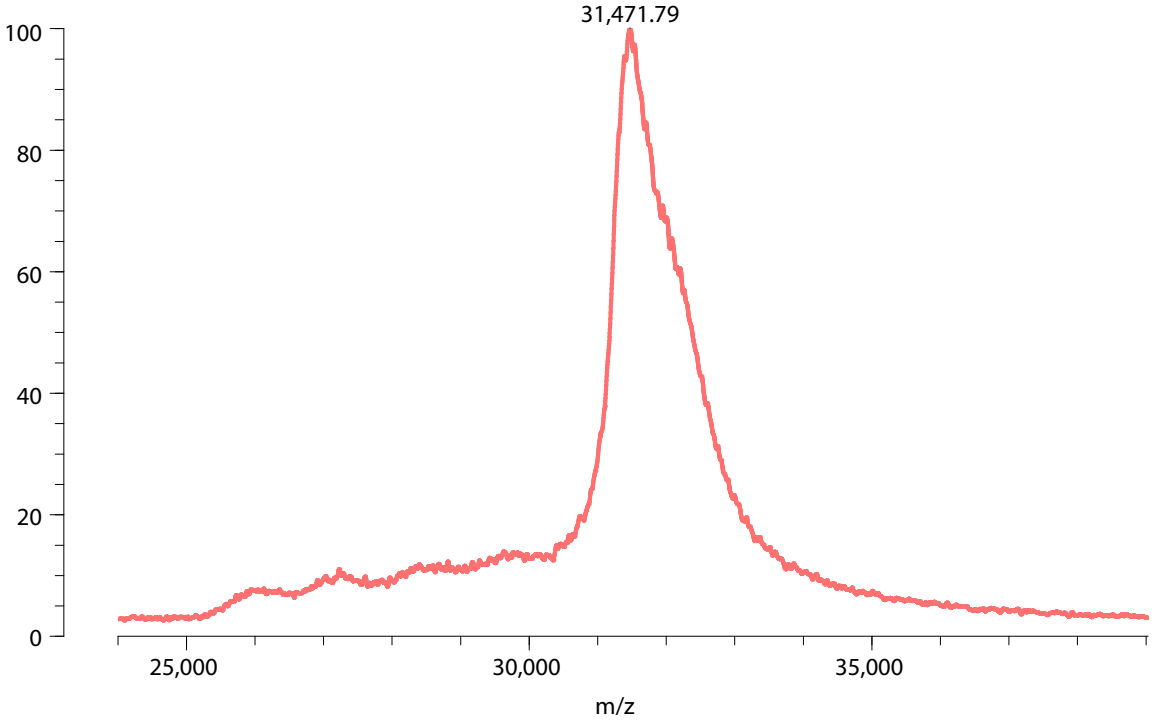

Representative MALDI trace of the A strand.

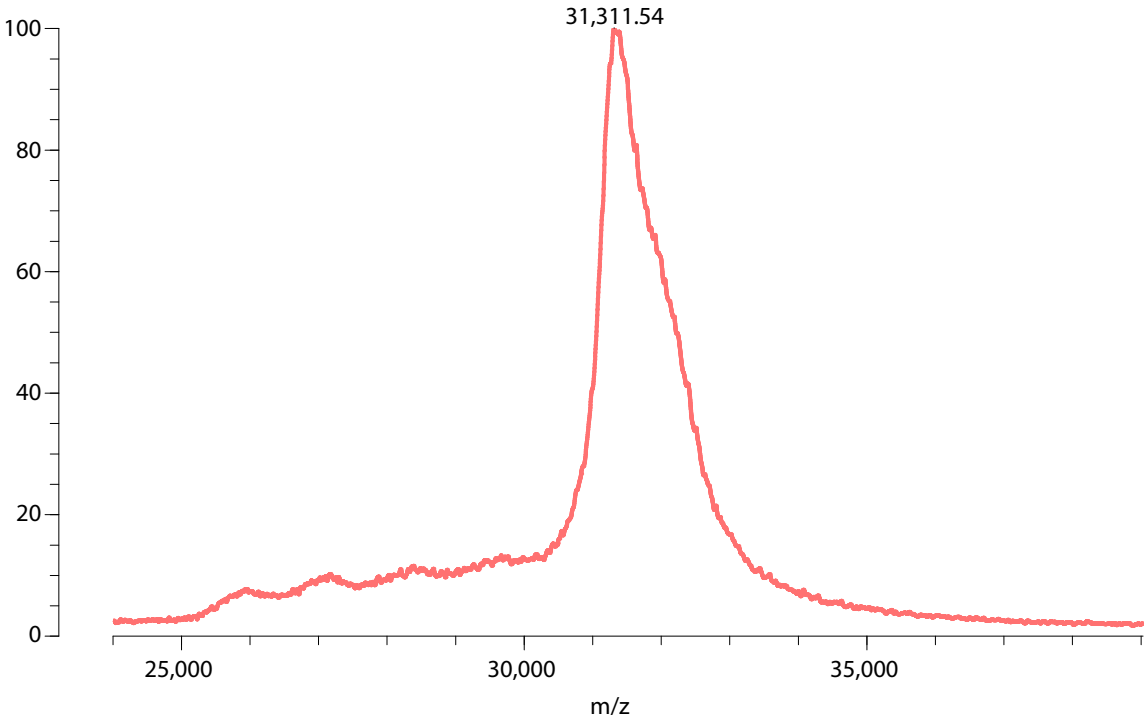

Representative MALDI trace of the A’ strand.

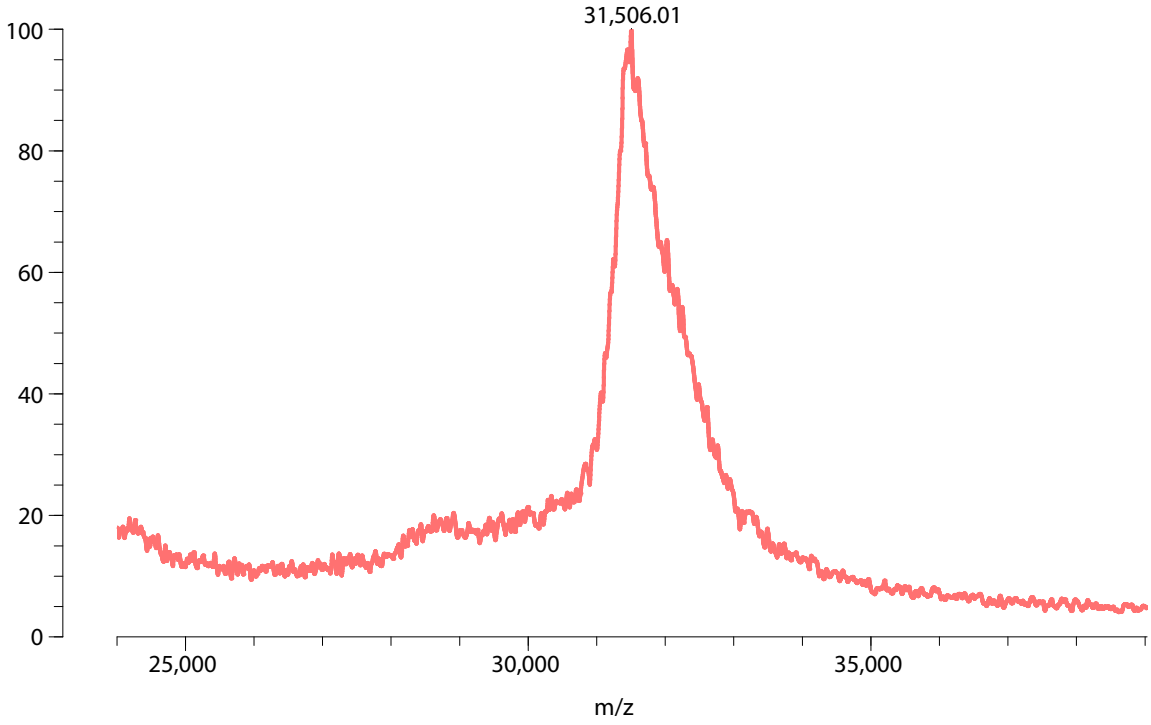

Representative MALDI trace of R strand.

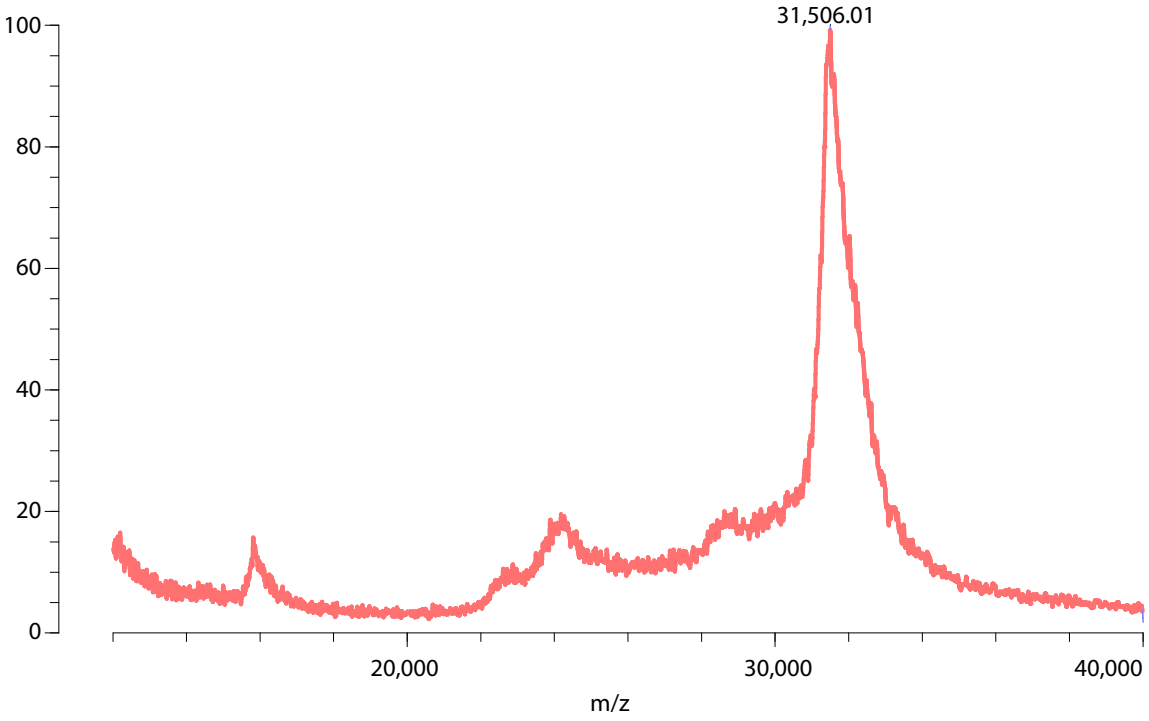

Representative MALDI trace of R’ strand.

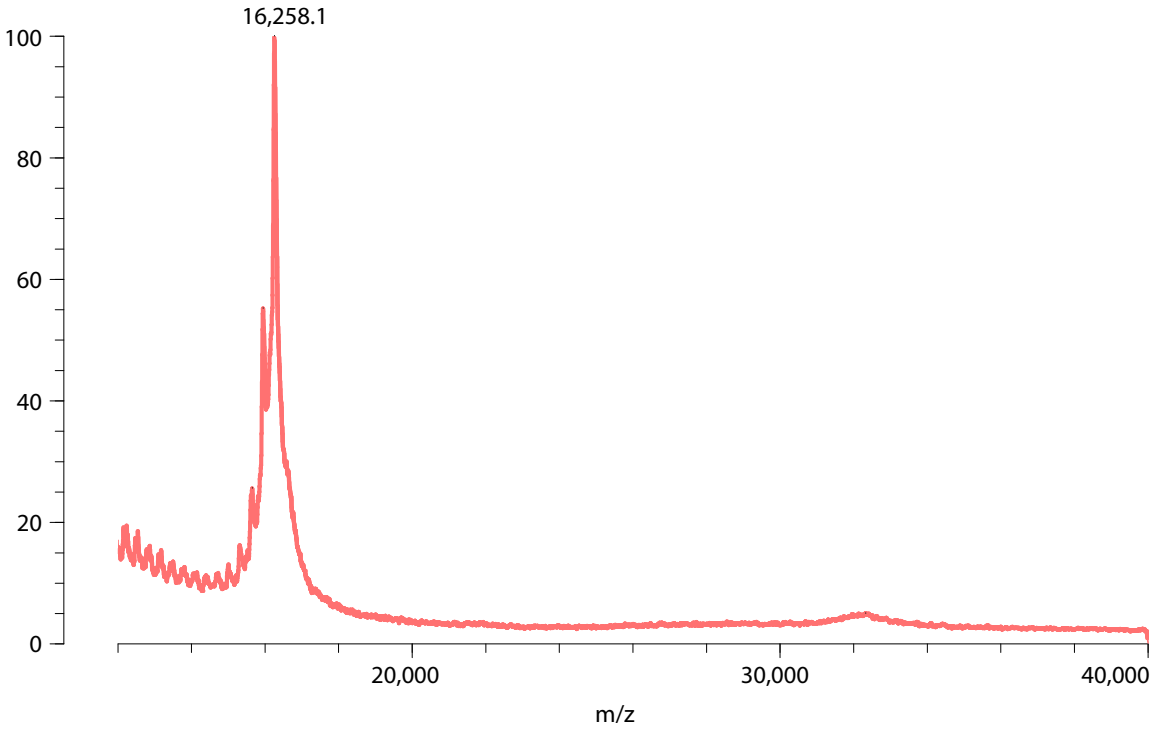

Representative MALDI trace of Co-Anchor.

REFERENCES

1. Lancaster, M. A.; Knoblich, J. A.Organogenesis in a dish: Modeling development and disease using organoid technologies Science 2014, 345 (6194) 1247125– 1247125, DOI: 10.1126/science.1247125

2. Ranga, A.; Gjorevski, N.; Lutolf, M. P.Drug discovery through stem cell-based organoid models Adv. Drug Delivery Rev. 2014, 69–70, 19– 28, DOI: 10.1016/j.addr.2014.02.006

3. Sachs, N.; Clevers, H.Organoid cultures for the analysis of cancer phenotypes Curr. Opin. Genet. Dev. 2014, 24, 68– 73, DOI: 10.1016/j.gde.2013.11.012

4. Khademhosseini, A.; Langer, R.; Borenstein, J.; Vacanti, J. P.Microscale technologies for tissue engineering and biology Proc. Natl. Acad. Sci. U. S. A. 2006, 103 (8) 2480– 2487, DOI: 10.1073/pnas.0507681102

5. Weigelt, B.; Ghajar, C. M.; Bissell, M. J.The need for complex 3D culture models to unravel novel pathways and identify accurate biomarkers in breast cancer Adv. Drug Delivery Rev. 2014, 69-70, 42, DOI: 10.1016/j.addr.2014.01.001

6. Clevers, H.Modeling Development and Disease with Organoids Cell 2016, 165 (7) 1586– 1597, DOI: 10.1016/j.cell.2016.05.082

7. Varner, V. D.; Nelson, C. M.Let’s push things forward: disruptive technologies and the mechanics of tissue assembly Integr. Biol. 2013, 5 (9) 1162, DOI: 10.1039/c3ib40080h

8. Shamir, E. R.; Ewald, A. J.Three-dimensional organotypic culture: experimental models of mammalian biology and disease Nat. Rev. Mol. Cell Biol. 2014, 15 (10) 647– 664, DOI: 10.1038/nrm3873

9. Sato, T.; van Es, J. H.; Snippert, H. J.; Stange, D. E.; Vries, R. G.; van den Born, M.; Barker, N.; Shroyer, N. F.; van de Wetering, M.; Clevers, H.Paneth cells constitute the niche for Lgr5 stem cells in intestinal crypts Nature 2011, 469 (7330) 415– 418, DOI: 10.1038/nature09637

10. Chan, H. F.; Zhang, Y.; Ho, Y.-P.; Chiu, Y.-L.; Jung, Y.; Leong, K. W. Rapid formation of multicellular spheroids in double-emulsion droplets with controllable microenvironment. Sci. Rep. 2013, 3 DOI: , DOI: 10.1038/srep03462

11. Shackleton, M.; Vaillant, F.; Simpson, K. J.; Stingl, J.; Smyth, G. K.; Asselin-Labat, M.-L.; Wu, L.; Lindeman, G. J.; Visvader, J. E.Generation of a functional mammary gland from a single stem cell Nature 2006, 439 (7072) 84– 88, DOI: 10.1038/nature04372

12. Karthaus, W. R.; Iaquinta, P. J.; Drost, J.; Gracanin, A.; van Boxtel, R.; Wongvipat, J.; Dowling, C. M.; Gao, D.; Begthel, H.; Sachs, N.Identification of Multipotent Luminal Progenitor Cells in Human Prostate Organoid Cultures Cell 2014, 159 (1) 163– 175, DOI: 10.1016/j.cell.2014.08.017

13. Takebe, T.; Enomura, M.; Yoshizawa, E.; Kimura, M.; Koike, H.; Ueno, Y.; Matsuzaki, T.; Yamazaki, T.; Toyohara, T.; Osafune, K.Vascularized and Complex Organ Buds from Diverse Tissues via Mesenchymal Cell-Driven Condensation Cell Stem Cell 2015, 16 (5) 556– 565, DOI: 10.1016/j.stem.2015.03.004

14. Cerchiari, A. E.; Garbe, J. C.; Jee, N. Y.; Todhunter, M. E.; Broaders, K. E.; Peehl, D. M.; Desai, T. A.; Labarge, M. A.; Thomson, M.; Gartner, Z. J.A strategy for tissue self-organization that is robust to cellular heterogeneity and plasticity Proc. Natl. Acad. Sci. U. S. A. 2015, 112 (7) 2287– 2292, DOI: 10.1073/pnas.1410776112

15. Xu, T.; Zhao, W.; Zhu, J.-M.; Albanna, M. Z.; Yoo, J. J.; Atala, A.Complex heterogeneous tissue constructs containing multiple cell types prepared by inkjet printing technology Biomaterials 2013, 34 (1) 130– 139, DOI: 10.1016/j.biomaterials.2012.09.035

16. Davies, J. A.; Chang, C.-H.Engineering kidneys from simple cell suspensions: an exercise in self-organization Pediatr. Nephrol. 2014, 29 (4) 519– 524, DOI: 10.1007/s00467-013-2579-4

17. Zhang, S. C.; Wernig, M.; Duncan, I. D.; Brüstle, O.; Thomson, J. A.In vitro differentiation of transplantable neural precursors from human embryonic stem cells Nat. Biotechnol. 2001, 19 (12) 1129– 1133, DOI: 10.1038/nbt1201-1129

18. Eiraku, M.; Takata, N.; Ishibashi, H.; Kawada, M.; Sakakura, E.; Okuda, S.; Sekiguchi, K.; Adachi, T.; Sasai, Y.Self-organizing optic-cup morphogenesis in three-dimensional culture Nature 2011, 472 (7341) 51– 56, DOI: 10.1038/nature09941

19. Greggio, C.; De Franceschi, F.; Figueiredo-Larsen, M.; Gobaa, S.; Ranga, A.; Semb, H.; Lutolf, M.; Grapin-Botton, A.Artificial three-dimensional niches

deconstruct pancreas development in vitro Development 2013, 140 (21) 4452–4462, DOI: 10.1242/dev.096628

20. Johnson, K. R.; Leight, J. L.; Weaver, V. M. Demystifying the Effects of a Three-Dimensional Microenvironment in Tissue Morphogenesis. In Methods in Cell Biology; Methods in Cell Biology; Elsevier, 2007; Vol. 83, pp 547– 583

21. Spencer, V. A.; Xu, R.; Bissell, M. J.Gene Expression in the Third Dimension: The ECM-nucleus Connection J. Mammary Gland Biol. Neoplasia 2010, 15 (1) 65– 71, DOI: 10.1007/s10911-010-9163-3

22. Xu, F.; Celli, J.; Rizvi, I.; Moon, S.; Hasan, T.; Demirci, U.A three-dimensional in vitro ovarian cancer coculture model using a high-throughput cell patterning platform Biotechnol. J. 2011, 6 (2) 204– 212, DOI: 10.1002/biot.201000340

23. Atefi, E.; Lemmo, S.; Fyffe, D.; Luker, G. D.; Tavana, H.High Throughput, Polymeric Aqueous Two-Phase Printing of Tumor Spheroids Adv. Funct. Mater. 2014, 24 (41) 6509– 6515, DOI: 10.1002/adfm.201401302

24. LaBarbera, D. V.; Reid, B. G.; Yoo, B. H.The multicellular tumor spheroid model for high-throughput cancer drug discovery Expert Opin. Drug Discovery 2012, 7 (9) 819– 830, DOI: 10.1517/17460441.2012.708334

25. Barrett, D. G.; Yousaf, M. N.Rapid Patterning of Cells and Cell Co-Cultures on Surfaces with Spatial and Temporal Control through Centrifugation Angew. Chem., Int. Ed. 2007, 46 (39) 7437– 7439, DOI: 10.1002/anie.200701841

26. Ozkumur, A. Y.; Goods, B. A.; Love, J. C.Development of a High-Throughput Functional Screen Using Nanowell-Assisted Cell Patterning Small 2015, 11 (36) 4643– 4650, DOI: 10.1002/smll.201500674

27. Kang, L.; Hancock, M. J.; Brigham, M. D.; Khademhosseini, A.Cell confinement in patterned nanoliter droplets in a microwell array by wiping J. Biomed. Mater. Res., Part A 2009, 9999A, NA– NA, DOI: 10.1002/jbm.a.32557

28. Gobaa, S.; Hoehnel, S.; Roccio, M.; Negro, A.; Kobel, S.; Lutolf, M. P.Artificial niche microarrays for probing single stem cell fate in high throughput Nat. Methods 2011, 8 (11) 949– 955, DOI: 10.1038/nmeth.1732

29. Giobbe, G. G.; Zagallo, M.; Riello, M.Confined 3D microenvironment regulates early differentiation in human pluripotent stem cells Biotechnol. Bioeng. 2012, 109, 3119– 3132, DOI: 10.1002/bit.24571

30. Nelson, C. M.; Inman, J. L.; Bissell, M. J.Three-dimensional lithographically defined organotypic tissue arrays for quantitative analysis of morphogenesis and neoplastic progression Nat. Protoc. 2008, 3 (4) 674– 678, DOI: 10.1038/nprot.2008.35

31. Cerchiari, A.; Garbe, J. C.; Todhunter, M. E.; Jee, N. Y.; Pinney, J. R.; Labarge, M. A.; Desai, T. A.; Gartner, Z. J.Formation of Spatially and Geometrically Controlled Three-Dimensional Tissues in Soft Gels by Sacrificial Micromolding Tissue Eng., Part C 2015, 21 (6) 541– 547, DOI: 10.1089/ten.tec.2014.0450

32. Raab, M.; Swift, J.; Dingal, P. C. D. P.; Shah, P.; Shin, J.-W.; Discher, D. E.Crawling from soft to stiff matrix polarizes the cytoskeleton and phosphoregulates myosin-II heavy chain J. Cell Biol. 2012, 199 (4) 669– 683, DOI: 10.1083/jcb.201205056

33. Paszek, M. J.; Zahir, N.; Johnson, K. R.; Lakins, J. N.; Rozenberg, G. I.; Gefen, A.; Reinhart-King, C. A.; Margulies, S. S.; Dembo, M.; Boettiger, D.Tensional homeostasis and the malignant phenotype Cancer Cell 2005, 8 (3) 241– 254, DOI: 10.1016/j.ccr.2005.08.010

34. Soofi, S. S.; Last, J. A.; Liliensiek, S. J.; Nealey, P. F.; Murphy, C. J.The elastic modulus of Matrigel as determined by atomic force microscopy J. Struct. Biol. 2009, 167 (3) 216– 219, DOI: 10.1016/j.jsb.2009.05.005

35. Lewis, M. T.; Landua, J. D.; Adams, H. C.; Medina, D.A Mystery Wrapped in an Enigma: Matrigel Enhancement of Mammary Cell Growth and Morphogenesis J. Mammary Gland Biol. Neoplasia 2012, 17 (2) 99– 101, DOI: 10.1007/s10911-012-9249-1

36. Kleinman, H. K.; McGarvey, M. L.; Hassell, J. R.; Star, V. L.; Cannon, F. B.; Laurie, G. W.; Martin, G. R.Basement membrane complexes with biological activity Biochemistry 1986, 25 (2) 312– 318, DOI: 10.1021/bi00350a005.

37. Gartner, Z. J.; Bertozzi, C. R.Programmed assembly of 3-dimensional microtissues with defined cellular connectivity Proc. Natl. Acad. Sci. U. S. A. 2009, 106 (12) 4606– 4610, DOI: 10.1073/pnas.0900717106

38. Hsiao, S. C.; Shum, B. J.; Onoe, H.; Douglas, E. S.; Gartner, Z. J.; Mathies, R. A.; Bertozzi, C. R.; Francis, M. B.Direct cell surface modification with DNA for the capture of primary cells and the investigation of myotube formation on defined patterns Langmuir 2009, 25 (12) 6985– 6991, DOI: 10.1021/la900150n

39. Twite, A. A.; Hsiao, S. C.; Onoe, H.; Mathies, R. A.; Francis, M. B.Direct Attachment of Microbial Organisms to Material Surfaces Through Sequence-Specific DNA Hybridization Adv. Mater. 2012, 24 (18) 2380– 2385, DOI: 10.1002/adma.201104336

40. Selden, N. S.; Todhunter, M. E.; Jee, N. Y.; Liu, J. S.; Broaders, K. E.; Gartner, Z. J.Chemically Programmed Cell Adhesion with Membrane-Anchored Oligonucleotides J. Am. Chem. Soc. 2012, 134 (2) 765– 768, DOI: 10.1021/ja2080949

41. Weber, R. J.; Liang, S. I.; Selden, N. S.; Desai, T. A.; Gartner, Z. J.Efficient Targeting of Fatty-Acid Modified Oligonucleotides to Live Cell Membranes through Stepwise Assembly Biomacromolecules 2014, 15 (12) 4621– 4626, DOI: 10.1021/bm501467h

42. Zhang, D. Y.; Winfree, E.Control of DNA Strand Displacement Kinetics Using Toehold Exchange J. Am. Chem. Soc. 2009, 131 (47) 17303– 17314, DOI: 10.1021/ja906987s

43.Li, Q.; Luan, G.; Guo, Q.; Liang, J.A new class of homogeneous nucleic acid probes based on specific displacement hybridization Nucleic Acids Res. 2002, 30, 5e, DOI: 10.1093/nar/30.2.e5

44. Todhunter, M. E.; Jee, N. Y.; Hughes, A. J.; Coyle, M. C.; Cerchiari, A.; Farlow, J.; Garbe, J. C.; Labarge, M. A.; Desai, T. A.; Gartner, Z. J.Programmed synthesis of three-dimensional tissues Nat. Methods 2015, 12 (10) 975– 981, DOI: 10.1038/nmeth.3553

FIGURES

Figure 3-1. Chemical micromolding.

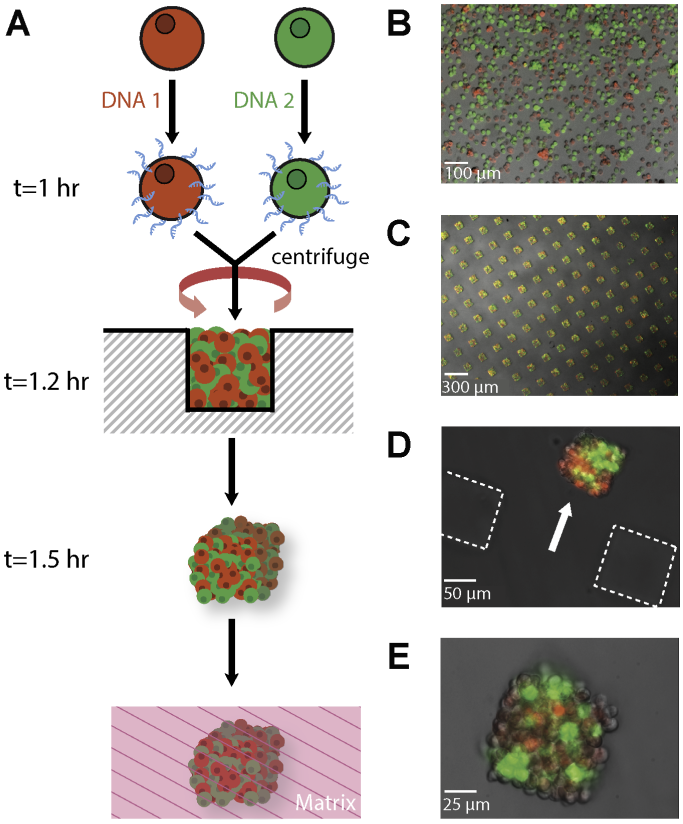

(a) Two cell populations are labeled with complementary ssDNA, mixed, and rapidly centrifuged into microwells. Cell surface ssDNA strands anneal only in the wells, locking cells into microtissues that conform to the shape of the microwells. Reconstituted microtissues are subsequently recovered from microwells and can be cultured in a 3D matrix of choice. (b) Field of cells stained red and green before centrifugation into microwells. (c) Representative field of cuboidal microtissues within microwells. (d) Representative microtissue (arrow) removed from its microwell (dotted lines). (e) Cuboidal microtissue embedded in culture.

Figure 3-2. Capping strands allow transfer of intact cell aggregates to hydrogels for 3D culture.

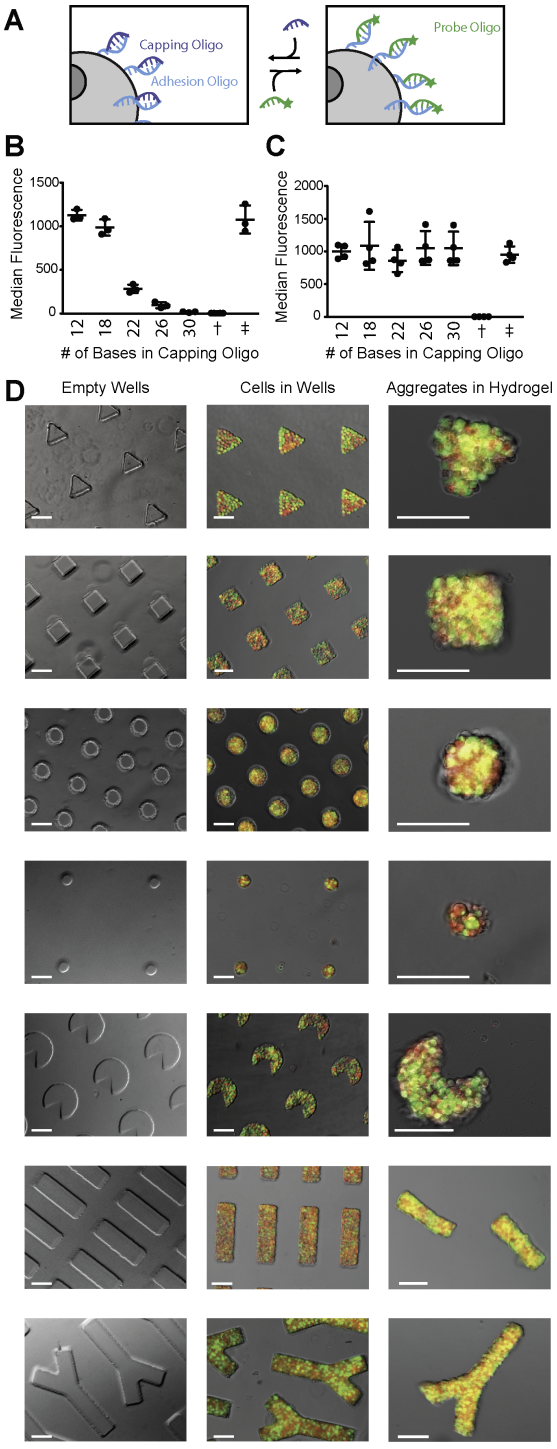

(a) Scheme illustrating the assays in B and C: Preannealed capping strands are displaced by a fluorescent probe and preannealed fluorescent probes are displaced by capping strands by single strand invasion. (b) Cells labeled with ssDNA are first treated with different lengths of capping strand and then a complementary fluorescent probe and measured by flow cytometry to test the effectiveness of capping strands at blocking subsequent binding events. (c) Cells labeled with ssDNA are first treated with complementary fluorescent oligo and then incubated with capping strand of the indicated length to test the stability of pre-existing hybridization events to strand displacement by the capping strand. † indicates cells with no DNA (negative control), ‡ indicates cells with DNA but no capping strand (positive control). (d) Gallery of shapes showing empty wells, filled wells, and structures transferred to hydrogel. Scale bars are 100 μm.

Figure 3-3. Multistep microtissues prepared by chemical micromolding.

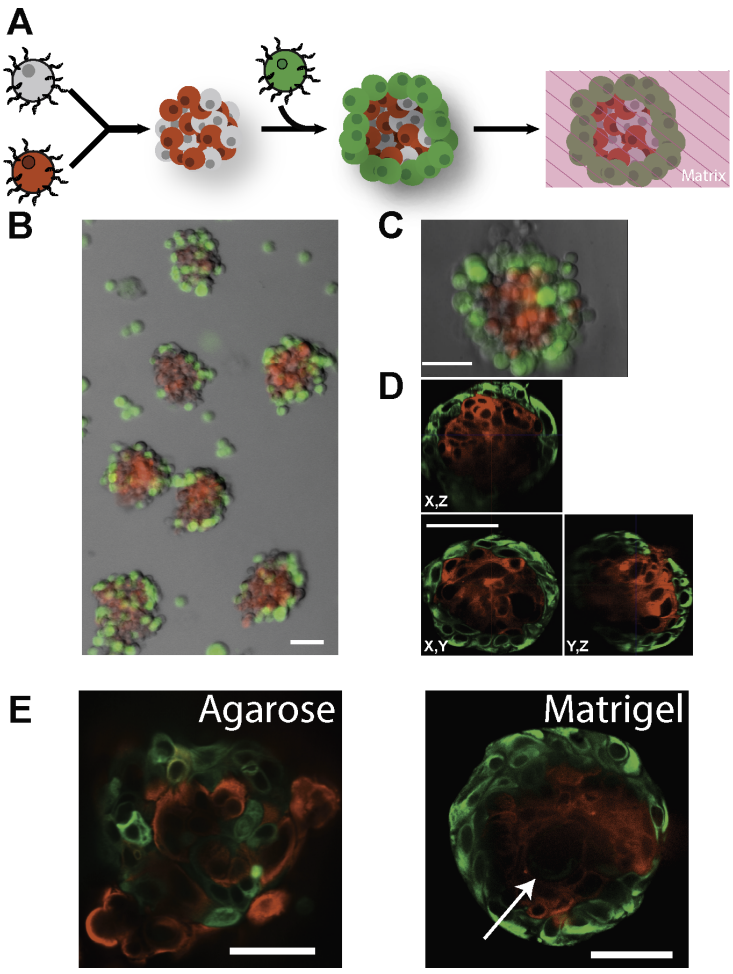

(a) Scheme for iterating chemical micromolding to make a core–shell cellular aggregate. Red and unstained (gray) cells are first molded into spheroids before addition of a layer of green cells. (b) Core–shell aggregates made from Jurkats, and (c) HMECs. (d) Immunofluorescence confocal image of HMECs after self-organization in matrigel for 24 h stained with LEP marker keratin-19 (red) and MEP marker keratin-14 (green). (e) Higher-magnification views of representative microtissues after 24 h in agarose and matrigel. Arrow indicates a forming lumen. Scale bars are 50 μm.

SUPPLEMENTARY

Figure 3-S1. Adhesive Cells Coalescing In Microwells and Transferred Without DNA Do Not Retain Shape of Microwells.

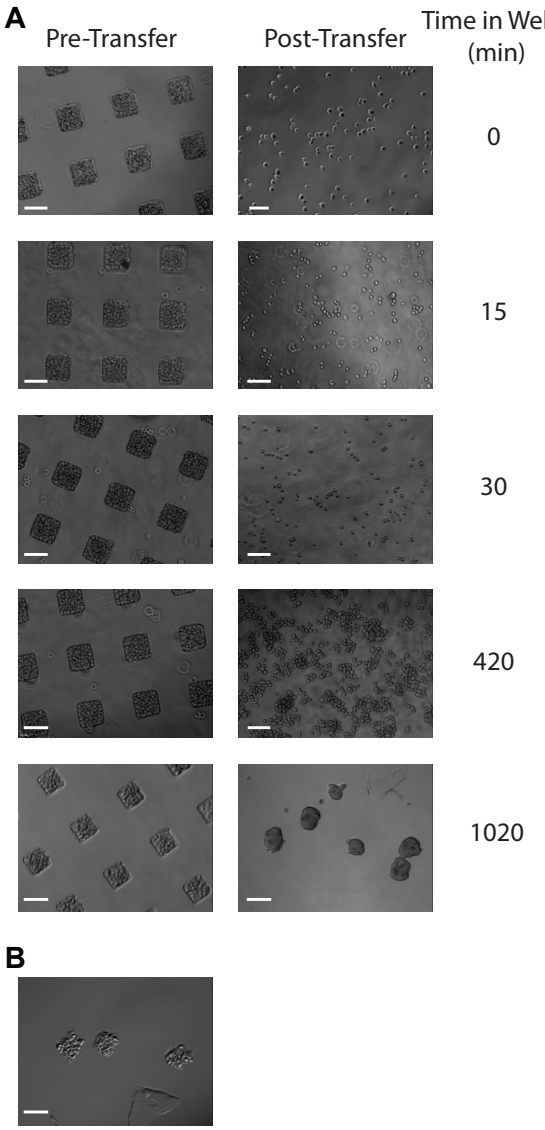

(a) MCF10A cells, a cohesive epithelial cell line, were cast into square microwells, imaged and recovered from microwells at the indicated time. No adhesion occurred when transferred between 0 to 30 minutes, resulting in a

spectrum of dissociated cells and small aggregates. By 420 minutes, some cell adhesion was observed, but the transferred cells were still composed of incomplete, rounded aggregates. By 1020 minutes, the cells are fully adhered, but also fully rounded with individual cells no longer readily apparent. This is in contrast to the complete MCF10A squares seen in (b) after only 10 minutes of DNA-mediated adhesion in the wells followed by 10 minutes incubation with capping strand. Scale bars are 100 μm. Brightness of images was adjusted to be similar across samples.

Figure 3-S2. R/R' Show Slower Assembly Kinetics than A/A'.

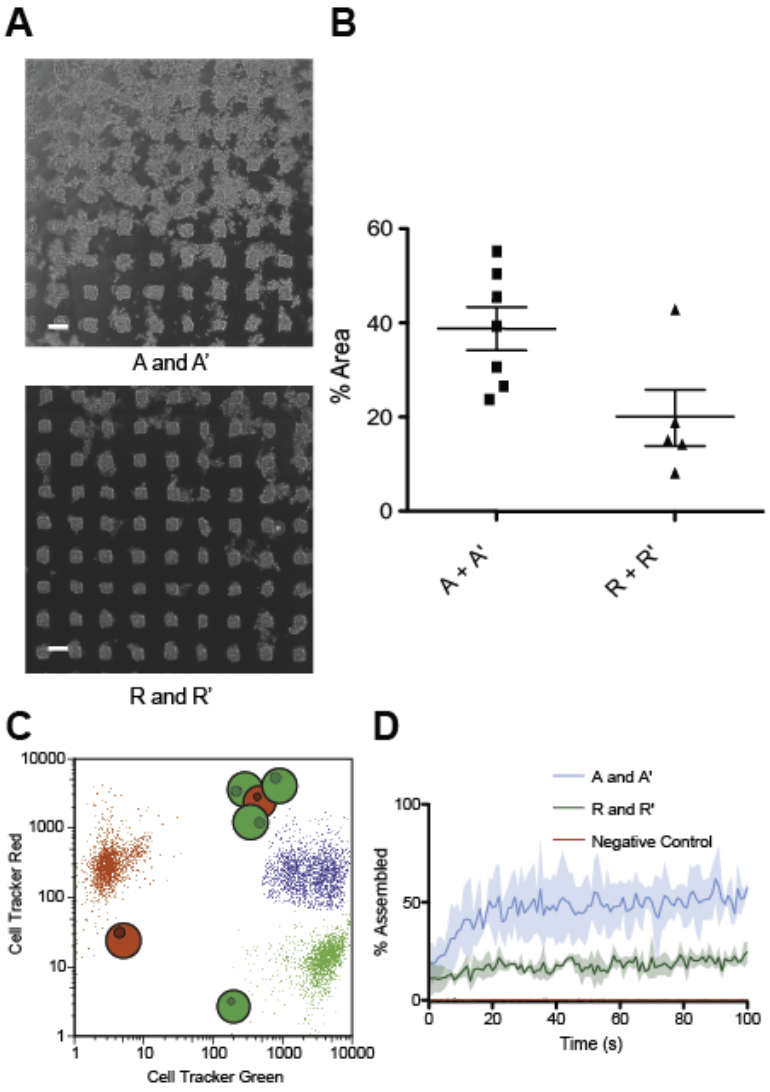

(a) Bright-field microscopy images depicting cell aggregates (grey) forming outside of wells labeled with the combination of A and A' oligonucleotides or the more heterogeneous R and R' oligonucleotides. Scale bars are 200 μm. (b) Quantification of the percentage of surface area obscured by aggregates outside of microwells. Each point is a separate microwell array and the line depicts the mean ± 1 SEM. (c) Flow cytometry scatter plot showing gating for quantifying aggregate formation. The FACS plot shows the flow positions of red cells alone,

green cells alone and assembled cells. To measure the rate of assembly, red and green cells were complementarily labeled, mixed at a ratio of 1:50 respectively, and rapidly put onto the flow cytometer. (d) Kinetics of Assembly. The plot shows the percentage of red cells moving from the red cloud (red cells only) to the blue cloud (red and green cells assembled) over 100 seconds. The plotted lines are the mean of N=3 samples, the shaded area is ±1 SD. Negative cells were not labeled with any DNA. Brightness of images in A was adjusted to be similar between the two samples.

Figure 3-S3. Scale-up of Chemical Micromolding With a Larger Stamp.

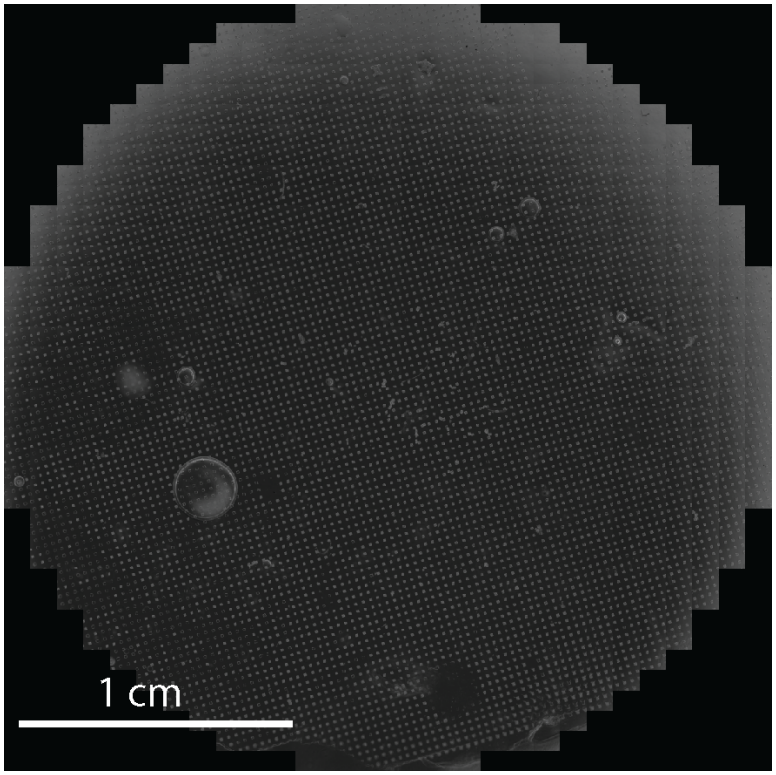

A 10x tiled image across a large microwell array full of chemically micromolded tissues. The array is approximately 107 microwells in diameter and comprises approximately 9,000 microwells in total. It was prepared in the same manner and using the same centrifugation time as smaller arrays with the number of cells increased proportionally to the increased surface area of the array. The array has approximately 80% occupancy with loss due to stamp imperfections as well as aggregates washed out of microwells during the removal of excess cells. This array was produced in 1 well of a 6 well plate. To scale up, one could simply use more wells of the plate or more plates.

Figure 3-S4. Efficiency of labeling cells with two unique strands of DNA.

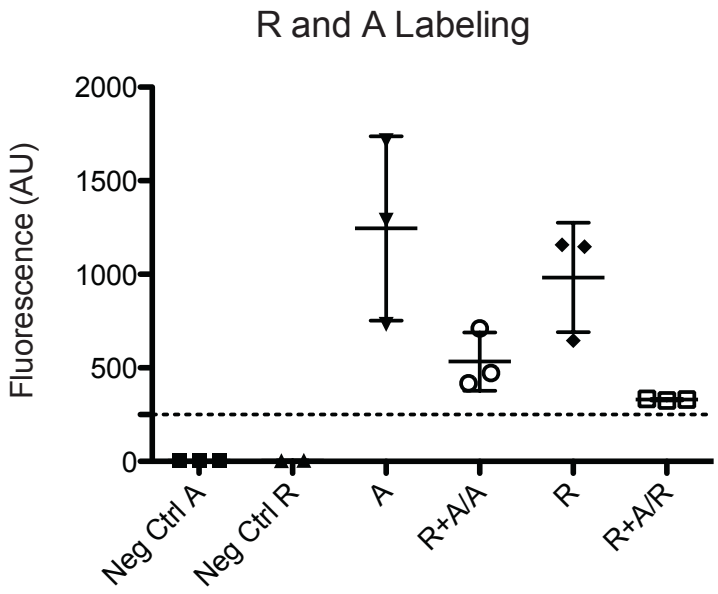

Cells were labeled with 1 μM of both A and R strands simultaneously and 2 μM of CoA-essentially a double dose of FA-DNA and then split in half and annealed to a FITC-oligo complementary to A and R respectively and fluorescence was measured by flow cytometry. There is a reduction in the amount of fluorescence from each strand as compared to singly labeled controls indicating that less of each is incorporated. However, labeling was still above the minimum for cell-cell adhesion (dotted line).

Table 3-S1. Map of R Strand Adhesion Region and Capping Strands as a Function of Length.

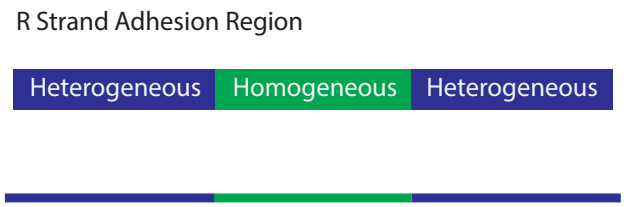

Capping Sequences 5'-3'	# Bases	ΔG(kcal/mol)[4]	Graphical Depiction
TACACACACACA	12	11.9	
GGATACACACACACAGGA	18	21.5	
TAGGATACACACACACAGGATA	22	25.7	
GATAGGATACACACACACAGGATAGG	26	31.7	
GGATAGGATACACACACACAGGATAGGAT	30	37.1	

The adhesion region of the R/R' strands has a central region of repeating 2mers flanked by more heterogeneous regions. The repetitive region has been shown to have more rapid kinetics of annealing to complementary sequences in contrast to the more heterogeneous sequences. The capping strands are listed by sequence, number of bases, energy of binding, and a graphical depiction of where the capping strands bind.

CHAPTER 4

SINGLE CELL RNA SEQUENCING OF MAMMARY GLAND ORGANOIDS

Source: This is original work, not yet compiled for publication. I worked closely on the sequencing with Dr. Lyndsay Murrow, PhD. I also worked closely with Dr. Joseph (Tony) Caruso and Professor Thea Tlsty for the acquisition, processing, and follow-up studies of primary human mammary gland samples.

Contributions: Lyndsay, Tony and I initiated the project and performed the majority of the experiments. Tutorials about RNA Sequencing and analysis was obtained through a number of discussions by Dr. Sisi Chen, Mr. Emeric Charles, Dr. Thomas Norman, and Professor Eric Chow. I wrote this version of what will become a future manuscript with figure contributions from Lyndsay Murrow and Tony Caruso. Zev Gartner, Tejal Desai, Thea Tlsty, and Matt Thomson supervised the project.

INTRODUCTION

As described in the introduction, the mammary gland is primarily composed of a bilayered, epithelial tree embedded in a stromal compartment with numerous fibroblasts and adipocytes among other cell types. Our current understanding of the epithelial populations that exist in the mammary gland is limited to the major subpopulations that can be purified in flow cytometry based on differences in their surface proteome: myoepithelial cells (MEPs), mature luminal cells (LEPs) and luminal progenitors (LPs).[1] Furthermore, there is controversy in the field as to what the correct flow cytometry markers are for stem cells.[2] It is well known that there is further heterogeneity within these cell types, the most obvious example being hormone receptor positive cells within the luminal population. As described in the introductory chapter, hormone responsive LEPs are those that express the nuclear hormone receptors for estrogen (ER/ESR1) and progesterone (PR/PGR).[3] These receptors are primarily present in the cytoplasm, bound by heat shock proteins until engagement with their cognate ligand causes an allosteric shift resulting in dimerization and translocation to the nucleus where they act as transcription factors for a host of hundreds of other genes.[4] The reliance on surface proteome differences to isolate live cell types presents a challenge to isolating this interesting subpopulation of cells as the primary protein marking their difference is cytoplasmic rather than on the surface. However, this issue extends beyond just isolation of hormone receptor positive cells. Multiple works have underscored the fact that we simply do not understand the heterogeneity or hierarchy of the

epithelial mammary gland as well as we do for other tissues.[3] In particular, comparisons are often drawn to the hematopoietic stem cell hierarchy, the complete description of which has allowed major advances in understanding and treating blood disorders.[5]

Our general hypothesis is that within each major cell type there exist subtypes of cells as of yet unrealized due to an inability to purify and analyze them. We further hypothesize that differences between these subtypes will be observable by measuring differences in mRNA expression. This is an ideal problem to tackle with single cell RNA sequencing (scRNA seq) as it offers an unbiased and global assessment of the transcription state of individual cells. We will theoretically be able to define transcriptional programs that delineate different subtypes. To that end, we obtained healthy, mammary reduction samples from 5 women (Supplementary Table 1) and using the massive throughput offered by modern, droplet-based single cell sequencing technologies, [6-9] we measured the expression profile from nearly 10,000 cells per mammoplasty sample.

RESULTS AND DISCUSSION

Fluorescence activated cell sorting (FACS) was used to purify live cells as well as to collect cells in 3 different classes: 1. All living cells, 2. All living LEPs, and 3. All living MEPs. We used this enrichment strategy to ensure that we had sufficient epithelial cell profiles from which to draw potentially subtle conclusions. As we were collecting these fractions, we also observed that samples from women who had a previous history of pregnancy (Gravidity/Parity greater than 1)

(Supplementary Table 1) had concomitant changes in their FACS profile (Table 1). The most notable change was a large increase in the proportion of MEPs (Figure 4-1). It has long been known that pregnancy is protective of breast cancer, [10] however these changes are often attributed to changes in signaling pathways within cells[11,12] and in contrast, showed a decrease in proliferation potential within the basal population.

We collected the cells from flow cytometry and immediately prepared transcriptome libraries using 10x 3' counting kit as per manufacturers instructions.[6] We sequenced the libraries on an Illumina HiSeq4500 and used 10x's CellRanger software to produce digital expression matrices. One sample was processed with V1 chemistry and the subsequent 4 were processed with V2 chemistry. In order to avoid chemistry related batch effects, only the 4 V2 samples were aggregated for analysis (Supplementary Table 1). In analyzing these expression matrices using the Seurat R package[13], and using suggested default settings for defining variable genes, the first thing we observed was the ease of distinguishing the major cell subtypes, MEPs, LEPs, Luminal Progenitors, and Stroma using a t-SNE projection based on statistically significant principle components (Figure 4-2). To assign cluster identities, we used well-documented markers of each major cell type, for example, Keratin 18, Keratin 19, and Claudin 4 for LEPs (Supplementary Table 4-S2). The ease of separating these major cell types was even apparent just looking at projections of cells on the first 2 principal components (Figure 4-3) of variable genes and suggests that there are significant differences between these cells at the level of

the transcriptome that are represented in the first few principal components. Using marker analysis, we were able to assess the top genes that mark each of these major populations (Supplementary Table 2). However, when labeling this same data by the reduction mammoplasty from which the cells originated, it became readily apparent that there were significant sample-to-sample differences driving the organization of the data as well (Figure 4-4). For analyzing differences between major cell types, the batch effects do not appear to present major difficulties – using t-SNE, the major cell types are still well separated. However, when subsetting on one cell type, for example mature LEPs, and repeating the Seurat clustering pipeline, including defining variable genes, batch effects present a more significant challenge. Using the same approach as for all cells, t-SNE primarily organizes mature LEPs by batch rather than in any kind of meaningful subtypes (Figure 4-5). This is likely because differences between subtypes of mature LEPs, if they exist at all, are subtler than differences between mature LEPs and MEPs, for example. In this data set, it is challenging to parse technical batch effects from biological batch effects as each sample was processed independently and also originated from a different woman.

To address this challenge, we used Seurat's native batch correction, which removes genes whose expression pattern is likely associated with a sample. We set the AUC cutoff for this measurement to 0.7. The batch correction algorithm removed a handful of genes strongly correlated with sample identification within the mature LEP cell type, organized by a hierarchical clustering algorithm (Figure 4-6). We plotted the remaining cell by gene matrix as a heatmap also organized

by a hierarchical clustering algorithm (not shown). It is apparent from the batch gene corrected Heatmap that there are blocks of genes that vary within each sample yet overall there is still primarily strong organization by sample instead of mixing between the samples. Part of this may be due to a preganancy/non-pregnancy split as we observed in FACS. However, of the two samples without a history pregnancy, RM272 stands out from its counterpart, RM273, for high expression of a number of transcripts downstream of estrogen receptor alpha (TFF1, TFF3, AREG, AZGP1)[14] and progesterone receptor (RANKL, WNT4).[15] If this effect is biological rather than technical, it indicates a high level of hormone signaling in RM272 compared to RM273 which could correspond to undocumented use of hormonal birth control in this patient, or that the reduction mammoplasty sample of RM272 was collected in the luteal phase of the menstrual cycle and the others in the follicular phase.[16] Thus, even with batch correction, many clustering algorithms get trapped in a local minima and organize the mature LEPs into 3 clusters: The two with the history of pregnancy (RM264 and 282), the high hormonal signaling, RM272, and finally RM273.

To overcome the local minima problem with various other clustering algorithms, we used an approach called Nonnegative Matrix Factorization (NNMF) [17,18] to break the cell by gene matrix into two substituent matrices: basis by gene and cells by mixture coefficients. These two matrices, when multiplied together, result in the original matrix. In this analysis, the basis genes represent gene modules that describe subtypes of cells in the data and the mixture coefficients describe groupings of cells (Figure 4-7). Thus, NNMF simultaneously

provides cell clustering and gene modules through factorizing the cells by gene expression matrix. A required input of NNMF is to set the number of clusters/cell types (called rank number) for the factorization fit the data to. For mature LEPs, this number was determined empirically by doing 30 simulations of the factorization for rank numbers 2 through 10 and measuring the error between the original data matrix and the matrix that results from multiplying together the resulting basis by gene and cells by mixture matrices. Our goal was to set rank to the number greater than 3 which minimized error in the resulting matrix to overcome the issues described above. Using the dispersion and cophentic metrics, it is apparent that there is a local minimum in error of the resulting matrix at a rank of 5 (Figure 4-8). Thus, we set rank to 5 and factored the matrix using the Brunet algorithm.[19] The resulting gene modules and cell clustering is organized for a subset of genes defined as 'variable genes' in the Seurat pipeline. As described above, variable genes are defined as transcripts with expression values meeting an arbitrary dispersion threshold (0.5) and expression threshold, (0.0125 to 6 on a log10 scale) across the data matrix. However, our interest is in fully describing the gene modules that represent these cell types. To that end, we used the cell clustering from NMF to assign cluster IDs in Seurat and then used those cluster IDs to determine all markers that correlated with those clusters from the entire expression matrix, even for those transcripts that did not meet the cutoffs for a variable gene. We plotted these markers as a mature LEPs by cluster markers matrix (Figure 4-9). Using this approach and

applying it to other major cell classes, we will be able to define the number of subtypes as well as the transcripts that drive those subtypes.

CONCLUSION

This work is ongoing, but it seems clear that while t-SNE is very useful for separating major cell types, the approach is more difficult for parsing subtle subtypes within a major cell type. It appears that Nonnegative matrix factorization (NMF) is a successful strategy to identify gene modules for subtypes, exemplified here in mature luminal cells. We will continue the same process for the other major cell types: myoepithelial cells and luminal progenitors.

Despite our best efforts to minimize the time between steps, ultimately, scRNA sequencing is susceptible to technical variations induced by freezing and thawing the cells as well as the various processing steps to get to a purified, live single cell population (see methods section). Furthermore, there is not always a consistent relationship between mRNA transcript levels and protein expression with a pearson correlation between mRNA transcript and protein abundance in the realm of 0.4-0.6. [20,21] This is typically attributed to regulation at the level of translation and mRNA degradation rather than simply expression level. However, recent studies suggest there is better correlation for differentially expressed transcripts which is the basis of the present study. In the face of this unknown, it is imperative to confirm RNA sequencing findings by RNA FISH and IHC in matched tissue samples to ensure that the gene programs observed are not artifactual due to inherent differences between mRNA and protein levels or

induced by cell handling – particularly stress-response programs. Addressing these questions will be the immediate next steps of this work.

METHODS

TISSUE SAMPLES AND PREPARATION

Reduction mammoplasty tissue samples and medical reports with personally identifiable information redacted were obtained by the Tlsty lab. Breast tissue was processed into 150 μm in diameter organoids as previously described (Jove). Organoid aliquots were frozen and maintained at -180 °C until use. Separately, a sample of each sample in the organoid archive was formalin fixed and embedded in paraffin blocks for follow-up work.

FLOW CYTOMETRIC ANALYSIS OF MAMMARY GLAND ORGANOIDS

Organoid ampules were thawed at 37 °C until thawed (1-3 minutes). Cells were transferred to a 15 mL conical with 5 mL of 0.05% trypsin (UCSF Cell Culture Facility) and titurated for 2 minutes with a 1 mL pipet. The trypsin was quenched by adding 10 mL of Hanks Balanced Salt Solution (HBSS, ThermoFisher 14025092) supplemented with 2% v/v fetal bovine serum (FBS) (UCSF Cell Culture Facility). The cells were pelleted by centrifugation for 5 minutes at 1300 rpm. The supernatant was aspirated and the pellet was resuspended in 4 mL of Dispase (Stem Cell Technologies 07913) and DNase I (Stem Cell Technologies 07900) in HBSS, 5 U/mL and 1 mg/mL respectively. The pellet was again titurated for 2 minutes with a 1 mL pipet. The dispase and DNase I were subsequently quenched with 10 mLs of HBSS supplemented with

2% FBS. The resulting cell suspension was filtered through a 40 μm filter into a clean 50 mL falcon tube. The tube and filter were washed with aliquots of HBSS + 2% FBS. The cell suspension was transferred to a clean 15 mL falcon tube and pelleted at 1300 rpm for 5 minutes. The supernatant was removed and the pellet was resuspended in 10 mL of complete mammary epithelial growth medium with 2% v/v FBS and without GA-1000(MEGM) (Lonza CC-3150). Cells were incubated in a 37 °C for 2 hours, rotating on a hula mixer (ThermoFisher 15920D). After incubation, cell viability was assessed with by staining a sample 1:1 with trypan blue and measuring on a hemocytometer. Cells were pelleted at 1300 rpm for 5 minutes and resuspended in phosphate buffered saline (PBS) (UCSF Cell Culture Facility) supplemented with 1% BSA at a concentration of 1 million cells per 100 μL in a 15 mL falcon tube.

Cells were incubated with the primary antibodies and at the concentrations listed in supplementary table 3 for 15 minutes at room temperature on a platform rocker. After 15 minutes, 10 mL of PBS + 1% BSA was added and the cells were pelleted for 5 minutes at 1300 rpm. The cells were again resuspended in PBS + 1% BSA at a concentration of 1 million cells per 100 μL. 1 μL per 1 million cells of Streptavidin-BV785 (Biolegend 405249) was added and cells were incubated for 15 minutes on a platform rocker. In the final 5 minutes of streptavidin staining, DAPI (2 drops per million cells)(Thermo, NucBlue, R37606) was added. After this staining cells were once again washed and resuspended in PBS + 1% BSA. Cells were maintained on ice until sorted.

For flow cytometry, a FACS Aria 2 was used (UCSF Laboratory for Cellular Analysis). Cells were gated on low DAPI signal for viability as well as low BV785 signal to create a population depleted of immune and stromal cells. The remaining cells were sorted on EpCAM-FITC and CD49f-PE for which 4 populations were observed (Supplementary Figure 4-S1). Mature luminal epithelial cells were defined as cells that were EpCAM+CD49f-, luminal progenitors as EpCAM+CD49f-, myoepithelial cells as EpCAM-CD49f+. Double negative cells were presumed to be from the stromal compartment. For each reduction mammary sample we collected 3 separate samples of 10,000 cells from 'All Live' (DAPI negative), myoepithelial, and all luminal cells.

cDNA Library Preparation and Sequencing

Following flow cytometry, cells were resuspended at the appropriate concentration for sequence 3,000 cells in non-acetylated BSA (Thermo Fisher AM2616). Cells were immediately taken to the 10x Chromium Controller instrument for encapsulation. From there cDNA libraries were produced in accordance with the 10x manual (V1 and V2) following the quality and size constraints therein. Concentrations for final libraries were quantified by a combination of high sensitivity DNA bioanalyzer (Agilent, 5067-4623), qPCR against Illumina adaptors(Kapa Biosystems KK4824), and qubit (Thermo Fisher Q32851). Each library was separately sequenced on a lane of a HiSeq4500 following the settings recommended in the 10x manual.

Bioinformatic Analysis of Sequencing Outputs

We processed bcl2 files from the sequencer into aligned and counted matrices using CellRanger software version 1.31. All samples prepared with V2 chemistry were aggregated together using the 10x aggregation pipeline to produce a sample-normalized digital expression matrix with cell identities as columns and genes as rows.

Post-aggregation analysis was performed using the Seurat package in R-Studio, version 1.4.0.7.(Alexis) Aggregated data was filtered to remove cells that had fewer than 200 genes and for genes that appeared in fewer than 3 cells. Remaining cells were normalized to counts of 10,000 genes per cell and then log10 transformed. Cells with a Z score of 4 or greater for number of genes were presumed to be doublets and removed from analysis. Cells with a Z score of 3 or greater for percent of mitochondrial genes were presumed to be low diversity and removed from analysis. Variation due to the number of UMIs and percent of mitochondrial genes were regressed out. We defined variable genes as those with a coefficient of variance > 1. We ran principal component analysis (PCA) on variable genes using default settings. To determine statistically significant principal components (PCs) we used the native Jackstraw function on all 40 PCs generated from PCA, using 200 iterations and permuting 1% of the data each iteration. We took any PC with an overall significance score of $p \leq 0.001$. We utilized those principal components to produce t-SNE plots and to perform K-nearest neighbor clustering, both functions are native to the Seurat package.

Separately, we used hclust to create heatmaps of gene expression by cell. For Nonnegative matrix factorization, we used the NMF package by Gaujoux et

al. version 0.17.6[17] with the algorithm set to Brunet (Brunet) and the seed set to Nonnegative Double Singular Value Deconvolution (nndsvd).[22]

REFERENCES

(1) Visvader, J. E. *Genes & Development* **2009**, *23* (22), 2563–2577.

(2) Prater, M. D.; Petit, V.; Alasdair Russell, I.; Giraddi, R. R.; Shehata, M.; Menon, S.; Schulte, R.; Kalajzic, I.; Rath, N.; Olson, M. F.; Metzger, D.; Faraldo, M. M.; Deugnier, M.-A.; Glukhova, M. A.; Stingl, J. *Nat Cell Biol* **2014**, *16* (10), 942–950.

(3) Tornillo, G.; Smalley, M. J. *J Mammary Gland Biol Neoplasia* **2015**, *20* (1-2), 63–73.

(4) Carroll, J. S.; Meyer, C. A.; Song, J.; Li, W.; Geistlinger, T. R.; Eeckhoute, J.; Brodsky, A. S.; Keeton, E. K.; Fertuck, K. C.; Hall, G. F.; Wang, Q.; Bekiranov, S.; Sementchenko, V.; Fox, E. A.; Silver, P. A.; Gingeras, T. R.; Liu, X. S.; Brown, M. *Nat Genet* **2006**, *38* (11), 1289–1297.

(5) Dontu, G.; Ince, T. A. *J Mammary Gland Biol Neoplasia* **2015**, *20* (1-2), 51–62.

(6) Zheng, G. X. Y.; Terry, J. M.; Belgrader, P.; Ryvkin, P.; Bent, Z. W.; Wilson, R.; Ziraldo, S. B.; Wheeler, T. D.; McDermott, G. P.; Zhu, J.; Gregory, M. T.; Shuga, J.; Montesclaros, L.; Underwood, J. G.; Masquelier, D. A.; Nishimura, S. Y.; Schnall-Levin, M.; Wyatt, P. W.; Hindson, C. M.; Bharadwaj, R.; Wong, A.;

Ness, K. D.; Beppu, L. W.; Deeg, H. J.; McFarland, C.; Loeb, K. R.; Valente, W. J.; Ericson, N. G.; Stevens, E. A.; Radich, J. P.; Mikkelsen, T. S.; Hindson, B. J.; Bielas, J. H. *Nat Comms* **2017**, *8*, 14049–12.

(7) Klein, A. M.; Mazutis, L.; Akartuna, I.; Tallapragada, N.; Veres, A.; Li, V.; Peshkin, L.; Weitz, D. A.; Kirschner, M. W. *Cell* **2015**, *161* (5), 1187–1201.

(8) Macosko, E. Z.; Basu, A.; Satija, R.; Nemesh, J.; Shekhar, K.; Goldman, M.; Tirosh, I.; Bialas, A. R.; Kamitaki, N.; Martersteck, E. M.; Trombetta, J. J.; Weitz, D. A.; Sanes, J. R.; Shalek, A. K.; Regev, A.; McCarroll, S. A. *Cell* **2015**, *161* (5), 1202–1214.

(9) Novak, R.; Zeng, Y.; Shuga, J.; Venugopalan, G.; Fletcher, D. A.; Smith, M. T.; Mathies, R. A. *Angew. Chem. Int. Ed.* **2010**, *50* (2), 390–395.

(10) Medina, D. *Breast Cancer Research* **2013**, *15* (3), R36–2.

(11) Blakely, C. M. *Cancer Research* **2006**, *66* (12), 6421–6431.

(12) Meier-Abt, F.; Milani, E.; Roloff, T.; Brinkhaus, H.; Duss, S.; Meyer, D. S.; Klebba, I.; Balwierz, P. J.; van Nimwegen, E.; Bentires-Alj, M. *Breast Cancer Research* **2013**, *15* (2), R36.

(13) Satija, R.; Farrell, J. A.; Gennert, D.; Schier, A. F.; Regev, A. *Nat Biotechnol* **2015**, *33* (5), 495–502.

(14) Wilson, C. L. *Endocrine Related Cancer* **2006**, *13* (2), 617–628.

(15) Tanos, T.; Sflomos, G.; Echeverria, P. C.; Ayyanan, A.; Gutierrez, M.; Delaloye, J.-F.; Raffoul, W.; Fiche, M.; Dougall, W.; Schneider, P.; Yalcin-Ozuysal, O.; Brisken, C. *Sci Transl Med* **2013**, *5* (182), 182ra55.

(16) Pardo, I.; Lillemoe, H. A.; Blosser, R. J.; Choi, M.; Sauder, C. A. M.; Doxey, D. K.; Mathieson, T.; Hancock, B. A.; Baptiste, D.; Atale, R.; Hickenbotham, M.; Zhu, J.; Glasscock, J.; Storniolo, A. M. V.; Zheng, F.; Doerge, R. W.; Liu, Y.; Badve, S.; Radovich, M.; Clare, S. E. *Breast Cancer Research* **2014**, *16* (2), R26.

(17) Gaujoux, R.; Seoighe, C. *BMC Bioinformatics* **2010**, *11* (1), 367.

(18) Zhu, X.; Ching, T.; Pan, X.; Weissman, S. M.; Garmire, L. *PeerJ* **2017**, *5* (11), e2888–20.

(19) Brunet, J.-P.; Tamayo, P.; Golub, T. R.; Mesirov, J. P. *Proc. Natl. Acad. Sci. U.S.A.* **2004**, *101* (12), 4164–4169.

(20) Greenbaum, D.; Colangelo, C.; Williams, K.; Gerstein, M. *Genome Biol* **2003**, *4* (9), 117.

(21) Schwanhäusser, B.; Busse, D.; Li, N.; Dittmar, G.; Schuchhardt, J.; Wolf, J.; Chen, W.; Selbach, M. *Nature* **2011**, *473* (7347), 337–342.

(22) Boutsidis, C.; Gallopoulos, E. *Pattern Recognition* **2008**, *41* (4), 1350–1362.

FIGURES AND TABLES

Table 4-1. Flow Cytometry by Sample.

Sample	Live (%)	Lin - (%)	Double Negative (%)	EpCAM- CD49f+ (%) (Basal)	EpCAM+ (%)	EPCAM+ CD49f- (%) (Mature LEP)	EPCAM+ CD49f+ (%) (Lum Prog.)
RM263	87.8	73.2	36.2	8.99	49.6	63.9	33.1
RM264	61.4	90.2	13.8	28.3	49.8	77.6	20.1
RM272	77.9	85	24.7	8.3	61.9	90.7	7.75
RM273	64	89.5	21.2	9.81	57.6	32.4	61.4
RM282	76.2	90.8	20.3	26	49.2	9.69	89.7

Figure 4-1. Percentage of Epithelial Cells Defined as MEPs/Basal Cells in Flow Cytometry by Sample.

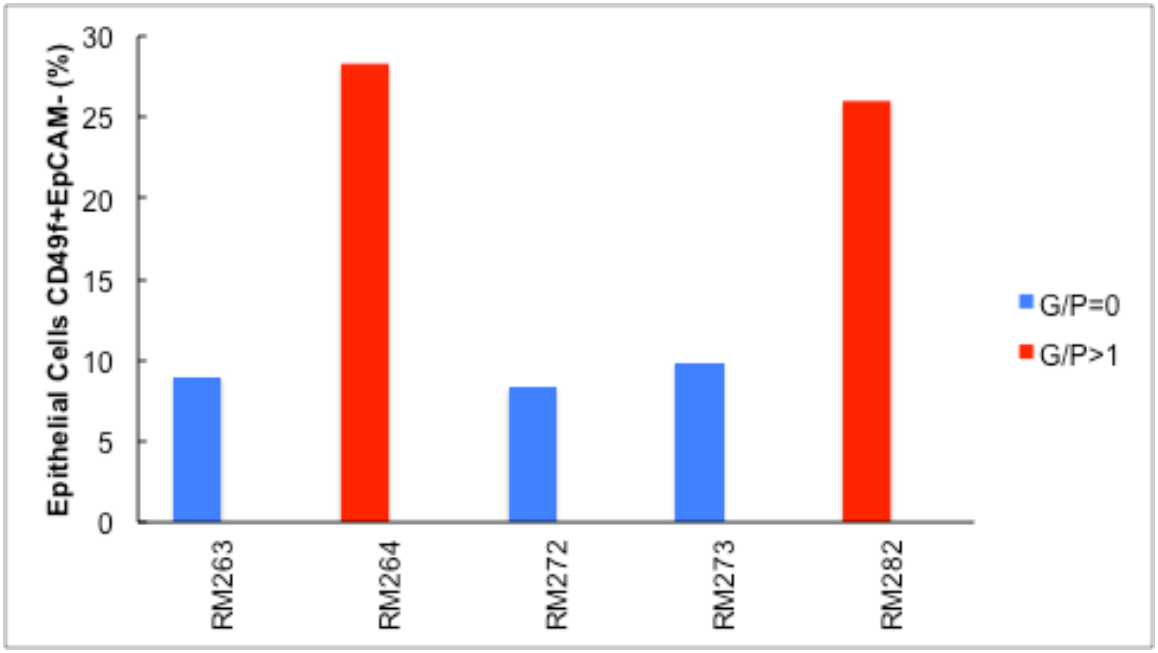

There is a substantial increase in the percentage of epithelial cells appearing in the MEP gate by flow cytometry, defined as CD49f+/EpCAM- for samples from women who have a previous history of pregnancy (G/P>1) compared to those who have no history of pregnancy (G/P=0).

Figure 4-2. t-SNE Plot of scRNA Seq Data by Cell Type.

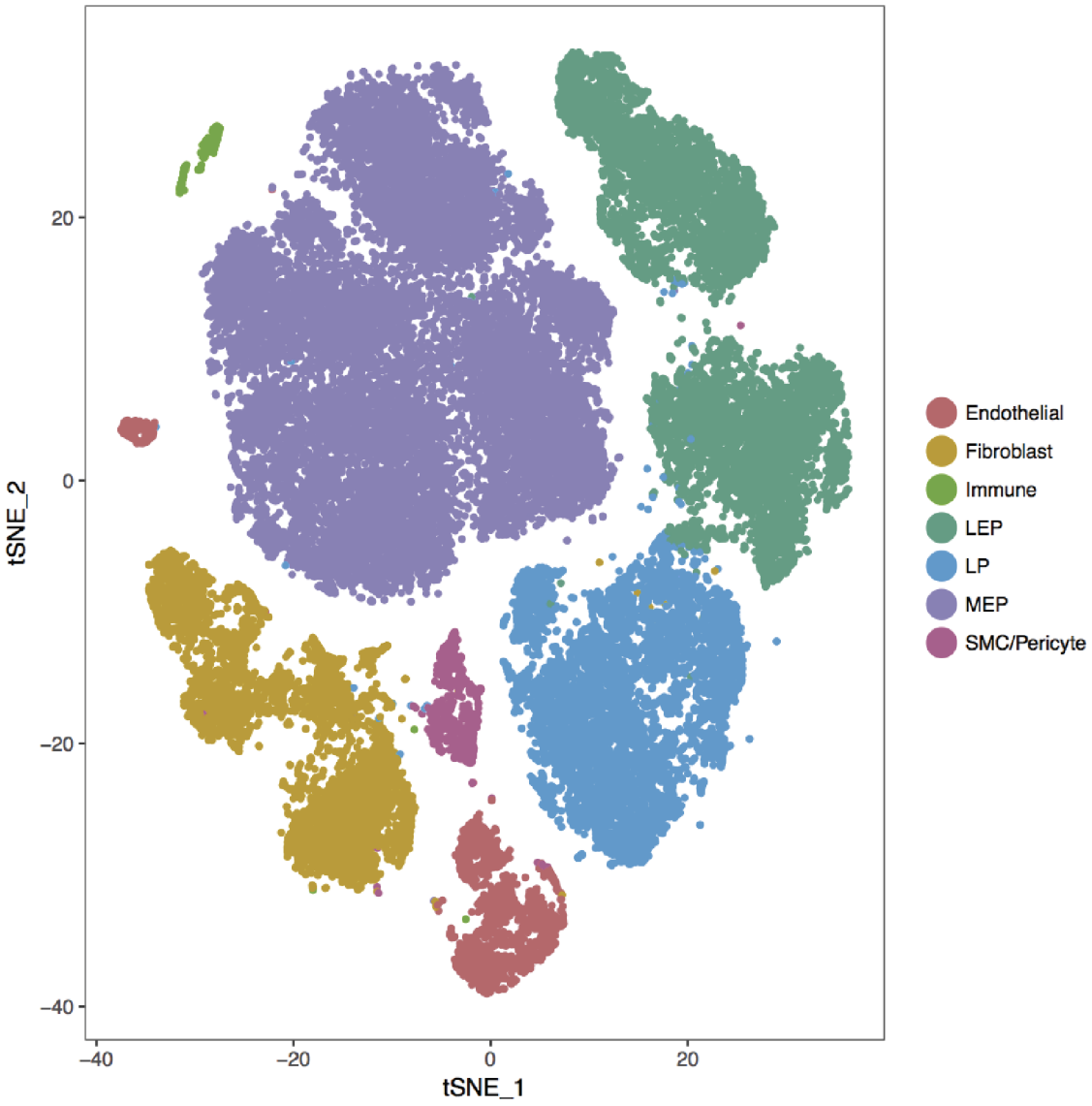

Plotting of all 40,000 cells sequenced on V2 chemistry on t-SNE axies based on var genes with k nearest neighbor clustering by cell type reveals the major cell subtypes in the proportions we expect from flow cytometry.

Figure 4-3. Principal Component Plot of Major Cell Types by Sample ID.

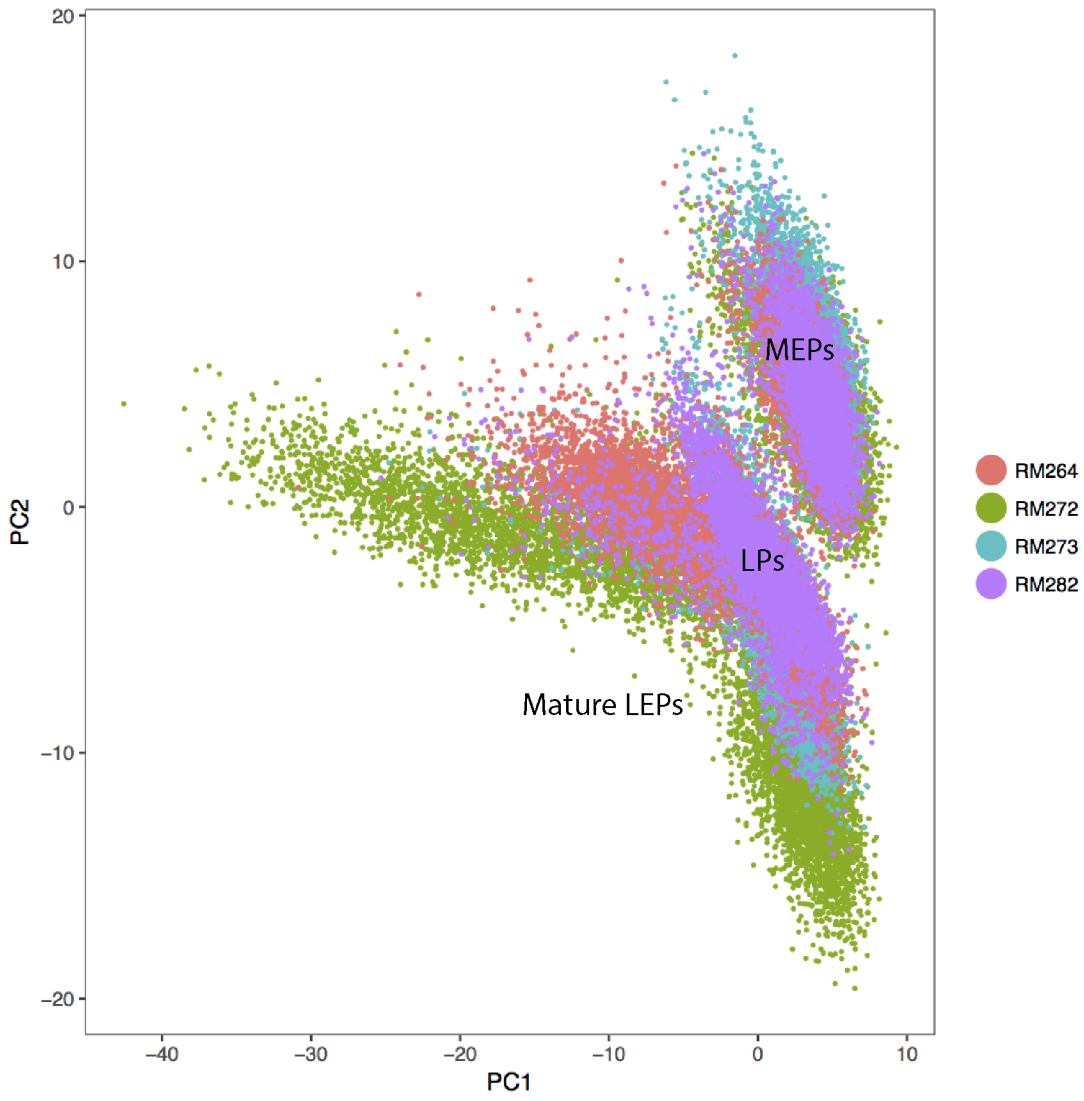

This is a subset of the data just focusing on epithelial cells. Major cell types (annotated on graph) are separable even based just on the information captured in the first two principal components.

Figure 4-4. t-SNE Plot of scRNA Seq Data by Sample ID.

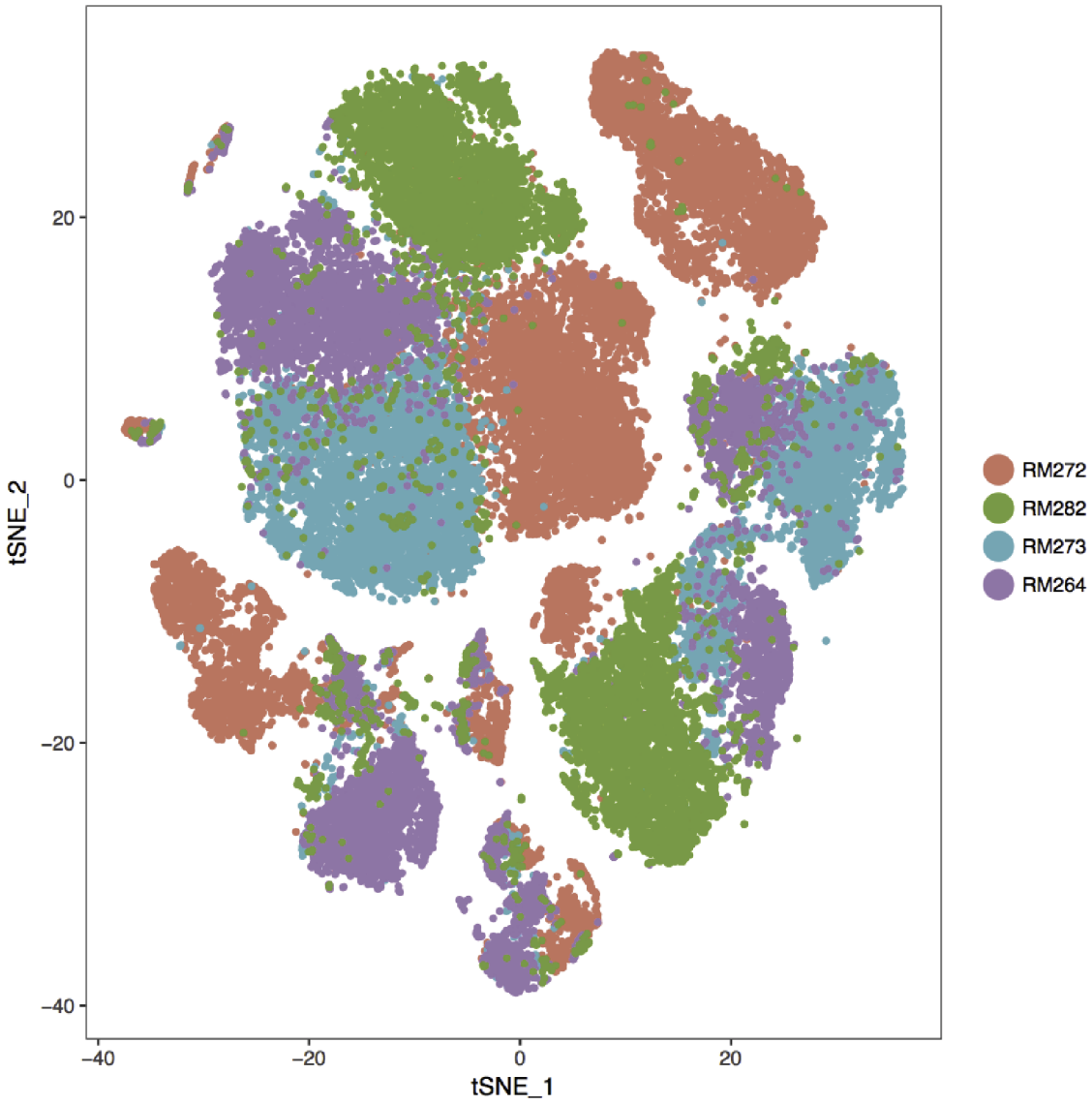

Plotting of all 40,000 cells sequenced on V2 chemistry on t-SNE axies based on var genes clustering by sample identification reveals batch to batch differences driving separation of the same major cell classes from each woman. It is apparent that for mature LEPs and Luminal Progenitors, RM272 is particular is an outlier.

Figure 4-5. t-SNE Plot of All LEPs by Sample Identification.

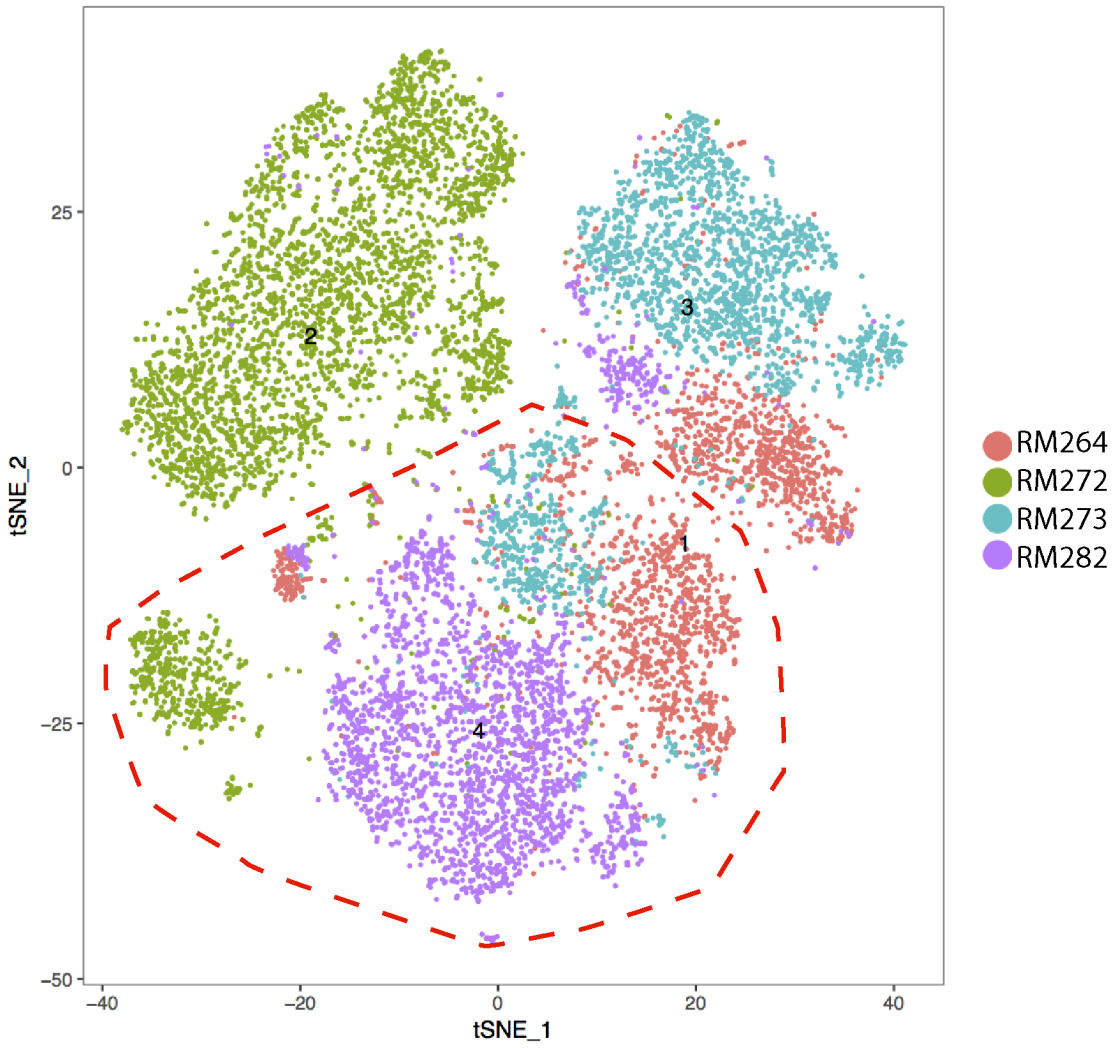

Plotting all LEPs – both mature and luminal progenitors by sample ID on t-SNE axis based on var genes re-calculated for this subsetted data. Luminal progenitors (based on marker analysis) are circled in the red dotted line. From this plot it appears that cells are roughly organized into mature LEPs and luminal progenitors, separated by sample identification with the most prominent outlier being RM272.

Figure 4-6. Heatmap of Mature LEPs by Batch Genes, Organized by Hierarchical Clustering.

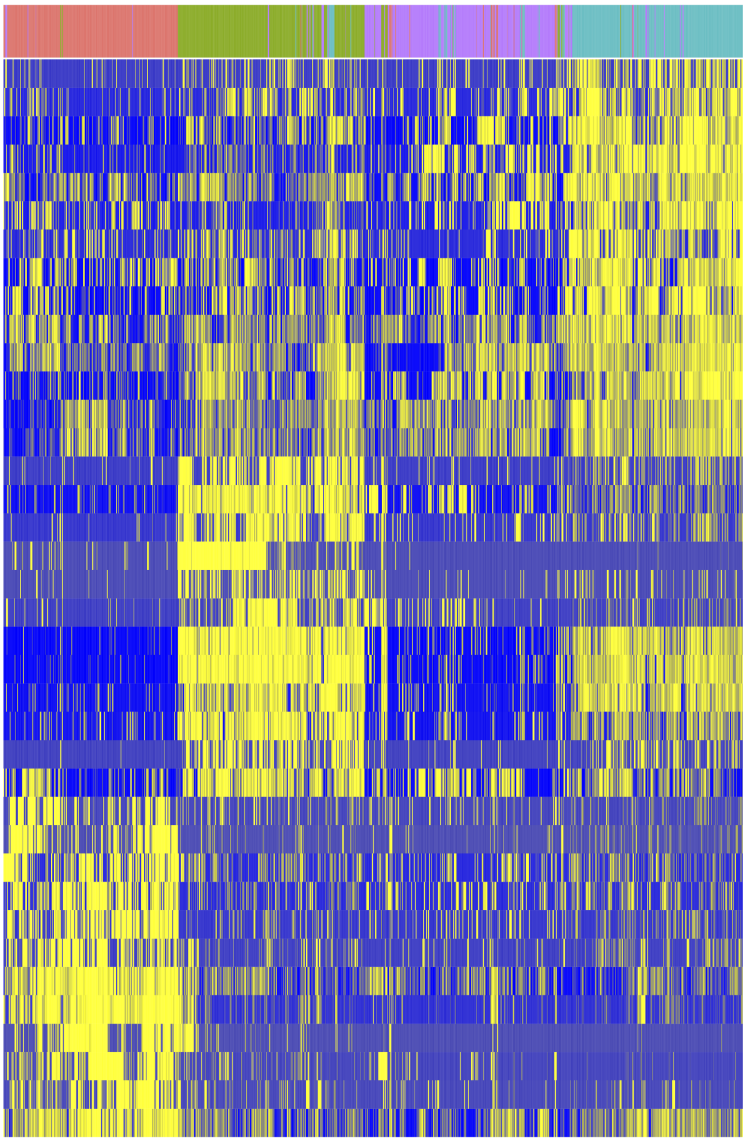

A matrix of mature LEPs by batch genes with cell IDs annotated at the top by colored bars. Yellow indicates high expression. It is apparent that several genes defined as variable genes in Seurat primarily describe sample to sample differences rather than cellular heterogeneity within samples.

Figure 4-7. Mature LEP Basis and Mixture Matrices.

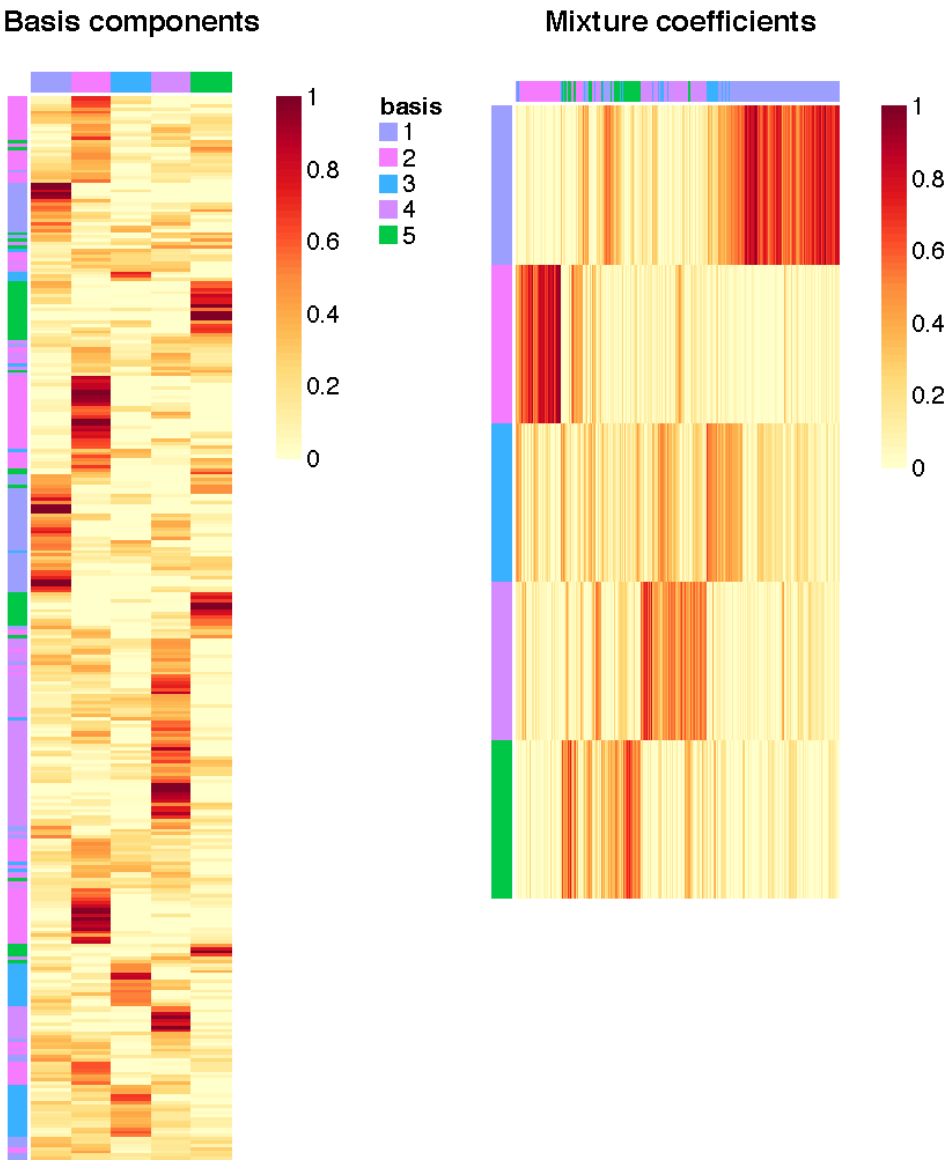

For a rank of 5, the mature LEP matrix was factored into two matrices which when multiplied together will result in the original matrix. The first is basis by genes with high expression per cluster in red. The second matrix is cells by mixture coefficients. In this way NMF simultaneously organizes cells into clusters and gives a list of genes that define those clusters.

Figure 4-8. Determining the Correct Rank Number Empirically.

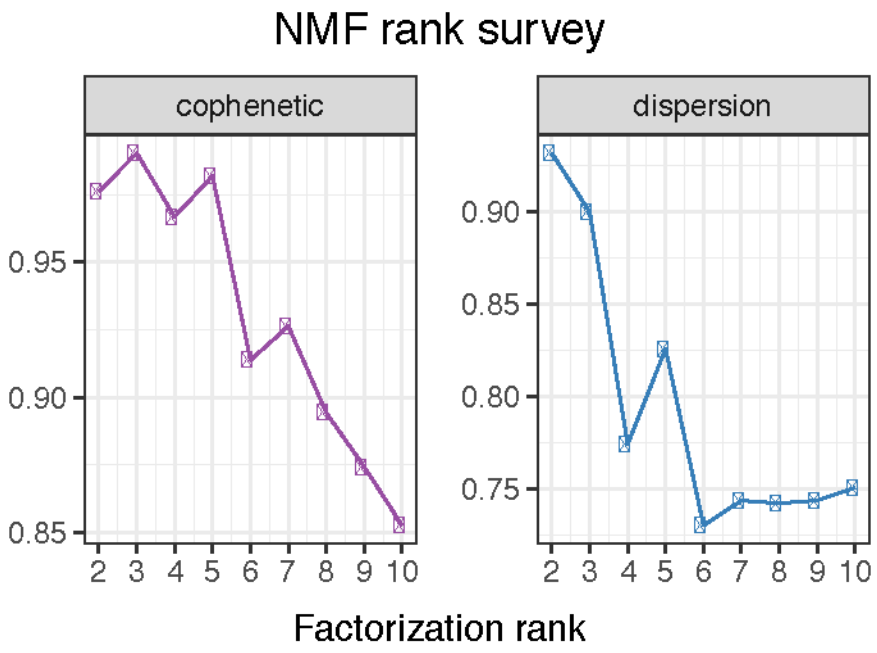

30 NMF simulations were performed for each rank 2 through 10. It is clear that beyond a rank of 3, there is a local maxima at rank of 5 by both the cophentic and dispersion metrics. We proceeded with rank 5 for factorizing mature LEPs.

Figure 4-9. Hierarchical Clustered Heatmap of Genes that Mark Each NMF Rank.

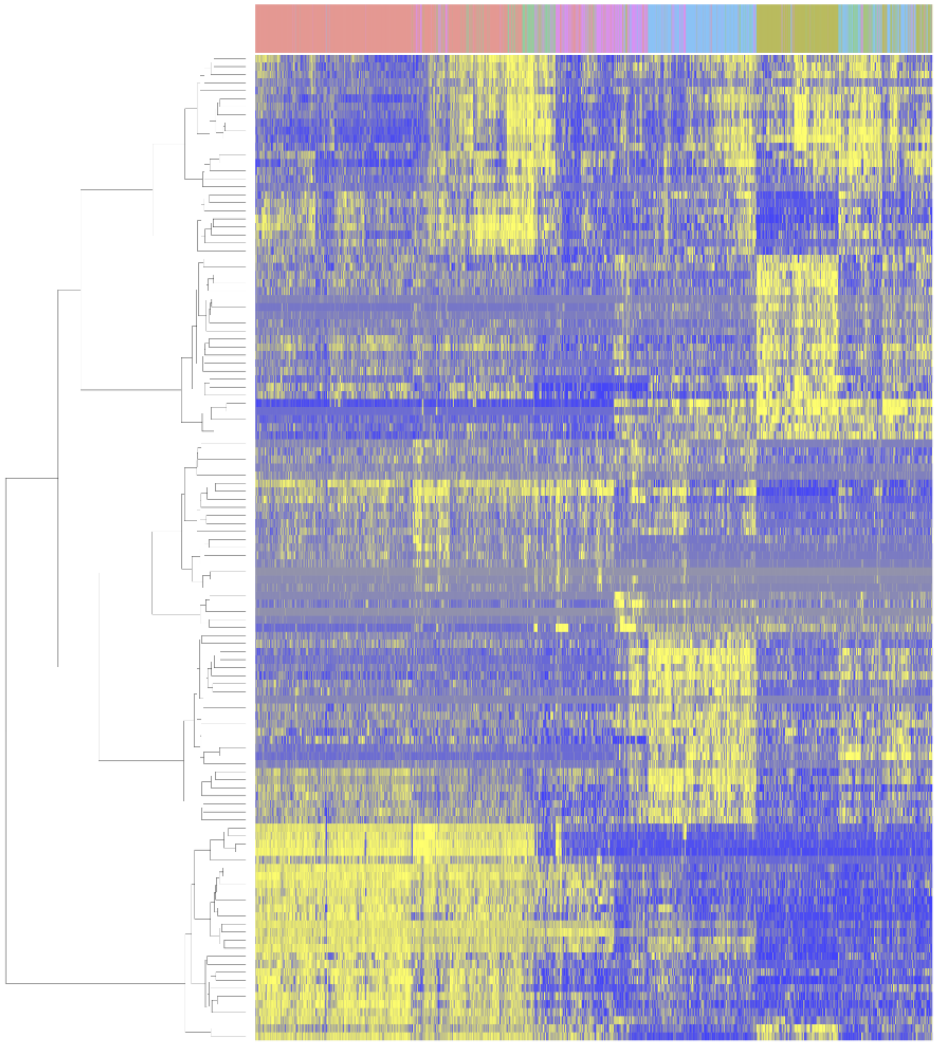

A cells by gene matrix of mature LEPs. Marker analysis in Seruat was performed with mature LEP IDs set as their assigned rank in NMF. The mature LEP by genes matrix was reproduced with a gene list consisting of the measured markers. The colored bars across the top indicate which NMF cluster each cell belongs to. This organization reveals clear gene module patterns that are high for subsets of mature LEPs.

SUPPLEMENTARY

Table 4-S1. Patient sample and demographic information.

Patient Code	10x Kit	Age	Ethnicity	Gravidity/ Parity	BMI	Menopause	Hormone Usage
RM 263	(V1)	23	Caucasian	0/0	26	Pre	N
RM 272	(V2)	24	Caucasian	0/0	27.3	Pre	N
RM 264	(V2)	37	African American	6/3	31.5	Pre	N
RM 273	(V2)	24	African American	0/0	26.2	Pre	Briefly
RM 282	(V2)	36	Caucasian	2/2	44.3	Pre	N

Table 4-S2. Genes that specifically mark major epithelial cell types in the present study.

MEP	LEP	Luminal Progenitor
KRT5	KRT18	SLPI
KRT14	KRT19	LTF
KRT17	KRT8	KRT23
ACTA2	CLDN4	S100A9
ACTG2	AZGP1	WFDC2
MT1X		

Table 4-S3. Antibody materials list.

Antibody Target	Conjugation	Volume per million cells (µL)	Source, Catalogue No. & Clone ID
EpCAM	FITC	1.5	BD 550257, Clone AD2
CD49f	APC	4	Stemcell 10109 VU1D9
CD2	Biotin	8	Biolegend 313626 GoH3
CD3	Biotin	8	BD 55325 RPA-2.10
CD16	Biotin	8	BD 555338 HIT3a
CD64	Biotin	8	BD 555526 10.1
CD31	Biotin	4	Inbitrogen MHCD31154 MBC78.2
CD45	Biotin	1	Biolegend 304004 HI30
Streptavidin	BV785	1	Biolegend 405249
DAPI	N/A	2 drops	Thermo R37606

Figure 4-S1. Example of Flow Cytometry Gates.

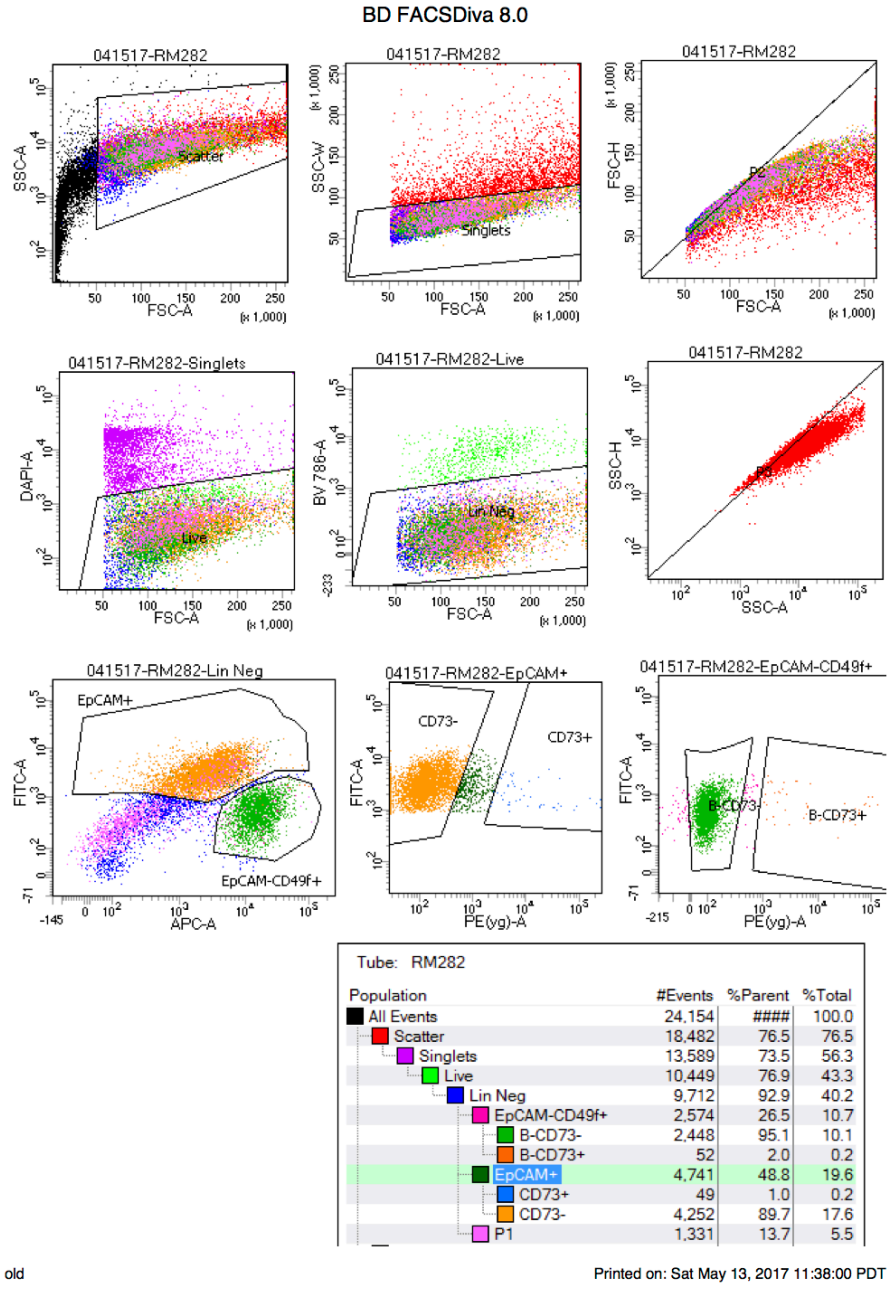

Gating scheme showing the hierarchy of gates and the relative position of the gates used in this study to separate major cell types.

APPENDIX

LIST OF PUBLICATIONS

1. Weber, R. J., Liang, S. I., Selden, N. S., Desai, T. A., & Gartner, Z. J. (2014). *Efficient Targeting of Fatty-Acid Modified Oligonucleotides to Live Cell Membranes through Stepwise Assembly*. Biomacromolecules, 15(12), 4621–4626. http://doi.org/10.1021/bm501467h

2. Todhunter, M.E., Weber, R.J., Farlow, J., Jee, N.Y., Cerchiari, A.E. *and* Gartner, Z.J. 2016. *Fabrication of 3-D reconstituted organoid arrays by DNA-programmed assembly of cells (DPAC).* Curr. Protoc. Chem. Biol. 8:147-178. *doi: 10.1002/cpch.8*

3. Weber, R. J., Cerchiari, A. E., Delannoy, L. S., Garbe, J. C., Labarge, M. A., Desai, T. A., & Gartner, Z. J. (2016). *Rapid Organoid Reconstitution by Chemical Micromolding.* ACS Biomaterials Science & Engineering, 2(11), 1851–1855. http://doi.org/10.1021/acsbiomaterials.6b00421

4. Weber, R. J., Desai, T. A., & Gartner, Z. J. (2017). *Non-autonomous cell proliferation in the mammary gland and cancer*. Current Opinion in Cell Biology, 45, 55–61. http://doi.org/10.1016/j.ceb.2017.02.009

5. Lyndsay M. Murrow, Robert J. Weber, Zev J. Gartner. Development 2017 *Dissecting the stem cell niche with organoid models: an engineering-based approach*, 144: 998-1007; doi: 10.1242/dev.140905

PUBLISHING AGREEMENT

It is the policy of the University to encourage the distribution of all theses, dissertations, and manuscripts. Copies of all UCSF theses, dissertations, and manuscripts will be routed to the library via the Graduate Division. The library will make all theses, dissertations, and manuscripts accessible to the public and will preserve these to the best of their abilities, in perpetuity.

I hereby grant permission to the Graduate Division of the University of California, San Francisco to release copies of my thesis, dissertation, or manuscript to the Campus Library to provide access and preservation, in whole or in part, in perpetuity.

Author Signature Rob Wilk Date 6/13/2017